Doctoral Thesis

DEVELOPMENT OF EMPAD SENSORS INSPIRED BY SILICON RETINAS AND IMPLEMENTED IN CMOS TECHNOLOGY

by

JORGE JOHANNY SÁENZ NOVAL

Supervised by:

Dr. LIONEL CERVERA GONTARD
Dr. JUAN ANTONIO LEÑERO BARDALLO

Condensed Matter Physics Department
October, 2024

Abstract

This thesis investigates the application of neuromorphic principles in designing and implementing advanced Electron Microscopy Pixel Array Detectors (EMPAD). The objective is to overcome conventional detector limitations, particularly in data throughput, temporal resolution, and energy discrimination, by utilizing systems that mimic biological processes through asynchronous and event-driven communication.

The research begins in Chapter 1 by analyzing the challenges that EMPADs face in Electron Microscopy (EM), emphasizing the need for innovative solutions to enhance their performance. Chapter 2 reviews the specifications and limitations of current detector technologies, including trade-offs associated with pixel size, charge sharing, and coincidence loss. It then introduces the principles of neuromorphic engineering, displaying their potential to optimize EMPAD design.

Chapter 3 describes the practical development of a neuromorphic EMPAD with Address-Event Representation (AER), covering its architecture, pixel design, and readout circuits. Simulations conducted in this research show that the AER protocol can achieve data reduction factors of up to 7.3 compared to conventional frame-based readout schemes. Experimental evaluation of the pixel under electron beam irradiation further validates its functionality. It demonstrates its ability to accurately estimate the metal collector's total electron emission yield (σ). Chapter 4 explores the integration of a spectral sensitivity sensor into a pixel array, allowing color imaging and future energy discrimination in EM. Two methods for energy resolution, stacked diodes and neuromorphic Time-over-Threshold (ToT) measurements, are investigated and compared.

The design, implementation, and evaluation of a prototype with stacked diodes are detailed. A 2816-pixel array (64 $\times$ 44 pixels) with integrated neuromorphic pixels was fabricated using a 0.18 µm UMC CMOS process. Both prototypes validate the color (energy) discrimination capability and demonstrate the advantages of applying neuromorphic concepts to EMPAD design. Finally, the thesis summarizes the main results and contributions, emphasizing the success of incorporating biologically-inspired concepts in EMPAD development.

Key words: Electron Microscopy Pixel Array Detectors (EMPADs), Address-Event Representation (AER), CMOS Image Sensors, 4D-STEM, Neuromorphic Systems

Resumen

Esta tesis investiga la aplicación de principios neuromórficos en el diseño e implementación de Detectores de Matriz de Píxeles para Microscopía Electrónica (EMPAD). El objetivo es superar las limitaciones de los detectores convencionales, en especial la tasa de datos, la resolución temporal y la discriminación de energía, utilizando sistemas que imitan procesos biológicos mediante comunicación asíncrona y basada en eventos.

La investigación comienza en el Capítulo 1 con el análisis de los desafíos que enfrentan los EMPAD en la Microscopía Electrónica (ME), destacando la necesidad de soluciones innovadoras. El Capítulo 2 revisa las especificaciones y limitaciones de las tecnologías actuales de detectores, incluidos los compromisos asociados con el tamaño de los píxeles, el compartimiento de carga y la pérdida por coincidencia. Luego, se introducen los principios de la ingeniería neuromórfica, mostrando su potencial para optimizar el diseño de los EMPAD. El Capítulo 3 describe el desarrollo práctico de un EMPAD con Representación de Eventos por Dirección (AER), abarcando su arquitectura, diseño de píxeles y circuitos de lectura. Las simulaciones realizadas muestran que el protocolo AER puede alcanzar factores de reducción de datos de hasta 7.3 en comparación con los esquemas de lectura convencionales basados en tramas. La evaluación experimental del píxel bajo un haz de electrones ratifica su funcionalidad. Demuestra su capacidad para estimar con precisión el rendimiento total de emisión de electrones del colector metálico (σ). El Capítulo 4 explora la integración de la sensibilidad espectral en una matriz de píxeles, permitiendo la adquisición de la imagen en color y la futura discriminación de energía en ME. Se investigan y comparan dos métodos para la resolución de energía: diodos apilados y mediciones neuromórficas de Tiempo sobre Umbral (ToT). Se detallan el diseño, implementación y evaluación de un prototipo con diodos apilados. Una matriz de 2816 píxeles (64 $\times$ 44 píxeles) neuromórficos integrados fue fabricada utilizando el proceso UMC CMOS de 0.18 µm. Ambos prototipos validan la capacidad de discriminación de color (energía) y demuestran las ventajas de aplicar conceptos neuromórficos al diseño de EMPAD. Finalmente, la tesis resume los principales resultados y contribuciones, destacando el éxito en la incorporación de los conceptos inspirados biológicamente en el desarrollo de los EMPAD.

Palabras clave: Detectores de Matriz de Píxeles para Microscopía Electrónica (EMPADs), Representación de Eventos por Dirección (AER), Sensores de Imagen CMOS, 4D-STEM, Sistemas Neuromórficos

Agradecimientos

Este trabajo de tesis no habría sido posible sin el apoyo y la colaboración de numerosas personas e instituciones a las que deseo expresar mi más sincero agradecimiento.

En primer lugar, quiero manifestar mi profunda gratitud a mis directores de tesis. De un lado, a Lionel Cervera Gontard, por su interés en mi experiencia, proponer este tema de investigación que me atrajo y su constante apoyo a lo largo de este proceso. Su interés por mi desarrollo y motivación han sido fundamentales para el desarrollo de esta investigación. De otro lado, a Juan Antonio Leñero, por su ayuda, preocupación, consejos técnicos y de vida. También por sus valiosas aportaciones y disponibilidad para resolver mis dudas y editar mis textos en cualquier momento y brindarme su experiencia en el tema y en la escritura.

Quiero expresar mi más sincero agradecimiento a la Universidad de Cádiz (UCA) por su apoyo y financiación, así como a los profesores del Departamento de Física de la Materia Condensada, por su valiosa colaboración, los enriquecedores encuentros y el ambiente de trabajo tan estimulante que han creado. Gracias a Carlos, Javi, María, Enrique, Edu y Petra por varios desayunos, comidas y momentos de vida de un predoctoral. Agradezco a Rubén Gómez Merchán, por su ayuda en la consecución del circuito integrado y su enorme realimentación. Agradezco también a Enrique Gallero por su asistencia técnica y su ayuda en la realización de los experimentos, y por su paciencia para resolver temas que un ingeniero entiende de antemano. Al profesor Wei Tan por abrirme la posibilidad de estancia en EUA y haberme recibido allí. Al Instituto de Microelectrónica de Sevilla (IMSE), por permitirme el acceso a sus herramientas de diseño analógico, así como por poner a mi disposición su valiosa infraestructura y equipo humano, lo cual fue fundamental para el desarrollo de mi proyecto

No puedo olvidar el apoyo incondicional de mi familia, mis padres Jorge Sáenz y Nancy Noval, por su amor, comprensión y aliento constante durante mis estudios, así como a mis dos hermanas por su soporte en la distancia. Agradezco también a Ramón y su familia por hacerme sentir uno más entre ellos. Finalmente, quiero mostrar mi gratitud a Margarita Didenko por su gran compañía y apoyo este último año. A pesar de que no siempre elegimos las guerras que enfrentamos, sí tenemos el poder de decidir con quién compartimos nuestras batallas.

A todos ellos, mi más sincero agradecimiento.

List of Acronyms

ABF	Annular Bright Field
ADC	Analog-to-Digital Converter
ADF	Annular Dark Field
ADS	Active Detector Size
AER	Address-Event Representation
AFM	Atomic Force Microscopy
ASIC	Application-Specific Integrated Circuit
BF	Bright Field
BSE	Backscattered Electron
CCD	Charge-Coupled Device
CL	Cathodoluminescence
CMOS	Complementary Metal-Oxide Semiconductor
COM	Center-of-Mass
CSA	Charge Sensitive Amplifier
CSD	Charge-Sharing Discrimination
CSM	Charge Summing Mode
CUDA	Compute Unified Device Architecture
DED	Direct Electron Detector
DD	Displacement Damage
DHCS	Dual Space Compressive Sensing
DR	Dynamic Range
DRAM	Dynamic Random-Access Memory
DVS	Dynamic Vision Sensor
EDS	Energy-Dispersive X-ray Spectroscopy
EELS	Electron Energy Loss Spectroscopy
EER	Event-based electron representations
ELT	Enclosed Layout Transistor
ELF	Energy-Loss Function
EM	Electron Microscopy
EMPAD	Electron Microscopy Pixelated Array Detector
EPS	Effective Pixel Size
ES	Energy Spread

FC	Faraday Cup
FIB	Focused Ion Beam
FPGA	Field-Programmable Gate Array
FPN	Fixed Pattern Noise
FoV	Field of View
fps	frames per second
FWHM	Full Width at Half Maximum
GDSII	Graphic Database System II
Gy	Gray
HAADF	High-angle Annular Dark Field
HPD	Hybrid Pixel Detector
I&F	Integrate and Fire
IC	Integrated Circuit
iDPC	integrated Differential Phase Contrast
IMSE	Instituto de Microelectr0̆0f3nica de Sevilla
IRN	Input-referred Noise
LSB	Least Significant Bit
MAPS	Monolithic Active Pixels Sensor
MTF	Modulation Transfer Function
NIR	Near-Infrared
NNPS	Normalized Noise Power Spectrum
NPS	Noise Power Spectrum
OpenMP	Open Multi-Processing
PCB	Printed Circuit Board
PDM	Pulse Density Modulation
PGA	Pin Grid Array
PPS	Physical Pixel Size
PSF	Point-Spread Function
PVD	Physical Vapor Deposition
QE	Quantum Efficiency
RGB	Red, Green, Blue
ROIC	Readout Integrated Circuit
ROI	Region of Interest
SEM	Scanning Electron Microscopy

SE	Secondary Electron
SEE	Single-Event Effect
SEU	Single Event Upset
SET	Single Event Transient
SNR	Signal-to-Noise Ratio
SRAM	Static Random-Access Memory
STEM	Scanning Transmission Electron Microscopy
SCL	Supercooled Liquids
TDM	Time-Division Multiplexing
TEM	Transmission Electron Microscopy
TID	Total Ionizing Dose
TG	Transmission Gate
ToA	Time-of-Arrival
ToF	Time-of-Flight
ToT	Time-over-Threshold
TSM	Top Surface Metallurgy
UBM	Under Bump Metallization
UMC	United Microelectronics Corporation
USB	Universal Serial Bus
VLSI	Very-Large-Scale Integration
XPS	X-ray Photoelectron Spectroscopy
ZLP	Zero-Loss Peak

Contents

List of Figures

List of Tables

Chapter 1

Introduction

Living organisms possess remarkable sensory capabilities, constantly extracting information from their environment through biological sensors to guide survival and maintain adequate behavior. Biological systems leverage the brain for efficient information transfer and compact storage. In contrast to computers, biological systems operate on a massively parallel architecture with billions of neurons working together, enabling rapid and efficient information processing and far surpassing conventional electronics systems.

The brain's ability to learn, adapt, and operate with minimal power exemplifies nature's efficient design. It is a beacon of inspiration for developing new technologies that emulate biological information processing efficiency. It has prompted extensive research on neuromorphic systems –i.e., artificial systems that mirror the organizational principles of the biological nervous system. Pioneering efforts include the Cellular-Neural Network invented by Leon Chua [1] or Carver Mead's work [2] on neuromorphic electronic sensors. A standout example is the silicon retina invented by Mahowald [3] using neuromorphic principles that revolutionized the field of image sensors by significantly reducing the required bandwidth of conventional approaches. Mahowald proposed a microelectronics architecture that reported only spatial and temporal changes occurring in the visual scene, similar to how our eyes function. These innovations paved the way for numerous applications requiring high-data throughput that strive to achieve the same efficiency and functionality as biological systems [4]. For example, a modern promising approach to achieving high efficiency in image sensors lies in the use of asynchronous neuromorphic approaches like the Address-Event

Representation (AER) [5–7]. Among these bio-inspired sensors with asynchronous operation, there is a family known as Dynamic Vision Sensors (DVS) [8–10]. In contrast to conventional frame-based image sensors, DVS mimics the biological eye by responding asynchronously to changes in light intensity. They operate on an event-driven principle, outputting a stream of events whenever a pixel detects a significant change in light. Inspired by biological vision, this approach significantly reduces data redundancy and allows for real-time processing of high-speed visual information.

Beyond research, neuromorphic image sensors are used in real applications requiring fast responses, like autonomous driving, drone navigation, or industrial quality inspection. Nonetheless, there is growing interest in the potential of such image sensors in other fields, like scientific instrumentation, where they hold significant promise for various applications. One of those fields is Electron Microscopy (EM).

1.1. Electron microscopy: trends and challenges

Electron microscopes study matter at scales ranging from the size of an atom to the macroscopic scale. They work by "illuminating" a sample with a beam of accelerated electrons and measuring the signals generated from the sample. These microscopes are extensively used in various fields of science and technology to study the physical and chemical properties of semiconductor devices, catalysts, pharmaceuticals, or cells. The primary results of electron microscopy are the image of the analyzed sample and its chemical composition.

Three primary types of electron microscopy techniques can be differentiated by how the images are formed. These are:

1. **Scanning Electron Microscopy or SEM** operates typically with electrons accelerated in the range between 5-30 kV. An image of a bulk sample is formed by scanning a focused electron beam and measuring the secondary electrons emitted from the sample's surface;

2. **Transmission Electron Microscopy or TEM** operates typically with electrons accelerated between 80-300 kV. An image is formed by illuminating a very thin sample (or electron-transparent sample) with a broad electron beam and measuring those electrons transmitted through the sample;

3. **Scanning Transmission Electron Microscopy or STEM** operates typically

with electrons accelerated in the range between 80-300 kV. It builds upon a combination of SEM and TEM principles, utilizing a focused electron beam to scan a very thin sample and collect the electrons transmitted at each sample point.

EM microscopes require three essential technologies: i) point sensors or image sensors also called "cameras", ii) spectrometers, and iii) image and data processing software. Significant advances in scientific understanding with these instruments stem from the most recent technological evolutions in any of those three components.

1.1.1 Multimodal STEM

STEM is increasingly popular as it has undergone a profound technological revolution from developing spherical aberration correctors, monochromators, high-brightness emission guns, improved vacuum quality, spectrometers, power supply stability, and powerful software. By combining imaging techniques with analytical techniques (in particular, electron energy loss spectroscopy (EELS) and energy dispersive X-ray spectroscopy (EDS)), STEM has now become a versatile and widely used tool to probe the structure, local chemistry, and optical properties of nanomaterials with a spatial resolution lower than one angstrom (atomic resolution) and a spectral resolution lower than 100 meV.

This ability to obtain multimodal data from a single experiment in EM presents significant advantages and is also one reason for the wide use of EM in science and engineering. For example, correlating various measurements such as morphology, elemental composition, or chemical bonding states can provide a more comprehensive understanding of a material's properties. One example is combining STEM and EELS, as demonstrated by Jarausch et al. in [11]. This technique combines the high spatial resolution of STEM with the rich chemical information gleaned from EELS. By acquiring a series of STEM images at different projections of the sample while simultaneously collecting the electron energy loss spectrum at each point, the reconstruction of a three-dimensional (3D) map depicting not only the three-dimensional morphology but also the elemental distribution and even chemical bonding states within a sample at the nanoscale is possible.

1.1.2 4D-STEM microscopy and EMPADs

Traditional STEM imaging typically relies on a set of fixed-geometry semiconductor sensors like the Bright Field (BF), Annular Bright Field (ABF), Annular Dark Field (ADF), and High-angle Annular Dark Field (HAADF) detectors (Figure 1.1(a)). These detectors integrate the electrons over specific, pre-defined regions of the diffraction plane formed by the focused electron beam after transversing an electron-transparent sample. While effective for some applications, this integration approach has limitations as it discards valuable high-resolution details in different diffraction pattern zones. A STEM image is a collection of discrete values measured across a 2D area by rastering the focused electron beam. It results in a comprehensive two-dimensional (2D) image whose pixel intensities are the integral values measured at each beam location.

Novel and powerful techniques are being developed in (S)TEM, supported by new types of electron sensors known as **Electron Microscopy Pixelated Array Detectors (EMPADs)**. With the availability of EMPADs, diffraction patterns or images in reciprocal space, given by the two-dimensional intensity distribution I(k_x, k_y), are recorded for each electron probe position (x, y) within a defined two-dimensional region of the sample (see Figure 1.1(b)). The resulting data is a collection of 2D patterns across a 2D area, which forms a comprehensive four-dimensional (4D) dataset.

The availability of these multi-dimensional datasets acquired with EMPADs has led to the emergence of new techniques in the field under the name of **4D-STEM** [12, 13]. The crucial advantage of 4D-STEM lies in its ability to acquire a rich array of information in each probe position, encompassing conventional STEM signals like BF, ABF, ADF, and HAADF but with more flexibility thanks to the availability of "virtual" segmented detectors of any geometry by combining the signals of pixels contained in a give region-of-interest. In addition, the wealth of data provided by EMPADs opens space for advanced analysis techniques, such as center-of-mass (COM), opening the door to measuring electrical/magnetic fields at the atomic level and novel electron phase contrast imaging modes (*aka.*, electron ptychography) with huge impact for detecting both heavy and light atoms [14, 15].

The recent advancements in detector technology and data acquisition strategies mean that, nowadays, multimodal EM also offers the acquisition of 4D-STEM data combined with other signals acquired with different detectors. In the work of Huth *et al.* [16], a novel design for a pnCCD chip with a center hole is presented. This

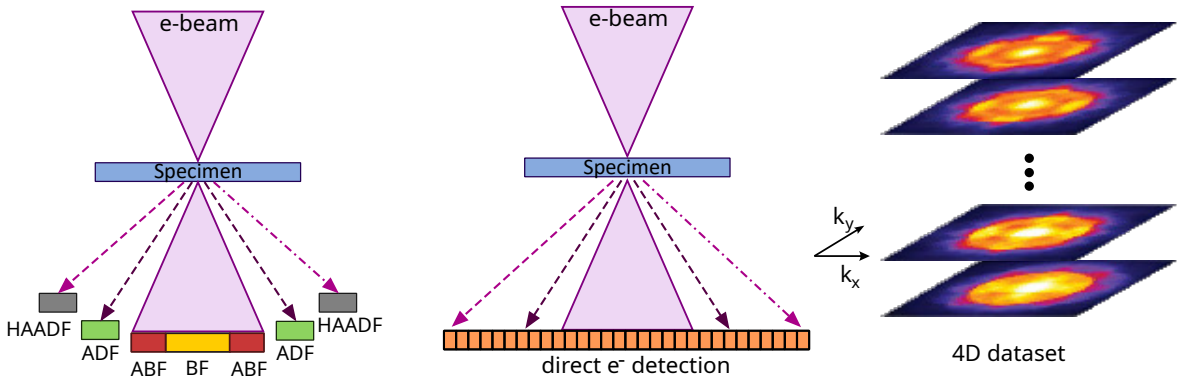

Figure 1.1: Comparison of conventional STEM and 4D-STEM. (a) In STEM, monolithic detectors are used in different angular regions to capture the integrated intensity. (b) In 4D-STEM, an image in reciprocal space is recorded with a pixelated array detector at each region's point containing the sample, generating a 4D-STEM dataset. For example, convergent beam electron diffraction patterns (or CBEDs) are shown at the right at each point. Adapted from [18].

innovative design allows the central part of the electron beam to pass through the detector and into the EELS spectrometer while simultaneously capturing the outer bright field disc and parts of the dark field signal on the pixelated 4D-STEM detector itself. This design eliminates the need to constantly switch between acquiring 4D-STEM and EELS data, significantly enhancing the efficiency of multimodal EM workflows. The works of Shi *et* [17] investigated the dynamic behavior of core-shell nanoparticles under elevated temperatures during an in-situ heating experiment. By combining 4D-STEM with energy-dispersive X-ray spectroscopy (EDX), the authors could monitor both the elemental distribution and lattice strain within the nanoparticles as they underwent interdiffusion and alloying.

In summary, 4D-STEM with EMPADs can provide new information on materials that are inaccessible through traditional methods. Therefore, there is great interest in the development of better 4D-STEM detectors. For example, faster and simpler detectors would allow faster experiments, enabling the capture of dynamic phenomena at the nanoscale through in-situ experiments or imaging with high-resolution organic samples while using lower electron doses.

1.1.3 High-data low-dose EM challenge

However, multimodal EM comes at a significant cost: a dramatic increase in raw data generated in every experiment compared to conventional EM. This increment is a massive challenge that necessitates advanced data processing and analysis strategies.

For example, consider the physical data infrastructure requirements for a 4D-STEM experiment consisting of the acquisition of nano-diffraction patterns of a sample:

1. The experiment might typically involve measuring patterns in a rectangular matrix of 256 × 256 probe positions.

2. The patterns are recorded with a commercial EMPAD with a pixel resolution of 144 × 144 pixels and with 16 bits of dynamic range acquired for each position.

3. The acquisition time per diffraction pattern, or dwell time, is as low as 10 µs. The total image acquisition time can be of less than a second[1].

The volume of data generated must be transferred to a host PC with a data rate of at least 4.2 GB/s for real-time processing. Up to 55 GB of storage capacity would be required to acquire 20 images in a standard session.

Figure 1.2(a) illustrates the data transfer rate requirements in gigabytes per second (GB/s) as a function of the probe dwell time for three traditional commercial detector sizes: 128 × 128, 256 × 256, and 512 × 512. As the dwell time decreases (indicating faster data acquisition), the required bandwidth between the detector and the PC increases significantly. The transfer of such data can surpass the bandwidth capabilities of even the fastest data communication protocols used, for example, in ports for accessing DDR5 DRAM memory or USB4 ports found in personal computers, by up to two orders of magnitude. Therefore, the limiting factor for achieving faster acquisition speeds (minimum dwell time) in 4D-STEM lies with detector readout speed and storage rather than the capabilities of the scan coils or scan controllers [19].

Another limitation of EM is that the energetic beam of electrons can easily damage the sample under examination. This statement is particularly true with organic and biological samples that may undergo structural changes. Hence, reducing the electron dose is crucial for characterizing beam-sensitive materials with EM. This challenge is tackled by designing sensors that collect high-quality images with minimal electron doses.

The dose applied to the sample, measured in electrons per unit area, can be represented by the formula:

$$D = \frac{I_p \cdot C \cdot \delta_t}{(d_p)^2} \tag{1.1}$$

[1]State-of-the-art pixelated detectors used in 4D-STEM applications can work at dwell times ranging from 10 to 1000 µs and with pixel resolutions between 128 × 128 and 512 × 512.

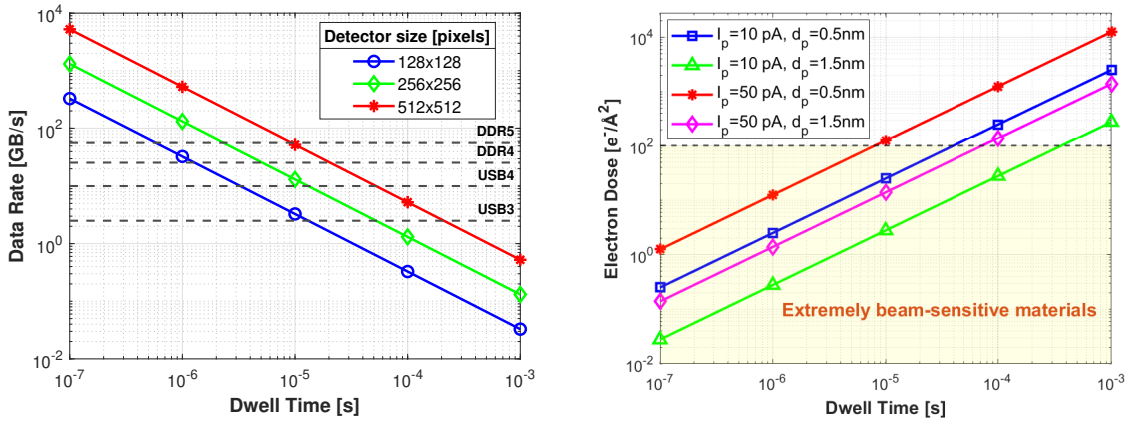

(a) (b)

Figure 1.2: Data rate and electron dose analysis for various EMPAD sizes in pixels and beam conditions as a function of dwell time. (a) Data rate (in GB/s) versus dwell time for different detector sizes and storing 16 bits of data for pixel. (b) Electron dose (in $e^-/\text{Å}^2$) versus dwell time for various beam current and probe diameter conditions. Electron doses under $100e^-/\text{Å}^2$) are required for imaging highly sensitive materials, such as organic crystals.

where I_p is the beam probe current, C the Coulomb charge of one electron, δ_t the dwell time, and d_p is the pixel width [2].

Given technological challenges in reducing δ_t, according to the equation 1.1, the dose D can be minimized by maintaining a low current or increasing the pixel width. Figure 1.2(b) shows the electron doses in $e^-/\text{Å}^2$ in the function of the dwell time in four conditions using STEM (two different current probes I_p and two different probe sizes d_p). The limited speed of detectors in EMPADs constrains the dwell time reduction necessary for dose minimization. Alternative strategies, such as increasing the probe size or reducing the beam current, either compromise resolution or reduce the signal-to-noise ratio, respectively. Achieving an optimal balance between dose and data quality remains a significant challenge. While 4D-STEM holds immense potential, designing EMPADs that can operate with ultra-low electron doses ($< 100e^-/\text{Å}^2$) required for imaging highly beam-sensitive materials, such as organic crystals, presents a substantial challenge for future research [20].

[2]This equation doesn't account for the deposited dose due to the flyback of the electron beam [19].

1.2. Objectives of this work

There is much interest in developing better image sensors for EM or EMPADs, which are transforming the field of EM. We believe that integrating neuromorphic strategies in such sensors can solve some of the significant challenges of their design. Therefore, our main objective has been implementing neuromorphic approaches in designing, fabricating, and testing microelectronics radhard pixels suitable for building better EMPADs.

1.2.1 Specific objectives

1. **Establish a Comprehensive Understanding of EMPADs:** Identify and analyze the current bottlenecks, critical performance parameters, and the latest advancements in EMPADs, with a specific focus on their limitations in CMOS technology through a detailed examination.

2. **Investigate Energy Detection in CMOS EMPADs:** Utilize the principles of neuromorphic engineering to investigate and develop innovative techniques for accurate energy detection and discrimination in CMOS-based EMPADs. This approach will enable the acquisition of energy-resolved information, such as electron energy loss spectra, alongside high-resolution imaging data, expanding the capabilities of EM for materials characterization.

3. **Propose a Neuromorphic EMPAD Design:** Propose a novel EMPAD architecture incorporating silicon retina approaches for direct and potentially indirect electron detection. This design will leverage neuromorphic principles to enhance data throughput, reduce redundancy, and enable real-time analysis of multi-dimensional data streams, including energy (color) information.

4. **Mitigate Radiation Hardening and Enhance Pixel Durability:** Explore and implement strategies to reduce radiation hardening effects in CMOS EMPADs, aiming to improve the durability and longevity of pixels, thereby ensuring sustained performance in high-radiation environments.

5. **Reduce Beam Exposure Time and Increase Information Rate:** Develop and evaluate methods to decrease beam exposition time while increasing the information rate in EMPADs, leveraging the event-driven nature of neuromorphic systems and optimizing data compression techniques.

6. **Couple and Synchronize Multiple Physical Parameters:** Investigate and implement methodologies for the coupling and synchronizing of various physical parameters (e.g., time, energy, position) within the neuromorphic EMPAD framework, enabling a more comprehensive and informative data acquisition process.

1.3. Dissertation organization

The dissertation is organized into four chapters apart from the introductory chapter.

In Chapter 2, we examine the specifications and challenges of designing image sensors for electron microscopes. We include a revision of the State-of-the-Art of EMPADs, both in research and commercialized. We focus more on those EMPADs that are of interest for their application in 4D-STEM. We finalize the chapter discussing neuromorphic strategies used in image sensors and how these can benefit EMPAD design.

In Chapter 3, we describe a novel neuromorphic pixel designed, fabricated, and tested during this thesis. The pixel has been optimized to be radhard at the electron energies used in SEM microscopes and can be integrated into a pixel array to be used as an EMPAD.

In Chapter 4, we explore two approaches to designing EMPADs with spectral sensitivity based on bioinspired solutions.

The last chapter of the dissertation discusses the results of this work and proposes routes for its continuation.

Finally, the document finishes with an annex and bibliography.

Chapter 2

EMPAD Challenges and the Neuromorphic Solution

EMPADs have revolutionized materials characterization, providing unprecedented insights at the atomic level through high-resolution imaging and spectroscopy. However, as the demands of modern electron microscopy escalate, so too do the challenges facing EMPAD technology. These detectors encounter escalating limitations in spatial and temporal resolution, sensitivity, efficiency, radiation hardness, and cost, hindering the full potential of advanced EM techniques, particularly in data-intensive applications like 4D-STEM.

This chapter thoroughly examines these challenges, exploring the underlying factors contributing to these limitations found in the state-of-the-art EMPAD design. We will explore the impact of charge sharing on the degradation of spatial resolution, the detrimental effects of coincidence loss on temporal resolution, and the inherent trade-offs between sensitivity, efficiency, and dynamic range. Further, we will address the complexities of achieving optimal energy resolution and ensuring radiation hardness in harsh operating conditions. The escalating costs associated with the fabrication, maintenance, and data management of high-performance EMPADs will also be considered.

In response to these limitations, we introduce the concept of information-centric EMPADs and explore the transformative potential of data-centric neuromorphic solutions. Inspired by the remarkable efficiency of biological neural networks, neuromorphic principles offer a novel paradigm for addressing the challenges faced by conventional EMPADs. We will discuss how implementing integrate-and-fire neurons and the

Address-Event Representation (AER) protocol can drastically reduce data redundancy, enhance temporal resolution, and enable real-time analysis, ultimately leading to more efficient and informative electron microscopy.

2.1. EMPADs: Direct vs. Indirect detection

Most EMPADs nowadays comprise a sensor array (pixels) and microelectronics circuits fabricated with CMOS technology. The readout electronics and the sensing part can be integrated or not together in a single silicon chip. EMPADs are different from conventional image sensors found, for example, in smartphones, in that they must be designed to withstand high-energy electron irradiation without being damaged [21]. Thus, most EMPADs are designed to be radhard, that is, resistant to radiation damage by one of three different post-CMOS manufacturing approaches: indirect, direct, or hybrid fabrication, described in the following three sections.

2.1.1 Indirect scintillator-based cameras

In this approach, the EMPAD comprises an array of pixels coupled to a scintillator. The pixels are fabricated using a Charge-Coupled Device (CCD) or Complementary Metal-Oxide Semiconductor (CMOS) technology. It is an indirect illumination approach where the electrons hit a cathodoluminescent material (*aka.*, scintillator) that emits low-energy monochromatic visible photons. These photons are optically guided to the sensor. This indirect approach is the most common because it is flexible, durable, and economical.

Unfortunately, the light emission process that occurs in the scintillator has a slow characteristic decay time that depends on the scintillator material, usually lasting over 0.5 µs and sometimes as long as 1.5 µs [19,22]. The decay time restricts how quickly the detector can record subsequent events, hindering the ability to achieve ultra-low dwell times and limiting their practical use in 4D-STEM. Moreover, other characteristics like noise, sensitivity, and image quality are degraded by the use of this indirect approach.

2.1.2 Direct back-thinned cameras

In the first decade of the XXI century, direct electron detectors (DEDs) for EM were commercialized for the first time. They were built with a CMOS Monolithic Active

Pixels Sensor (MAPS) that can be back-illuminated directly with electrons without converting them first into photons. These DEDs surpassed indirect cameras in sensitivity, dynamic range, and speed. They can be built with many pixels, which are necessary for taking high-resolution images of biological samples and have revolutionized the analysis of biomolecules with cryo-TEM due to their high sensitivity, in theory up to 1 single electron using post-processing [23]]. They are built with a MAPS whose silicon substrate is deeply back-thinned ($\sim 4 - 20\mu m$). As the sensor is back-illuminated, the substrate is the side of the die that is exposed to the electrons. The side with active circuits remains at the back and includes all the signal amplification, digitization, and readout electronics, as shown in Figure 2.1. Substrate thinning allows high-energy electrons to traverse the whole thickness of the chip (substrate and electronics), depositing only a fraction of their energy, which is then partly collected in the sensing area of the pixels integrated at the backside. Each pixel's output corresponds to the total accumulated charge in the standard charge integrating operational mode of MAPS detectors. However, the resulting images often suffer from Landau noise, arising from the inherent fluctuations in the energy deposited by individual electrons as they pass through the sensor [24].

The disadvantages of this method of fabricating radhard EMPADs include the fact that those back-thinned cameras are costly because they require non-standard manufacturing processes with a low yield. They cannot stand high electron doses (direct exposure to the electron beam can still damage them) and, therefore, have shorter operating lives. Finally, they are only effective with microscopes operating at high acceleration voltages > 160 kV so that the electrons can traverse the entire chip thickness.

2.1.3 Direct hybrid cameras

DEDs based on hybrid structures were developed first for high-energy physics applications in the CERN and then applied in EM. For example, in Gontard et al., a 10-channel silicon strip sensor was combined with a discrete electronics readout circuit demonstrating the detection of a single electron of 200 keV in a TEM [25]. Nowadays, the most successful DEDs are the Medipix family, which combines a CMOS MAPS with flip-chip integration, where the sensing of electrons and electronics readout areas are physically separated. Figure 2.1 shows a hybrid detector composed of a dedicated detector substrate interconnected with a MAPS by a layer of bump bonds. These detectors can be fine-tuned for various energy ranges by integrating materials and designs

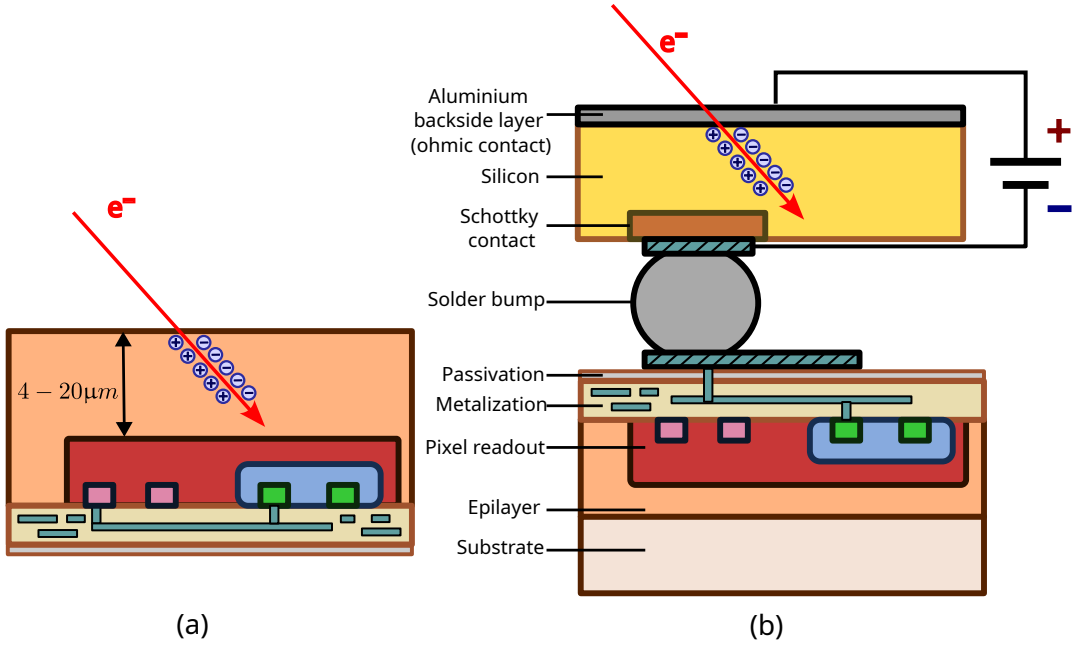

Figure 2.1: Cross sections views of the structure of two approaches for building direct electron detectors used for EM. (a) Back-thinned MAPS with an epi-layer to collect electron-hole pairs.(b) Hybrid pixel detector with the epi-layer connected to the pixel readout through a solder bump Adapted from [21].

optimized for specific beam energies, making them adaptable for low- and high-energy applications. They are state-of-the-art for material studies with 4D-STEM, with high frame rates, high dynamic range, high sensitivity (up to single electron counting), and high resistance to beam damage [23].

Hybrid EMPADs require costly fabrication technology. Moreover, the manufacturing process, underneath circuitry and inter-pixel charge sharing within the detector material, limits the minimum achievable pixel size [26, 27]. These constraints typically result in arrays with 256×256 pixels. Hence, they used to be unsuitable for acquiring high-resolution images like in cryo-TEM. Finally, hybrid-pixel detectors absorb electrons entirely within their pixels, which permits measuring their energy. This possibility allows, in principle, the acquisition of richer images in which each pixel would contain flux and spectral information. Unfortunately, current technologies using this approach only achieve an energy resolution of around 1 keV.

2.2. EMPADs specifications

The main product of EM is images of a sample. Therefore, most instrumentation developments seek to maximize image quality. The quality of an image is dependent on optical parameters and noise (electron source, acceleration voltage, focus and magnification, lens aberrations, electronic, environmental, and mechanical instabilities). Also, EMPADs are characterized by many specifications, which affect the quality of an image. In this section, we focus on reviewing the characteristics of EMPADs concerning parameters of interest for EM:

2.2.1 Spatial resolution:

Spatial resolution is a critical objective in EM, as it determines the level of detail that can be discerned within a specimen. It can be quantified on the image obtained (e.g., maximum recorded spatial frequency, SNR), which also depends on the properties of the EMPAD used to acquire the image. Two important metrics of an EMPAD related to spatial resolution are the point-spread function (PSF) and the modulation transfer function (MTF), which provide comprehensive descriptions of the EMPAD performance and the electron behavior within the sensor of the EMPAD.

The PSF encapsulates the spatial distribution of signal intensity from a point source, effectively quantifying the blurring or spreading introduced by the imaging system and electron-sample interactions. It provides insights into how a point object is "seen" by the detector, with a narrower PSF indicating sharper imaging.

The MTF, derived from the PSF, quantifies the detector's ability to transfer contrast across different spatial frequencies faithfully. It represents a given spatial frequency's output modulation (contrast) ratio to input modulation. A high MTF implies the detector can accurately reproduce fine details in the sample, while a low MTF indicates a loss of contrast and blurring of high-frequency features.

In the context of pixelated detectors like EMPADs, the Nyquist frequency emerges as a crucial concept. It represents the highest spatial frequency that can be unambiguously detected and is determined by the pixel pitch (center-to-center distance between pixels). The Nyquist frequency is typically half the sampling frequency, meaning that a detector can resolve features with a size no smaller than twice the pixel pitch. This relationship underscores the importance of pixel size in determining the theoretical

limit of spatial resolution.

Incorporating direct electron detectors (DEDs) into electron microscopy has catalyzed substantial improvements in resolution capabilities, pioneering a new era of experimental opportunities in diverse scientific domains [24]. This "resolution revolution" is mainly attributed to the superior image quality, efficient image acquisition, and the ability to compensate for sample motion during image capture that DEDs offer compared to traditional film-based and indirect scintillator-based technologies [21].

In the context of EMPADs, the spatial resolution, as well as PSF and MTF, are influenced by several factors, including:

Pixel count, pixel size and Charge-Sharing

The pursuit of enhanced spatial resolution in EM detectors naturally leads to a demand for smaller pixels, as pixel size directly limits the detector's ability to resolve fine details within a specimen. However, reducing pixel size introduces challenges related to charge sharing, which can significantly impact both spatial resolution and spectroscopic performance.

When an energetic electron interacts with the detector material, it generates a cascade of charge carriers (electron-hole pairs) that spread laterally within the sensor layer. Suppose the lateral spread of this charge cloud is comparable to or larger than the pixel pitch (distance between pixel centers). In that case, a significant portion of the charge may be collected by neighboring pixels [28], which increases the PSF and, in turn, reduces image quality. This low-resolution blurs details, posing limitations in techniques like TEM of the non-crystalline samples (e.g., biological specimens) or spectroscopy. In techniques like EELS, charge sharing degrades the quality of the acquired spectra as the energy information associated with the incident electron becomes distributed across multiple pixels [29].

Charge sharing can be corrected partially by data processing, for example, by fitting the signal of neighboring pixels to clusters of "hit" pixels [30]. This approach effectively reduces the impact of charge sharing on image quality, leading to improved spatial resolution and more accurate measurements. With some direct EMPADs that can detect and count single electrons, charge sharing can be used to pinpoint the location of an electron strike with sub-pixel precision, allowing for the creation of super-resolution images. In these images, the electron counting output from the detector

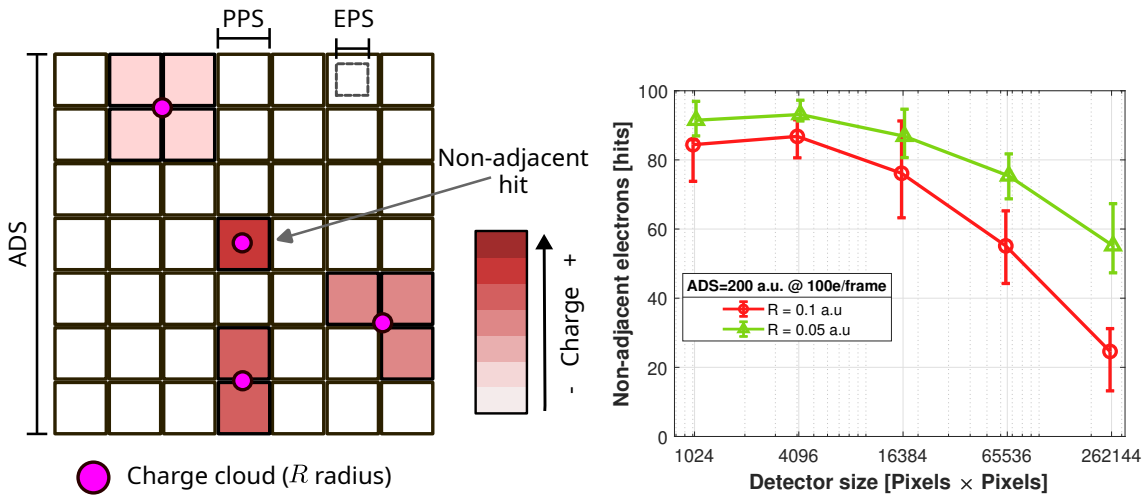

(a) (b)

Figure 2.2: (a) Diagram of the detector illustrating pixel arrangements and sizes, showing how charge distribution varies based on hit localization. (b) The plot shows the number of non-adjacent hits as a function of detector size in pixels for a fluence of 100 electrons per frame and two different charge radii.

contains more pixels than the physical number of pixels on the detector [31].

Figure 2.2 (a) illustrates a pixelated detector, showing how charge distribution varies based on hit localization. Each square represents a pixel, and the colors within the squares depict the intensity of the detected charge, with darker shades indicating higher charge levels. Two key metrics are illustrated: Physical Pixel Size (PPS) and Effective Pixel Size (EPS). The EPS denotes the area size within the charge generated by an electron hit that can be collected by a single pixel. If the charge cloud extends beyond the EPS, it can be shared among multiple pixels, potentially leading to non-adjacent hits. The magenta circles symbolize the charge clouds, characterized by their radius (R). Four different cases are shown: i) A detector hit occurs at the center of a pixel, creating charge solely within that pixel. The detector hit creates a charge distributed across ii) two pixels, iii) three pixels, and iv) four pixels.

Figure 2.2 (b) shows the simulation results investigating the relationship between the number of non-adjacent hits and the detector size expressed in pixels. The simulation assumes a constant fluence of 100 electrons per frame around 10 different runs and examines two scenarios with different charge cloud radii (0.1 and 0.05 arbitrary units). In both cases, the total active detector size (ADS) is kept constant at 200 arbitrary units and a uniform hit probability across all pixels. This plot shows that detectors with more pixels and identical sizes exhibit a more significant number of adjacent hits,

mainly when the charge cloud radius is more extensive. For example, a detector with 512×512 pixels would have almost 3/4 of the electron hits outside the EPS for a $R = 0.1$ a.u., in comparison with around 1/2 for the half charge radio $R = 0.05$ a.u. The incident electron's energy mainly influences the cloud radius [24].

EPS is a crucial parameter in semiconductor detectors as it determines the likelihood of charge sharing and, consequently, the occurrence of non-adjacent hits. This phenomenon is especially significant in detectors with higher pixel densities and events with larger charge cloud radii. For instance, the Hybrid Pixel Detector (HPD) are often less suitable for imaging applications due to their compromised spatial resolution, stemming from their relatively large pixel size ($\geq$ 55µm) mainly limited by charge sharing effects and the inability of accurately detect the impact point [32].

Understanding and mitigating charge-sharing effects is vital for optimizing the performance of semiconductor detectors in various applications.

2.2.2 Time resolution

Modern EMPADs allow the detection of single electron events. This capability introduces a paradigm shift in EMPADs from frame-based to data-driven acquisition schemes, with event-based electron representations (EER) gaining prominence. This transition promises enhanced temporal resolution and more efficient data handling. However, a standardized approach for implementing EER at the detector level remains elusive, leading to various challenges in achieving optimal time resolution.

One critical limitation in achieving high temporal resolution in EMPADs is coincidence loss, which arises when the detector cannot distinguish and register multiple electron arrivals occurring in rapid succession. This issue is exacerbated when using data-intensive techniques requiring high electron flux rates like 4D-STEM.

Several factors drive the need for improved time resolution:

1. The desire to reduce the beam exposure time for beam-sensitive samples, keeping the premise of every electron count.

2. The ability to perform faster image acquisition for real-time or in-situ measurements of dynamic processes.

3. The goal of reducing the PSF is achievable through data processing. For exam-

ple, in direct EMPADs, that means reducing charge-sharing effects by counting single electrons in neighboring pixels. Additionally, precise timing information is vital for accurate energy measurements in techniques like electron energy loss spectroscopy (EELS), as demonstrated in works using the Medipix family [33] or detectors like DECTRIS ELA [34]. In the TimePix family, each pixel or sensor segment produces a pulse with a width proportional to the energy absorbed in that area [35].

In the next section, we will discuss the technical challenges of achieving high time resolution in modern EMPADs, focusing on coincidence losses and their impact on various EM techniques.

Coincidence loss

This phenomenon arises when multiple electrons strike the same detector area within a short time frame, leading to the undercounting of actual electron events and subsequent degradation of image quality [36].

EMPADs can register individual electron impacts when operating in electron counting mode to enhance Detective Quantum Efficiency (DQE)[1]. While counting offers advantages such as improved DQE, potential resolution doubling, and noise reduction [37], it is susceptible to coincidence loss. When multiple electrons hit the same region within the detector's dead time, they may be erroneously counted as a single event, resulting in information loss and inaccurate electron counts [37,38]. Coincidence loss directly affects the temporal resolution of EMPADs, degrading their ability to distinguish events occurring in rapid succession and limiting the highest minimum exposure rate [38], as higher exposure rates increase the likelihood of coincidence loss. There is a dead time during which a system (detector) cannot process new signals, including the time to acquire, convert, and read out the signal.

The sparsity of the electron signal in each frame is crucial for successful electron counting. Insufficiently sparse signals increase the probability of coincidence loss, for example, 4D-STEM diffraction patterns, necessitating operation at lower exposure rates to maintain accurate counting. This trade-off is evident in the contrasting frame

[1]DQE is a key metric used to describe the performance of imaging detectors, particularly in fields such as medical imaging, radiography, astronomy, and particle physics. It measures how efficiently an imaging system can transfer the information content of the input signal (e.g., light, X-rays, or particles) to the final image, considering both the signal and noise.

rates between charge-integrating and counting modes. While high frame rates in the charge-integrating mode can capture multiple electrons per pixel per frame, ensuring adequate signal-to-noise levels, sparse individual frames in the counting mode require the summation of numerous frames for meaningful analysis [37, 38].

For instance, to maintain a coincidence loss below 5%, frame-based EMPADs should not exceed an exposure rate of roughly eight electrons per pixel per second [36]. This limitation underscores the challenge of balancing high temporal resolution with low coincidence loss, a critical consideration in optimizing EMPAD performance for time-resolved electron microscopy applications.

Figure 2.3 illustrates the impact of coincidence loss on the performance of simulated EMPADs under varying conditions of incident current (I_p) and dead time. The simulations were conducted for detector arrays with varying pixel resolutions (128×128, 256×256, and 512×512), assuming a resolution time of 100 ns and uniform hit probability across all pixels.

In Figure 2.3 (a), the detector count (hits/ms) is shown as a function of the incident current (I_p). The theoretical curve (dashed blue line), representing an ideal detector with no coincidence loss, exhibits a linear relationship between the count rate and incident current. The simulated data for all three array sizes initially follow this linear trend at lower currents. However, as the incident current increases, the 128×128 array deviates significantly from the theoretical expectation, indicating the onset of coincidence loss. The 256×256 and 512×512 arrays show greater resilience to coincidence loss, maintaining closer adherence to the theoretical curve at higher currents. This result indicates that by distributing the electron flux over more pixels, larger arrays experience reduced coincidence loss effects.

Figure 2.3 (b) depicts the detector count (hits/ms) as a function of dead time, with a fixed incident current of 10 pA. The theoretical curve, again representing an ideal detector, remains constant across all dead times. The simulated data reveal a clear dependence of coincidence loss on dead time. The 128×128 array experiences a dramatic decrease in count rate as the dead time increases, highlighting its vulnerability to coincidence losses. The 256×256 array exhibits improved performance, while the 512×512 array closely follows the theoretical curve, demonstrating minimal coincidence loss even at longer dead times. This result further emphasizes the advantage of larger pixel arrays in mitigating coincidence loss effects. Coincidence loss leads to the undercounting

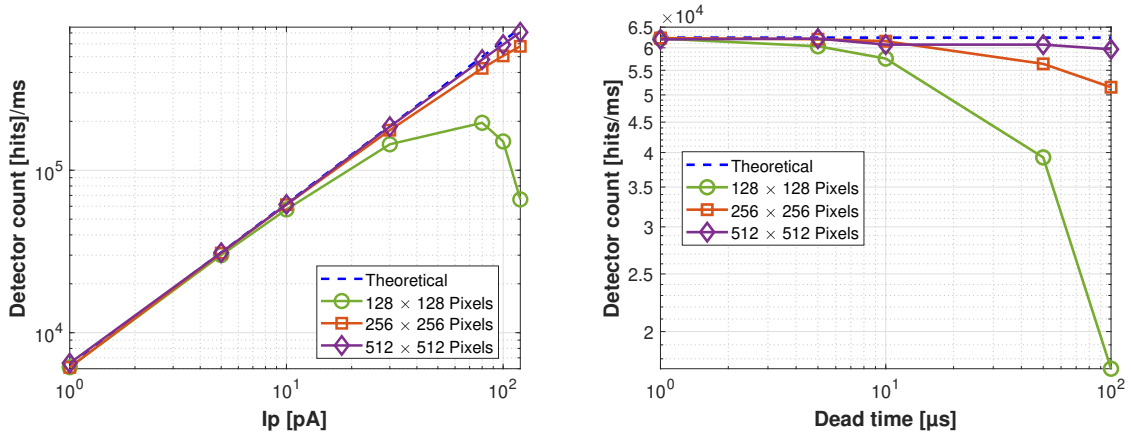

(a) (b)

Figure 2.3: Coincidence loss in time for detector arrays with varying pixel resolutions. (a) Detector count as a function of incident current (I_p) for a fixed dead time of 10 µs. (b) Detector count as a function of dead time for a fixed incident current of 10 pA. Both plots compare theoretical values with simulated data for arrays of 128 × 128, 256 × 256, and 512 × 512 pixels, assuming a resolution time of 100 ns and uniform hit probability across all pixels.

of electrons, which can negatively affect quantitative analysis and limit the detector's maximum achievable count rate and temporal resolution.

Readout Speed

The advent of 4D-STEM techniques, coupled with the increasing pixel density of modern EMPADs and the ever-accelerating scan speeds, has led to a massive surge in experimental data rates [19]. Despite the impressive advancements in frame rates achieved by modern direct detectors, with dwell times as low as 10 µm, a significant bottleneck remains in transferring this vast amount of data from the detector to the processing unit [39].

Irrespective of the specific EM application, operating high-speed electron detectors at their total capacity inevitably generates enormous quantities of raw data. This reality poses substantial challenges for data handling and processing [40, 41]. While reducing the data volume through compression or selective readout can alleviate this issue, it often comes at the cost of information loss. This trade-off is evident in cryo-EM, where individual electron readouts are combined within frames, sacrificing some level of detail.

The sheer volume of data generated by modern EMPADs is exemplified by prac-

tical pixelated STEM scans acquired with the Gatan K2 IS detector, which can easily reach 200 GB per scan, with entire sessions producing terabytes of data [42]. As technology progresses and faster cameras, storage, and processing systems become available, these data volumes are only expected to increase exponentially. This data bottleneck poses a significant hurdle in realizing the full potential of high-speed EMPADs.

Sensitivity and noise

The detector's sensitivity or ability to convert incoming electrons into measurable signals is an important property quantified with Quantum Efficiency (QE). High QE indicates efficient conversion, minimizing information loss during detection. It is formally defined as the ratio of detected electrons to the total number of incident electrons. QE of a detector denotes the average fraction of the input quanta that contributes to generating the output signal [43].

DQE extends beyond QE by incorporating the detector's noise characteristics. DQE can be defined as the ratio of the square of the output signal-to-noise ratio (SNR_{OUT}) to the square of the input SNR_{IN}:

$$DQE = \frac{SNR_{OUT}^2}{SNR_{IN}^2} \tag{2.1}$$

For two-dimensional linear imaging systems, it is appropriate to extend the concept of DQE into the spatial frequency domain (μ, ν) [44]. This results in the following formulation:

$$DQE(\mu, \nu) = \frac{MTF(\mu, \nu)^2}{NNPS(\mu, \nu)} \cdot \frac{1}{Q} \tag{2.2}$$

Here, MTF represents the Modulation Transfer Function, NNPS denotes the Normalized Noise Power Spectrum (calculated by dividing the NPS by the mean output signal), and Q signifies the incoming electron flux density, equivalent to the SNR_{IN}^2 under Poisson statistics [45].

An ideal detector would have a DQE of unity, perfectly preserving the SNR. However, real-world detectors introduce additional noise due to various factors, including the physics of particle detection, signal generation mechanisms, and signal processing [45]. This noise inevitably reduces the DQE, making it a more comprehensive metric of detector performance than QE alone.

Achieving high QE and DQE involves unavoidable trade-offs with other detector

characteristics. For instance, increasing the detector's sensitivity to low-dose signals may necessitate larger pixels or thicker sensor layers, which can compromise spatial resolution and increase charge sharing [46]. Centroiding techniques, while improving spatial localization and MTF, can also increase the high-frequency component of the noise power spectrum (NNPS), thereby degrading the DQE in that range [47]. While a high modulation transfer function (MTF) is generally desirable for resolving fine details, applications like cryo-EM and cryo-tomography, where radiation damage limits the total dose, prioritize high DQE over MTF for enhanced sensitivity in low-dose regimes [46].

2.2.3 Energy resolution

Spectrometry such as EELS or Energy Dispersive X-rays (EDX) combined with imaging capabilities makes EM a potent characterization tool of materials. EELS acquisition in TEM or STEM is done with EMPADs attached to the output of electromagnetic filters. In SEM, EELS is not usually recorded[2].

Recent advances in instrumentation have enabled the recording of EELS spectra with a very high energy resolution of the order 0.1 eV, enough for resolving the finest features in the spectrum, which has significantly propelled EELS capabilities. EM and EELS with sub-eV energy resolution can now provide spatially resolved insights into elemental composition, chemical bonding, optical properties, and vibrational modes of matter at the atomic level. However, there are several challenges in achieving the best performance (i.e., EELS spectra with the highest energy resolution). The recorded spectrum (R) in a detector is a convolution of the inherent energy-loss function (E_{LF}) of the sample, the energy spread of the electron source (E_S), and the zero-loss peak[3] (ZLP) [49, 50]:

$$R = E_{LF} \otimes (E_S \otimes \mathrm{LSF}) = E_{LF} \otimes ZLP \tag{2.3}$$

Nevertheless, the resolution is degraded due to the EMPAD used for recording

[2]Nonetheless, because SEM operates at electron beam energies below 30 keV, it may offer advantages listed in Table 2.1 such as reduced knock-on damage of the sample and lower costs of the spectrometer [48].

[3]The ZLP is the most intense feature of an EELS spectrum represents electrons that interact with the sample without significant energy loss (elastically scattered) and its width provides a robust measure of the energy resolution of the spectrometer.

the signal. In other words, the spectrum is convolved with the detector's PSF, and the ZLP's shape reflects the energy distribution of the electron source convolved with the detector's degradation [49]. By taking the ZLP's Fourier transform, an approximation of the modulation transfer function (MTF) of the EMPAD used for recording the spectrum can be obtained.

In scintillator-based EMPADs, photon scattering within the scintillator and electron backscattering from the fiber optics contribute to energy resolution degradation [51]. Conversely, direct detection EMPADs offer advantages due to their high signal-to-noise ratio (SNR), which enables electron counting and eliminates electronic readout noise and noise from variations in deposited energy per electron [50]. Back-thinned CMOS detectors are not used for EELS recording due to the lower dynamic range and low-intensity saturation, making them unsuitable for recording very intense signals like the ZLP [34]. Alternative approaches have also been explored, such as hybrid pixel detectors with EELS based on time-of-flight (ToF) measurements [52].

2.2.4 Dynamic Range

In addition to sensitivity and efficiency, an EMPAD's dynamic range is crucial. It represents the range of electron intensities the detector can accurately measure, from the lowest detectable signal to the highest without saturation.

EM applications often encounter a wide range of intensities, like diffraction patterns or EELS spectra, requiring detectors with a broad dynamic range to capture weak and intense signals without sacrificing accuracy. This scenario is exemplified by a typical EELS map, where the SiK edge might exhibit 10^2 counts. At the same time, the ZLP intensity can reach 2×10^9 counts—a disparity of nearly six orders of magnitude around 2 keV. Such intense ZLP signals can potentially damage detector pixels. Another interesting example of this challenge arises in 4D-STEM, where the simultaneous capture of CBED patterns and the bright central disk demands an exceptional dynamic range in the detector. This disparity in intensities can span several orders of magnitude, posing a significant challenge for conventional detectors [18].

2.2.5 Radiation damage

The harsh electron radiation environment of electron microscopes (EM) poses significant challenges to the longevity and performance of the EMPADS, especially the

back-thinned ones. When MAPS arrays are used for radiation imaging, they must be designed to be radiation hard or *radhard* as highly energetic particles can damage electronics circuitry, inducing malfunction or even destroying the sensor. The total absorbed dose of ionizing radiation is measured in Grays (Gy) for the SI, and it quantifies how much energy from ionizing radiation is absorbed by matter[4]. In the case of an EMPAD made of Silicon, it would be how much energy is deposited in the silicon substrate when irradiated with the electrons. Meanwhile, indirect and hybrid EMPADs are highly radhard.

The dominant concern is the cumulative dose effects, encompassing Total Ionizing Dose (TID) and displacement damage (DD) [53]. The cumulative dose effects arise from the detector's continuous exposure to the radiation beam over time. TID refers to the total amount of ionization energy deposited in the detector material, primarily affecting the oxide layers of CMOS transistors [54]. This ionization can lead to trapped electron-hole pairs, altering transistor characteristics and causing increased leakage currents and variations of the voltage threshold [55]. In severe cases, the trapped charges can damage the silicon-oxide interface, creating dangling silicon bonds and compromising detector performance. DD occurs when high-energy electrons displace atoms from their lattice positions in the detector material, creating defects that degrade charge collection efficiency and increase noise levels. The susceptibility to TID and DD varies depending on the detector material and design, with back-thinned detectors generally being more vulnerable because their circuitry is directly exposed to the radiation.

Beyond cumulative dose effects, single-event effects (SEEs) can also threaten EMPADs in EM. SEEs are transient malfunctions caused by a single ionizing particle (e.g., an electron) interacting with a sensitive node within the detector circuitry. This probability is further amplified in modern nanometer-scale CMOS processes, where the critical charge Q_{crit} required to trigger a SEE decreases as device dimensions shrink [56]. Two prominent SEEs in EMPADs are Single Event Upsets (SEUs) and Single Event Transients (SETs). SEUs manifest as changes in the state of storage elements, such as memory cells, potentially leading to data corruption or miscounting of events. SETs, on the other hand, are temporary voltage spikes in circuit nodes, which can cause unintended comparator triggers or even broader circuit malfunctions.

[4] 1 Gray is defined as the absorption of one joule of radiation energy per kilogram of matter. Before the adoption of the Gray, the unit used to measure absorbed radiation dose was the **rad** (radiation absorbed dose). The relationship between the Gray and the rad is: 1 Gray (1 Gy) = 100 rad

Mitigating radiation-induced damage in back-thinned EMPADs involves a combination of strategies, including radiation-hardened materials and designs, error detection and correction mechanisms, and redundancy in critical components. For instance, Enclosed Layout Transistor (ELT) designs in the analog parts of the pixel circuitry can significantly improve resistance to radiation effects [57]. ELT-enclosed geometry helps reduce the build-up of trapped charges within the oxide layers and at the silicon-oxide interface. This design minimizes the areas where charge trapping can occur, thereby decreasing radiation-induced leakage currents and threshold voltage shifts.

2.2.6 Cost

The pursuit of high-performance EMPADs, such as back-thinned and hybrid EMPADs, comes with a significant financial burden because they are still niche applications made with non-standard fabrication and post-fabrication technologies and, in some cases, with low yield. Moreover, techniques like 4D-STEM require high frame/pixel acquisition rates that generate massive amounts of data, requiring substantial data storage and high-performance computing infrastructure investments [58]. Both factors imply that the cost of high-end EMPADs can be prohibitive for smaller research institutions and may complicate the widespread adoption of cutting-edge EM technologies.

Beyond the financial implications of data storage and processing, other cost factors associated with modern EMPADs include:

1. **Detector Fabrication:** The fabrication of modern EMPADs, particularly those back-thinned with high pixel density and sophisticated readout electronics, is a complex and expensive process. Moreover, deep mechanical thinning of the chip substrate from a standard thickness of around 300 μm down to the 50 μm thickness needed in EM applications is expensive. Also, it reduces the fabrication yield dramatically as the thin chip becomes very fragile. In hybrid EMPADs, one of the significant cost drivers is the bump-bonding technique, which connects the sensor chip to the readout integrated circuit (ROIC). The bump-bonding process often dominates pixel detectors' production costs and schedules. Researchers are actively exploring alternative bonding techniques and simplified designs to reduce fabrication costs [59].

2. **Maintenance and yield:** In addition to fabrication costs, the maintenance and durability of EMPADs are also important considerations. These detectors are

subjected to high-energy electron beams and other forms of radiation, which can lead to radiation damage over time and reduce their lifespan. One common issue is the development of hot pixels, which exhibit abnormally high dark current due to radiation-induced defects [60].

2.3. EMPADs for 4D-STEM-in-SEM

Table 2.1 illustrates the potential advantages of implementing 4D-STEM techniques in SEMs (STEM-in-SEM) instead of in TEMs. SEMs are generally more accessible and less expensive than transmission electron microscopes (TEM). Additionally, the lower beam energies used in SEM (typically below 30 keV) can reduce sample damage (e.g., knock-on damage), a critical concern for studying beam-sensitive materials with EM. The increased scattering cross-sections at lower energies can also enhance the signal-to-noise ratio and improve the quality of diffraction patterns. Furthermore, SEMs offer a more extensive range of length scales for analysis. All these reasons make SEMs an attractive platform for implementing a technique like 4D-STEM [61].

Table 2.1. *4D-STEM implementation in SEM.*

Pros:	**Cons:**
✓ Easier Access (more SEMs available)	✗ Lower detection efficiency (less energy deposited by diffracted electrons)
✓ Reduced damage (Beam energies < 30 keV)	✗ Limited spatial resolution
✓ Increased scattering cross sections (lower energies)	✗ Non-correlative EELS spectroscopy
✓ Larger range of length scales	✗ Non standard integration of commercial EMPADs

2.4. Information-centric EMPADs

Electron microscopy is undergoing a paradigm shift towards information-centric EMPADs. This approach prioritizes extracting the most comprehensive information from each detected electron, ideally including individual hit location, energy, momentum, and spin, rather than solely maximizing the total number of detected electrons [62,63]. Traditional EMPADs often generate vast amounts of redundant data due to their frame-based readout mechanisms. This redundancy increases data storage and processing

requirements, impedes real-time analysis, and can lead to information bottlenecks.

2.4.1 Data reduction technologies

A crucial distinction exists between raw data and the information it encodes. Traditionally, frame-based cameras prioritize the transmission of the entire raw data stream of images, which can be vast and cumbersome. This data includes many elements, such as an integrated analog signal at each pixel, numerical representations of detected electron events, zero values for empty regions, and protocol headers for communication management. Furthermore, frame-based sensors often acquire redundant data due to repeated pixel readouts, even when the intensity does not change. However, a more efficient approach focuses on extracting and transmitting only the essential information embedded within the raw data. This information-centric strategy, inspired by Claude Shannon's theory of information entropy [64], aims to minimize data volume while preserving the scientific value of the acquired information.

Several options can be implemented to manage and reduce this data volume:

1. **On-the-Fly data compression:** By analyzing the data's entropy, efficient encoding schemes (such as Huffman coding or arithmetic coding) can compress the data in real time without any loss of information. The idea is to use shorter codes for more frequent patterns and more extended codes for less frequent patterns. This strategy can also involve filtering or feature extraction based on predefined criteria. However, implementing on-the-fly compression near the sensor readout can demand significant power processing inside or in proximity to it. This computational demand can lead to localized heat generation and increased latency, potentially challenging system design and performance.

   For example, the 4D camera presented in [58] achieves frame rates up to 87 kHz. A dedicated acquisition system was developed to handle the massive data rate (up to 480 Gbit/s). This system consists of four field-programmable gate arrays (FPGAs), each processing a quarter of each frame in parallel. A fifth server is dedicated to storage, data reduction, and image processing. However, such intricate hardware implementations can be costly and complex, potentially limiting their widespread adoption. An alternative approach, denominated as Dual Space Compressive Sensing (DHCS) [65], proposes subsampling 4D-STEM data, but its algorithmic complexity poses challenges for practical implementation.

2. **Pixel binning strategies:** This technique combines multiple pixels into larger "superpixels," reducing the overall data size while maintaining essential information. It also reduces the channel's bandwidth requirements for the interface with the PC and can eventually decrease the dwell time but compromise spatial resolution [45, 66, 67].

3. **Region of Interest (ROI) Scanning:** Focusing the scanning and data collection on specific regions of interest within the sample reduces the overall data volume. Still, it sacrifices the Field of View (FoV) [68–70].

4. **Post-Acquisition Compression:** While on-the-fly compression reduces data transmission, it shifts the computational burden and complexity to the sensor readout. These issues can be mitigated by performing compression on the PC or server side. Software packages such as Stempy [71] and LiberTEM [72] exploit node parallelism and utilize back-ends like CUDA or OpenMP to accelerate computations across multiple processing units. This approach significantly speeds up data analysis and reconstruction tasks, enabling more efficient handling of large datasets. Notably, some electron microscopy detectors, such as the K3 camera from Gatan, incorporate GPUs directly within the detector to optimize and expedite computational processes.

   This practice is one of the most adopted in works dealing with extensive 4D-STEM data experiments but may require copious resources for transferring and storing the datasets [73, 74]. An alternative, proposed by the company Thermo Fisher Scientific, utilizes event-driven representations in a format called Electron Event Representation (EER) [75]. This approach processes acquired raw points on the server side and obtains each detected electron's position and arrival time, resulting in significantly smaller files than traditional compressed movie formats. Despite the size reduction, a bottleneck remains at the detector readout stage, hindering the system's overall efficiency.

2.4.2 Entropy, Information, and AER encoding

Communication fundamentally involves transmitting information from a source to a destination through a channel. In the context of the EMPADs, the communication principles translate to the transfer of data generated by the detector (the source) to an external processing system (the destination). The channel through which this informa-

tion flows is typically a high-speed digital interface, such as Universal Serial Bus (USB) or Low-Voltage Differential Signaling (LVDS). Before transmission, the message ($\mathbf{S}$) is encoded by a function ($g = f(\mathbf{X})$) into a suitable format ($\mathbf{X}$) for the channel. This encoding can range from simple identity mapping (no change) to complex compression schemes that remove redundancy.

In 1948, Claude Shannon established the fundamental limits of communication through the concept of information entropy [64]. Shannon defined the bit as the basic unit of uncertainty (information), not merely as a binary digit [76]. The Shannon entropy, H($\mathbf{X}$), quantifies the minimum number of bits needed to represent a message $\mathbf{X}$, given by:

$$H(\mathbf{X}) = -\sum_{i=1}^{n} p_i \log_2 p_i \tag{2.4}$$

where p_i represents the probability of occurrence of the i-th symbol in the message, and n is the number of symbols in the message alphabet.

For example, consider two messages, $\mathbf{X}_1$ and $\mathbf{X}_2$, each consisting of four symbols (A, B, C, D). In $\mathbf{X}_1$, the symbols occur with equal probability (0.25 each). In $\mathbf{X}_2$, the symbol A occurs with a probability of 0.8, while B, C, and D each occur with a probability of 0.067. Calculating the entropy for each message:

$$H(\mathbf{X}_1) = -4 \cdot [0.25 \log_2(0.25)] = 2 \text{ bits} \tag{2.5}$$

$$H(\mathbf{X}_2) = -\left[0.8 \log_2(0.8) + 3 \cdot 0.067 \log_2(0.067)\right] = 0.72 \text{ bits} \tag{2.6}$$

The lower entropy of $\mathbf{X}_2$ (0.72 bits) compared to $\mathbf{X}_1$ (2 bits) signifies that $\mathbf{X}_2$ is more predictable, contains less information content, or is more redundant than $\mathbf{X}_1$. This result has practical implications for encoding and compression. Specifically, a new encoding system could compress $\mathbf{X}_2$ more efficiently than $\mathbf{X}_1$, as there is less unique information to represent in $\mathbf{X}_2$.

Shannon's theory of information is deeply interlaced with the principles of asynchronous AER communication. By transmitting only events that represent significant changes in the input, AER inherently reduces redundancy and maximizes the information content of the transmitted data.

Entropy in EMPADs

Electron counting in EMPADs can be modeled as a Bernoulli process, where each pixel within a frame has two possible outcomes: either it is hit by an electron (1) or not (0). The probability of a pixel being hit, denoted as p, is determined by the ratio of the camera exposure rate (electrons per pixel per second - eps) to the camera frame rate (frames per second) [75]:

$$p = \frac{\text{camera exposure rate}}{\text{camera frame rate}} \tag{2.7}$$

Given this Bernoulli model [22, 77], the Shannon entropy (H) of the pixel stream quantifies the average information content per pixel:

$$H(p) = -[p \log_2 p + (1-p) \log_2 (1-p)] \tag{2.8}$$

This entropy value represents a theoretical lower bound on the number of bits per pixel required to encode all the events (electron hits) within a counted frame. Achieving this lower bound necessitates a statistical model that accurately reflects the data's distribution and utilizes an optimal data compression scheme [76].

In terms of entropy per frame for a pixelated electron detector with N_{Pix} pixels, the entropy can be given by:

$$H_{frame}(p, N_{Pix}) = -N_{Pix} \cdot [p \log_2 p + (1-p) \log_2 (1-p)] \tag{2.9}$$

Consequently, the optimally compressed file size in bytes per second of exposure can be given by:

$$D(p, N_{Pix}, N_{frame}) = -\frac{1}{8} \cdot N_{frame} \cdot N_{Pix} \cdot [p \log_2 p + (1-p) \log_2 (1-p)] \tag{2.10}$$

where N_{frame} is the frame rate in frames per second (fps). Increasing the frame rate (and thus decreasing p) reduces the likelihood of multiple electrons hitting the same pixel within a frame, mitigating coincidence losses and improving temporal resolution. However, this approach can also lead to lower signal-to-noise ratios due to fewer

detected electrons per frame. On the other hand, decreasing the frame rate (increasing p) may improve the signal-to-noise ratio by capturing more electrons per frame. This advantage, however, is accompanied by an increased risk of coincidence losses and a reduction in temporal resolution.

2.5. EMPADs: State-of-the-Art

Specifications of EMPAD sensors vary widely depending on the application. Table 2.2 compiles the most crucial specifications in three categories: diffraction imaging, life science, and materials science. This thesis will address the challenges of acquiring data using electron diffraction (the foundation of 4D-STEM techniques). Compared to conventional EM, 4D-STEM applications are the most demanding regarding speed (frame rate per second or fps), Dynamic Range (DR), and radiation hardness.

Table 2.2. *Specs of image sensors on electron microscopy. Adapted from [78].*

	Diffraction Imaging	**Life Science**	**Materials Science**
Pixel Array	< 1 k $\times$ 1 k	> 4 k $\times$ 4 k	> 1 k $\times$ 1 k
Dynamic Range	Single-electron up to 10^5 e^-/pix/frame	Single-electron	$20 - 200$ e^- /pix/frame
Radiation Hardness [(a)] (1 year use)	$\sim$ 20 Grad	$\sim$ 20 Mrad	$\sim$ 1 Mrad
Frame Rate [fps]	> 1000/s	> 40/s	> 100/s
[(a)] Due to Total Ionization Dose (TID).			

Figure 2.4 illustrates the evolution of semiconductor detectors over the last 30 years, highlighting their performance in terms of pixel count, frames per second (fps), and dwell time. The detectors are categorized into CCD/CMOS, hybrid pixel detectors, a specialized region for annular detectors used in STEM (purple), and advanced pixelated detectors for 4D-STEM applications (green).

CCD/CMOS detectors, such as the K2 (2012) and K3 (2021), are characterized by high pixel counts, reaching up to 5760×4092 pixels in the K3 model. However, they operate at lower frame rates, typically under 100 fps, making them more suitable for high-resolution imaging with longer integration times than for applications requiring high frame rates. While some 4D-STEM studies have utilized these detectors, such as in [79] with the K3 IS detector at 600 fps, they often result in higher dose rates ($>$ 1000 $e^-/\text{Å}^2$) for the specimen compared to hybrid pixel detectors. Other studies, like

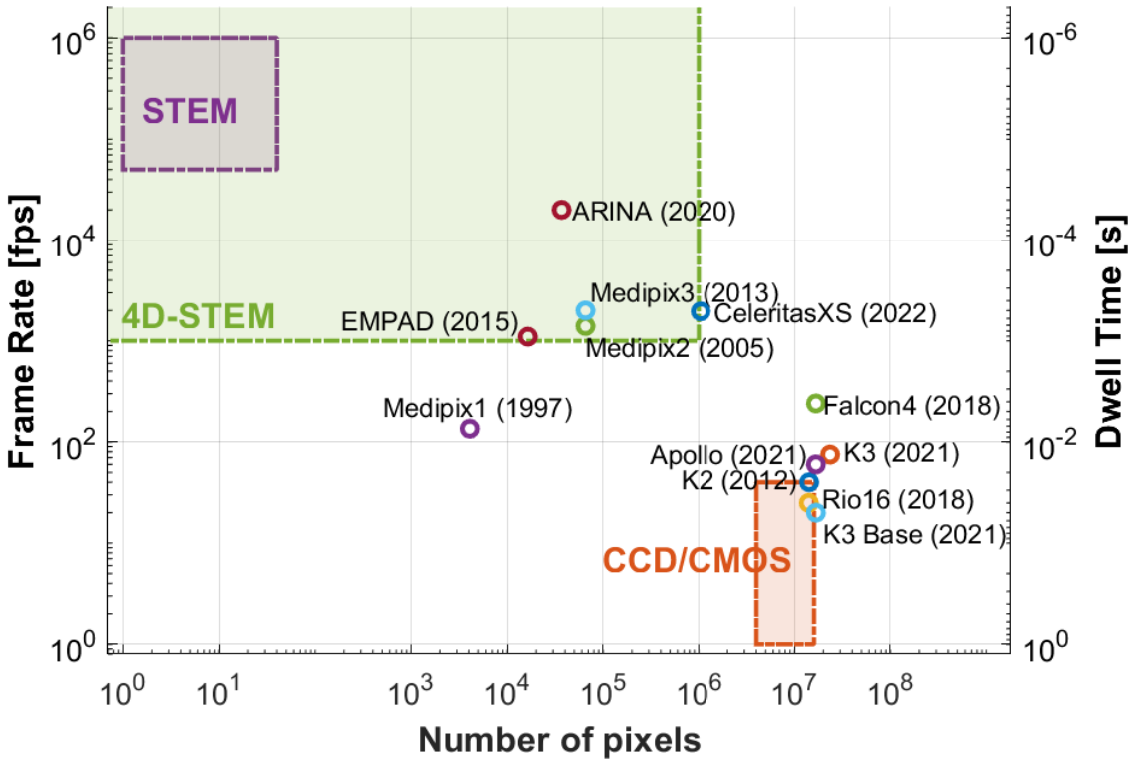

Figure 2.4: Comparison of conventional STEM and 4D-STEM. Adapted from [19]. (a) In STEM, monolithic detectors are used in different angular regions to capture diffraction patterns. (b) In 4D-STEM, the CBED pattern is stored at each point, generating a 4D-STEM dataset.

those employing integrated differential phase contrast (iDPC) STEM with the Falcon 4 detector, have reached doses of 350 $e^-/\text{Å}^2$ [80], which still exceeds the tolerance of ultra-beam-sensitive materials.

Hybrid pixel detectors, exemplified by the Medipix series and Thermo Fisher Scientific EMPAD[5] (2015), occupying the middle ground between pixel count and frame rate. They achieve this balance by integrating advanced detection materials with application-specific integrated circuits (ASICs). The Medipix series has seen significant advancements since its inception with Medipix1 in 1997. Subsequent generations, including Medipix2 [81], Timepix [82], and Medipix3 [83], have substantially enhanced dynamic range, resolution, and overall performance. Notably, the Timepix variant enables precise timing of electron/particle events, a crucial feature for specific STEM applications. It is worth noting that while the Medipix/Timepix architecture is available

[5]In this document, "EMPAD" is used as a general term to refer to any pixelated detector for electron microscopy unless otherwise specified. This should be distinguished from the "EMPAD" sensor produced explicitly by Thermo Fisher Scientific.

for licensing, various commercial implementations exist beyond those mentioned in the figure. In recent years, most publications involving 4D-STEM on beam-sensitive materials have utilized hybrid pixel detectors. For example, doses as low as 300 $e^-/Å^2$ have been achieved with the Timepix3 detector [84]. In another case, using the ARINA detector was reported a specimen dose of 3 $e^-/Å^2$ with a dwell time of 14 µs and a pixel size of 100 $µm^2$ [85].

The Celeritas XS, representing a MAPS sensor, balances resolution and speed using backside sensing technology. Studies have employed this detector to create 5D collections for capturing the dynamics of metallic supercooled liquids (SCLs) [86]. However, in the best cases, this approach reached doses around 5000 $e^-/Å^2$. Lower doses can be applied by employing ultra-low currents (0.4 pA), but at the expense of dynamic range and time resolution [87].

Table 2.5 provides a comprehensive overview of the state-of-the-art EMPAD sensors, highlighting key specifications pertinent to their performance and application in EM. The table details the exact detectors used in Figure 1.1.

The Medipix1, Medipix2, and Medipix3 detectors, developed by CERN, exhibit pixel sizes ranging from 55 µm to 170 µm and array sizes up to 256 × 256 pixels. These hybrid detectors utilize frame-based readout technology, achieving impressive frame rates of up to 3759 fps in parallel readout mode, making them ideal for high-speed counting applications. Gatan's K2 and K3 detectors, classified as Monolithic Active Pixel Sensors (MAPS), offer significantly smaller pixel sizes of 5 µm and larger array sizes, reaching up to 5760 × 4092 pixels. These detectors also feature frame-based readout systems, with the K3 achieving a remarkable frame rate of 1500 fps, suitable for high-resolution and high-speed imaging.

The Falcon 4 detector by Thermo Fisher Scientific employs EER technology, a data compression approach on the PC side. It combines a substantial array size of 4096 × 4096 pixels with a moderate pixel size of 14 µm, supporting frame rates of up to 250 fps. Similarly, the EMPAD by the same manufacturer offers a hybrid design with a pixel size of 150 µm and an array size of 128 × 128 pixels, operating at an impressive frame rate of 1100 fps.

The Rio 16 detector, utilizing indirect scintillator-based technology, features an extensive array size of 4096 × 4096 pixels with a smaller pixel size of 9µm. However,

its frame rate is comparatively lower at 20 fps, which is suitable for applications with no strict dwell time restrictions.

Direct Electron's Celeritas detector, with a pixel size of 15µm and an array size of 1024×1024 pixels, employs frame-based MAPS technology to achieve a high frame rate of 1960 fps, making it highly effective for rapid counting applications.

The Apollo is a DED also developed by Direct Electron. It utilizes a novel event-based MAPS detector specifically designed for high-speed electron counting. The sensor comprises 4096×4096 physical pixels, each measuring 8 µm. It incorporates on-chip correlated double sampling (CDS) for automatic noise subtraction within each pixel to mitigate noise. The detector also features a sense amplifier for thresholding and event identification and a priority encoder for packaging and outputting detection events. Despite event detection enabling faster transmission, the detector still requires a considerable exposure time to capture enough level signal [88].

Lastly, the ARINA detector by Dectris stands out with its hybrid design, a substantial pixel size of 100µm, and an array size of 192×192 pixels. This detector supports exceptionally high frame rates of up to 30.000 fps in 8-bit mode, demonstrating exceptional performance for high-speed counting.

In conclusion, EM detector technology has rapidly evolved. CCD/CMOS detectors remain strong in high-resolution imaging. Still, hybrid pixel detectors like Medipix dominate 4D-STEM due to their fast frame rates, inherent ability to work at low dwell times, and precise event timing. MAPS sensors like Celeritas XS offer a promising balance of resolution and speed but require further optimization for lower-dose applications.

However, implementing effective strategies to reduce data volume directly at the detector during 4D-STEM acquisition and reduce frame rate speeds remains a crucial challenge. This situation requires longer acquisition times, potentially compromising the integrity of dose-sensitive samples and limiting the capabilities of multimodal workflows. Future research should explore techniques to address these bottlenecks, including data compression at the detector level and faster acquisition strategies. This path will unlock the full potential of 4D-STEM for high-fidelity, information-rich characterization, particularly in the context of multimodal analysis.

Table 2.3. *The state of the art in most relevant EMPAD sensors for EM.*

Detector/ Manufacturer	**Pixel size [µm×µm]**	**Array size**	**Detector type**	**Readout**	**Frame rate [fps]**	**Detection mode**
Medipix1/ CERN	170 × 170	64 × 64	Hybrid	Frame-based	135	Counting
Medipix2/ CERN	55 × 55	256 × 256	Hybrid	Frame-based	Serial: 111 fps Parallel: 3759 fps	Counting
Medipix3/ CERN	55 × 55	256 × 256	Hybrid	Frame-based	Parallel: 2036 fps	Counting
K2/ Gatan	5 × 5	3840 × 3712	MAPS	Frame-based	400 fps	Counting
K3/ Gatan	5 × 5	5760 × 4092	MAPS	Frame-based	1500 fps	Counting
Falcon 4/ Thermo Fisher	14 × 14	4096 × 4096	MAPS	Frame-based (EER)	250	Counting/ Survey
EMPAD/ Thermo Fisher	150 × 150	128 × 128	Hybrid	Frame-based	1100	Counting
Rio 16	9 × 9	4096 × 4096	Indirect (Scintillator)	Frame-based	20	Counting
Apollo/ Direct Electron	15 × 15	4096 × 4096	MAPS	Event-based[1]	60	Counting
Celeritas/ Direct Electron	15 × 15	1024 × 1024	MAPS	Frame-based	1960	Counting
ARINA/ Dectris	100 × 100	192 × 192	Hybrid	Frame-based	20000 (12 bit) 30000 (8 bits)	Counting

(1) Linearly dependent on exposure time (integration mode).

2.6. Neuromorphic solution

As detailed in previous sections, the challenges faced by conventional EMPADs necessitate a paradigm shift towards more efficient and information-centric data acquisition in electron microscopy. Adopting a neuromorphic approach inspired by the sophisticated design principles of biological nervous systems offers a promising path to overcome these limitations.

In this thesis, we investigate image sensors incorporating data streaming techniques inspired by point-to-point neuromorphic systems, such as AER communication protocols with asynchronous operation [5–7] or the and Integrate and Fire (I&F) neurons [2].

2.6.1 Integrate and Fire neurons

Integrate and Fire (I&F) neurons, a key element in analog neuromorphic systems, are designed to replicate the behavior of biological neurons. Unlike digital implementations, I&F neurons operate in the analog domain, using continuous signals for both input and output. This unique characteristic closely mimics biological neurons and provides inherent noise immunity and energy efficiency advantages, making I&F neurons a valuable asset in analog neuromorphic systems.

The operation of an I&F neuron involves the integration of weighted charge inputs triggered by presynaptic action potentials (spikes). These inputs, typically current pulses, mirror the synaptic connections from other neurons. The neuron accumulates these charges on a capacitor, emulating a biological neuron's membrane capacitance [89].

As the integrated voltage on the capacitor rises, it is continuously compared to a threshold voltage. When the integrated voltage surpasses this threshold, the neuron "fires," i.e., generates a short output pulse (spike) to signal its activation. Subsequently, the integrator (capacitor) is reset, and the process begins anew.

Figure 2.5 illustrates the circuit implementation of an I&F neuron, proposed by Carver Mead in [2]. It consists of a capacitor for integration, a high-gain amplifier or comparator to provide the threshold comparison and spiking mechanism, and a reset mechanism to discharge the capacitor after firing. This straightforward design has

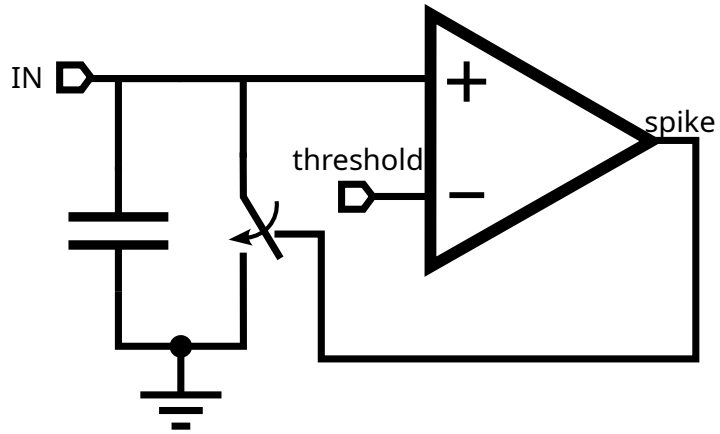

Figure 2.5: Basic schematic of an Integrate-and-Fire neuron.

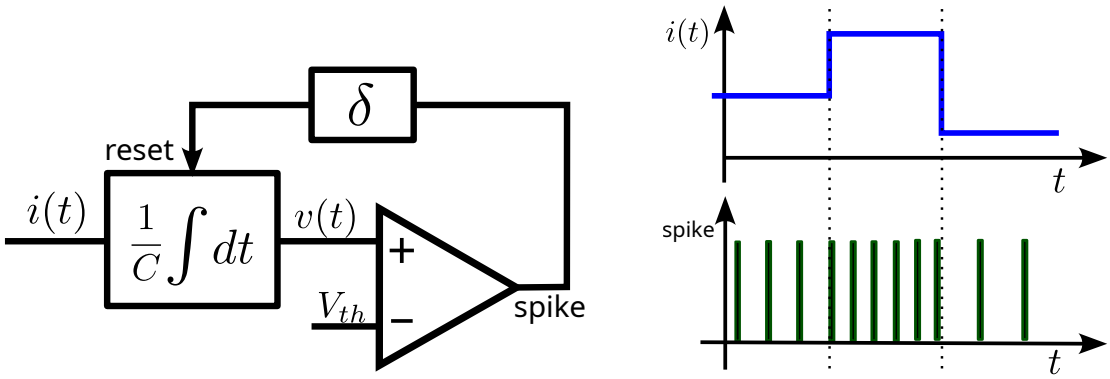

(a) (b)

Figure 2.6: (a) Block diagram of an I&F neuron using an electrical current over time as input. $i(t)$. (b) Spiking activity of the same I&F neuron as a $i(t)$ function.

become a foundational element in neuromorphic engineering, enabling the creation of large-scale networks of silicon neurons in various computational and sensory processing tasks.

Interestingly, the I&F neuron can be viewed as an analog-to-time converter. It transforms an analog input current or charge (the sum of weighted synaptic inputs) into an analog time interval (the time it takes for the integrated voltage to reach the threshold). Figure 2.6 illustrates a simplified diagram block that exemplifies a case where an I&F silicon neuron processes an input current. The first block weights and integrates its value, and then the resulting voltage is compared with a predefined threshold. Once it exceeds the threshold, a comparator is triggered, a pulse is generated, and the integrator is reset. The frequency of these output pulses, or the firing rate, is directly proportional to the magnitude of the input current. In this way, the I&F neuron encodes the intensity of the input signal as a frequency-modulated output. Simulation

waveforms are provided in the Annex A.3

Neuromorphic models encompass diverse neuron implementations, spanning from biologically plausible to computationally driven designs. I&F neurons, while relatively simple and less biologically realistic compared to other models, offer significant computational efficiency, making them a popular choice for large-scale neuromorphic systems [90].

2.6.2 The Address-Event Representation (AER) Protocol

The Address-Event Representation (AER) protocol, pioneered by Mahowald and Sivilotti [3,91], revolutionizes communication within neuromorphic systems by emulating the asynchronous nature of biological neural networks. AER is an event-driven approach that transmits only the timing and location of individual electron events rather than the entire image frame. This approach significantly reduces data volume and processing requirements compared to traditional frame-based methods. Integrating AER principles can lead to even more efficient data handling and potentially alleviate the computational load on the sensor. This efficiency would prove particularly advantageous in high-throughput 4D-STEM workflows.

AER has become a key component in neuromorphic engineering, especially for replicating the three-dimensional structure of the nervous system. This emulation necessitates adhering to fundamental principles: implementing event-driven communication, prioritizing access to the communication channel for the most active cells, and exploiting sparse activity to enhance speed. Unlike traditional digital circuits relying on external clock synchronization, AER employs a time-division multiplexing (TDM) scheme, where events are encoded with their location and timestamps. This approach overcomes the scalability challenges of point-to-point connections between numerous neurons, significantly reducing the required wires.

AER-based sensors and processors communicate event-driven, departing from the conventional fixed-interval readout of image sensors. Each pixel independently generates an event only upon detecting a significant change, such as a variation in light intensity (or another relevant parameter). This event, carrying the pixel's address and timestamp, is transmitted asynchronously through a shared bus. The AER control circuitry acts as an arbiter, managing the event transmission according to the application. This asynchronous, event-driven communication minimizes data redundancy and

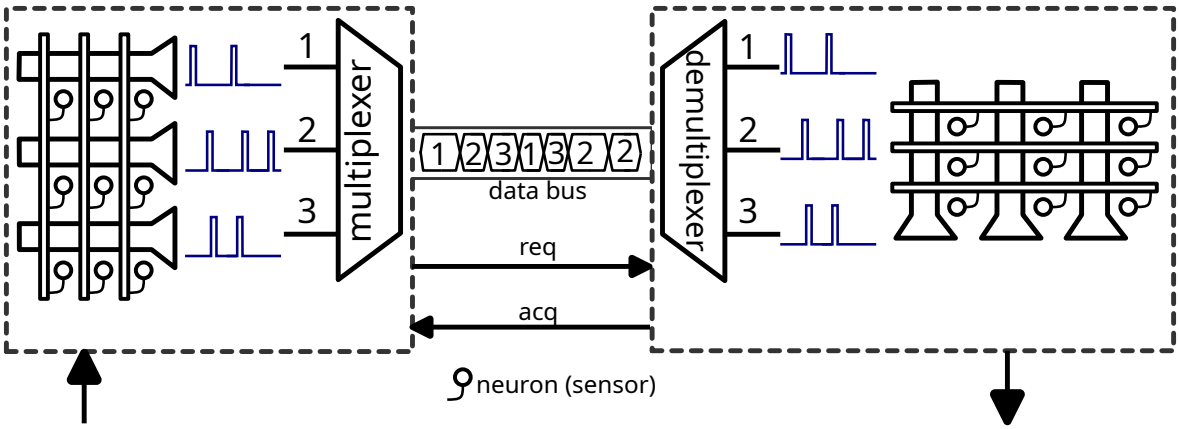

Figure 2.7: Basic implementation of AER protocol

enables high-bandwidth communication and real-time processing within neuromorphic systems, mirroring the efficiency of biological neural communication.

Figure 2.7 depicts the AER protocol involving a transmitting side (e.g., an event-based sensor) and a receiving side (e.g., a processor). Upon detecting a significant change, each transmitting element generates an event encoded with its address and a timestamp. The AER control circuitry acts as an arbiter, managing the event transmission according to the application. The multiplexer sequentially encodes these events based on their address (denoted by numbers 1, 2, 3) and transmits them over the shared data bus. The data bus conveys a sequence of events with corresponding addresses (1, 2, 3, 1, 3, 2, 2), indicating the temporal order of events generated by the source units.

The receiving side employs a demultiplexer to decode the address and route the event to its intended destination. Crucially, a handshaking mechanism using *req* (Request) and *ack* (Acknowledgement) signals, as illustrated in the timing diagram in Figure 2.8, ensures orderly communication. When a transmitting element wishes to send data, it asserts the *req* signal. The receiver, if available, responds with an *ack* signal after a short delay (t_1 in Figure 2.8), granting bus access and prompting the transmitter to put the data on the bus. This exchange ensures data integrity and prevents conflicts, particularly when multiple elements request transmission simultaneously. Once the data has been read (t_2-t_3 and t_5-t_6 in Figure 2.8), the *ack* signal is de-asserted, and the *req* signal is subsequently de-asserted. The cycle then repeats for subsequent events.

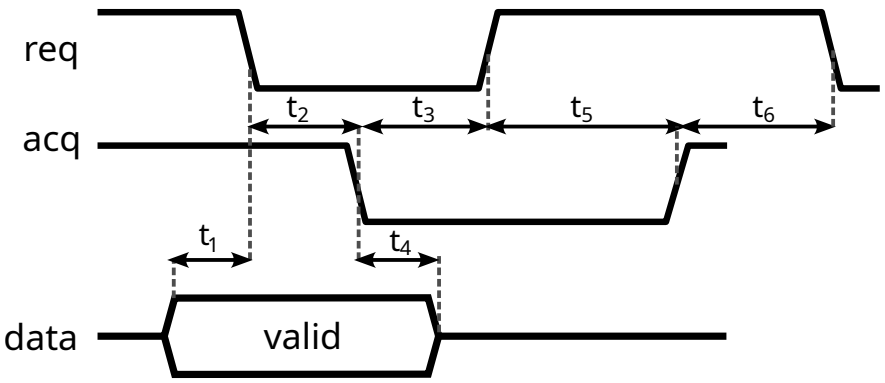

Figure 2.8: Timing diagram of a typical AER handshaking.

2.6.3 Collision handling and arbitration in AER

In AER protocol, efficient handling of multiple simultaneous events, or "collisions," is crucial to ensure data integrity and maximize throughput. As AER sensors operate asynchronously, multiple pixels may generate events concurrently, creating a potential conflict for access to the shared communication bus. To address this issue, AER systems use arbitration mechanisms. There are three different bus arbitration approaches in AER: full arbitration [92, 93], discarding [94], and aging vs. loss trade-off [95]. It is beyond the scope of this work to delve into the details of each arbitration mode so that we will focus on one of the most commonly used methods: full arbitration.

Figure 2.9 (a) illustrates that the binary tree arbiter employs a hierarchical structure based on a series of two-input arbiter circuits. In this structure, pairs of pixels (or event generators) share a simple arbitration circuit, which essentially functions as an RS flip-flop constructed from two cross-coupled NAND gates. Without requests, the flip-flop rests in an unstable state, with both outputs set high. When multiple requests arrive simultaneously, the flip-flop's state is determined by the first received request, whether *req0* or *req1*. The winning request moves up the tree to the next level, while the losing request is held back. This process repeats at each tree level until a single request reaches the top and is granted access to the bus.

The advantage of the binary tree arbiter lies in its logarithmic scaling. For N input requests, the arbitration delay is proportional to $\log(N)$, ensuring efficient conflict resolution even in large-scale systems. Figure 2.9 (b) illustrates how an 8-input arbiter can be constructed using seven instances of the 2-input arbiter.

Once a request has been granted, the AER system initiates a four-phase hand-

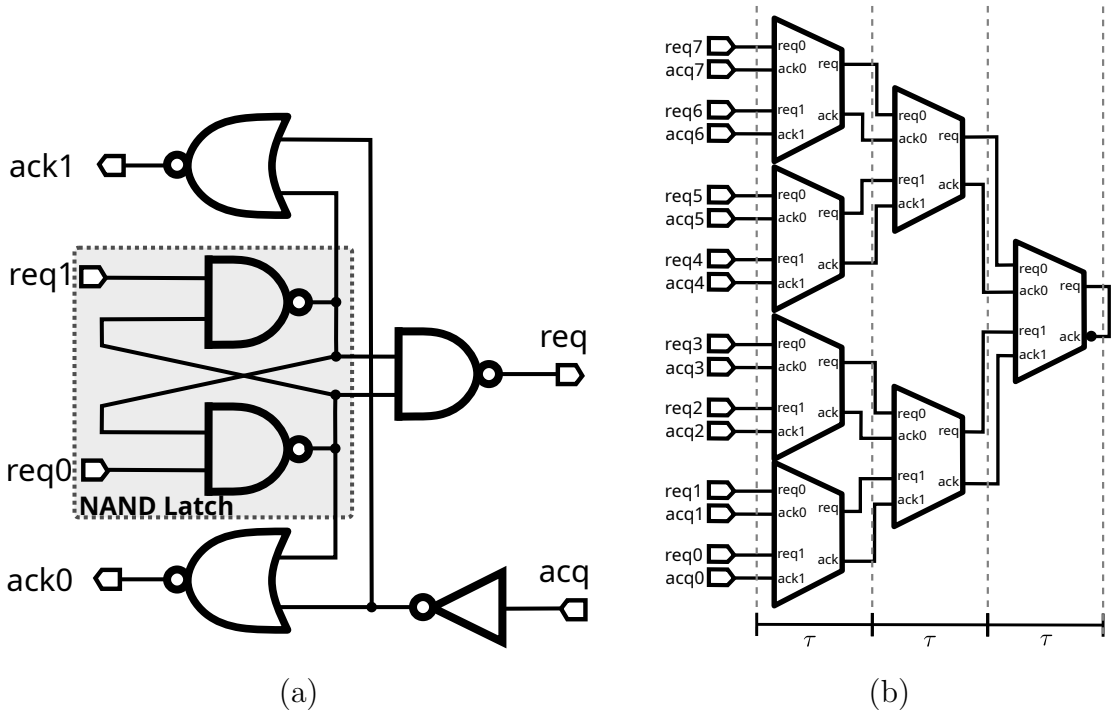

(a) (b)

Figure 2.9: (a) 2-input Greedy Arbiter for AER. (b) 8-input Binary Tree Arbiter for AER.

shake protocol to facilitate data transmission:

1. **Request:** The winning pixel asserts its REQ signal, indicating its intent to transmit data.

2. **Acknowledge:** The receiver (e.g., processor) acknowledges the request by asserting the ACK signal, granting the pixel access to the bus.

3. **Data Transmission:** The pixel places its event data (address and timestamp) onto the bus.

4. **Request Withdrawal:** After the receiver successfully reads the data, the pixel de-asserts its REQ signal. The receiver then de-asserts its ACK signal, marking the completion of the transmission cycle.

While the binary tree arbiter is efficient, exhaustive event detection mechanisms might lead to a single pixel requesting bus access multiple times [96]. In such cases, fairness mechanisms or modifications to the arbitration scheme may be necessary to ensure that all pixels have equal opportunities to transmit their events. Resolving conflicts efficiently and ensuring fair access to the communication bus enables the high-bandwidth, real-time processing capabilities essential for neuromorphic applications.

2.6.4 Refractory Period in Neuron Model

While the basic integrate-and-fire (I&F) neuron model offers computational efficiency, incorporating additional biological properties can enhance its realism, although at the cost of increased complexity [90]. One such property is the refractory period, a brief interval following an action potential during which a neuron is less responsive to stimuli and cannot generate another spike.

In AER-based neuromorphic systems, the refractory period can be implemented as a period during which a pixel (neuron) is prevented from requesting data transfer after successfully transmitting an event [3]. This mechanism is crucial for efficient arbitration among simultaneous events. By imposing a refractory period, the arbiter can prioritize events from different neurons, ensuring fair access to the communication channel.

The duration of the refractory period is a crucial design parameter. A prolonged refractory period allows for more effective arbitration, mainly when multiple neurons are simultaneously active. However, it also limits the neuron's maximum firing rate. The refractory period should ideally be set to allow for the transmission of all coincident events in rapid succession before a new event can be generated, achieving a balance between event detection and data handling efficiency. This ensures that all events are captured and transmitted effectively, preventing individual neurons from monopolizing the communication channel. In commercial AER cameras, such as the Prophesee Gen4 EVKv2, although the manufacturer does not publicly disclose the specific refractory period values, experimental testing has shown that they range from 6.8 µs to 6.3 ms [97].

2.6.5 Summary

Neuromorphic engineering represents a revolutionary approach to EMPAD design. It utilizes event-driven sensing and asynchronous communication to overcome the limitations of traditional detectors. In this context, the silicon retina, a neuromorphic vision sensor, serves as the foundation for the EMPAD, with individual pixels acting as the "neurons." These pixels respond to electron impacts on the detector substrate, generating events that carry both spatial and temporal information.

In this paradigm, the pixels within the EMPAD act as individual neurons, re-

sponding to incident electrons as their stimuli. When an electron strikes a pixel, it triggers an event equivalent to a neuron firing. Encoded with the pixel's address and a timestamp, this event is transmitted asynchronously through the AER protocol. By transferring only these significant events, AER dramatically reduces data redundancy and bandwidth requirements, allowing for more efficient utilization of the communication channel.

The following chapter will build upon the theoretical foundation laid in this chapter by detailing the practical implementation of neuromorphic principles for EMPADs using microelectronics. This will include thoroughly examining the detector architecture, pixel-level circuit designs, and the circuit integration of the AER protocol and I&F circuits. Additionally, we will explore the design and structural requirements needed to implement these detectors and the signal processing methods that enhance their performance in EM applications. Through this exploration, we aim to demonstrate the feasibility and efficacy of neuromorphic EMPADs as a viable solution to the challenges faced by traditional detectors.

Chapter 3

Implementation of a Neuromorphic EMPAD with AER

Two primary approaches in pursuing radiation-hard image sensors have emerged: back-thinning and flip-chip fabrication [98]. The latter, exemplified by the Medipix family of sensors, excels in applications like 4D-STEM due to its near 100% fill factor and may achieve high sensitivity through an application-specific detector.

Although flip-chip fabrication of EMPADs offers benefits, it's still expensive because of the significant post-processing steps involved. Furthermore, it restricts the number of pixels that can be incorporated [99]. The maximum size for small-pitch bump bonding is typically around 10 to 20 μm [100]. Consequently, with its sequential pixel scanning, traditional sequential readout hinders high-speed operation and scalability. Although advanced readout circuitry has been explored [101], these implementations often rely on digital counters, limiting the charge integration time and increasing pixel pitch due to the additional circuitry required.

This chapter focuses on practically implementing an alternative approach to address these limitations: a neuromorphic EMPAD leveraging the Address-Event Representation (AER) protocol. AER enables high-speed, asynchronous communication with minimal impact on pixel fill factor, as the in-pixel logic for AER compatibility is relatively straightforward [5,6]. This chapter presents a novel design for a direct charge sensing asynchronous pixel compatible with AER, tailored explicitly for EM applications. The design aims to achieve high sensitivity, low latency, and wide dynamic range while maintaining cost-effectiveness and scalability.

3.1. Neuromorphic EMPAD: Concept and Design

Building upon the theoretical foundation in Chapter 2, which explored the challenges faced by conventional EMPADs and the potential of neuromorphic solutions, this chapter transitions from theory to practice. We begin by outlining the general concept and design principles of a neuromorphic EMPAD, emphasizing the event-driven nature of data acquisition and the asynchronous communication facilitated by AER.

Subsequently, we will present a specific implementation detailing the architecture and organization of the pixel matrix and the design of individual pixels. We will also discuss the layout and structural considerations for the pixel arrays, focusing on optimizing the detector for efficient electron detection and signal transmission.

The latter part of the chapter will be dedicated to a comprehensive analysis of the implemented EMPAD. We will evaluate its performance at both the matrix and pixel levels, quantifying its data reduction capabilities, temporal resolution, sensitivity, and other relevant metrics. A comparative analysis with traditional EMPADs will further highlight the advantages and potential of the neuromorphic approach in electron microscopy applications.

3.1.1 Matrix Architecture and Pixel Organization

An exemplary AER-based pixelated matrix capable of functioning as either an EMPAD or an image sensor to form a "silicon retina" is depicted in Figure 3.1. This matrix comprises a 128×128 pixel array, whose two-dimensional nature compels a specialized data transmission protocol. A set of digital decoders positioned at the edges of the array decodes address events into specific pixel locations. The sensor comprises the pixel matrix, a control block for sensor operation and readout modes, and the AER arbitration system.

Each pixel functions as an independent, asynchronous unit capable of generating events upon detecting a significant change (e.g., electron impact or variation in light intensity). Each pixel is subject to a refractory period that restricts its event generation frequency, helping to mitigate bus congestion. These events, encoded with their address and timestamp, are transmitted off-chip via a shared readout channel managed by an arbitration circuit.

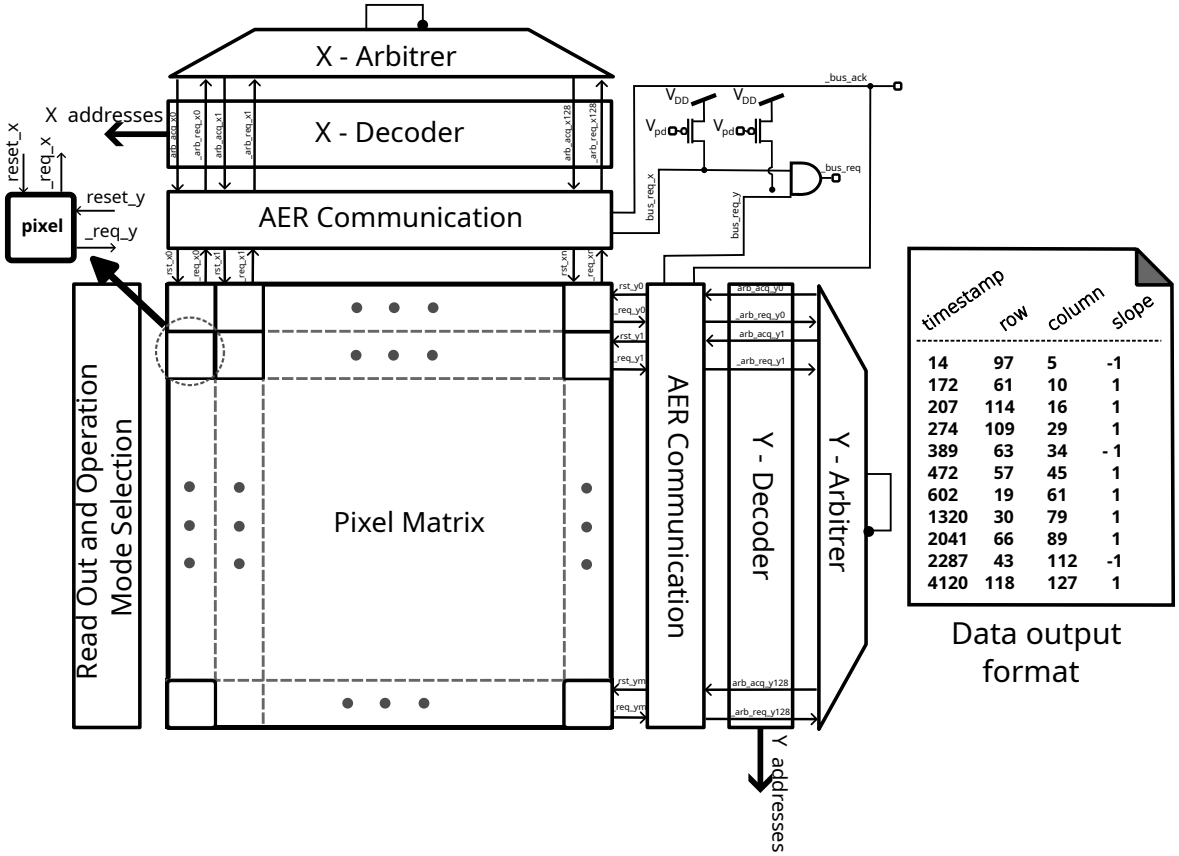

Figure 3.1: Block diagram of an AER-based matrix architecture for EMPAD and image sensor applications. Data Output Format includes a timestamp, pixel location, and slope parameters. Adapted from [102].

The AER arbitration system plays a crucial role in managing event transmission. The system resolves potential collisions between simultaneous requests for access to rows and columns at each pixel (*_req_x* and *_req_y* in Figure 3.1) through a hierarchical arbitration mechanism. Pixels initially request access at the row (or column) level using wired-NOR gates implemented with a single NMOS transistor per pixel. The winning row (or column) then requests access at the column (or row) level, ensuring that only one pixel transmits data at a time. This sequential arbitration scheme prevents generating "ghost events," which could occur if arbitration in both dimensions proceeded independently. While crucial for preventing bus congestion, this refractory period can also impact the detector's ability to handle high radiation flux rates (or high electron flux rates in the case of direct EMPADs). For an EMPAD, if multiple electrons strike a pixel within its refractory period, only the first electron event will be recorded, leading to potential coincidence loss and undercounting of electrons. Therefore, carefully considering the refractory period duration is essential to balance efficient bus utilization with capturing rapid events and minimizing coincidence loss.

The readout and operation mode selection block manages the sensor's functionality, including configuring the readout mode and overall operational parameters. The data output format specifies the structure of the transmitted event data, which includes a timestamp, row, and column indices, as well as a slope parameter that may be relevant for specific applications. The *arb_req* and *arb_ack* signals support the critical request-acknowledge handshake mechanism, ensuring synchronized communication between the transmitting pixels and the receiving end.

Sensors implemented with AER-based matrices offer numerous advantages, including reduced data flow, power consumption, and latency due to their event-driven nature. However, scaling the number of pixels poses challenges with traditional word-serial AER implementations. As the number of pixels increases and the pixel pitch decreases, issues such as inter-pixel capacitance coupling, stray capacitance from connections to readout electronics, the complexity of data management and readout, and challenges in maintaining channel matching become more prominent [103]. These factors can lead to higher power consumption, necessitate faster readout schemes to maintain frame rate, and degrade communication line impedance, impacting data throughput, latency, and signal integrity. Addressing these limitations involves implementing design guidelines for asynchronous communication circuitry, as outlined in [104].

3.1.2 Pixel Design Principles

The fundamental building block of the AER-based EMPAD is the individual pixel, designed to detect electron impacts and generate asynchronous events for efficient data transmission. Figure 3.2 shows a Dynamic Vision Sensor (DVS) general pixel circuit schematic. It comprises five key components: a detector, a Charge-Sensitive Amplifier (CSA), a differential amplifier, comparators with adjustable thresholds, and an in-pixel logic [105]. This design is also based on a DVS pixel for image sensors, as proposed in [106, 107].

The core component of the sensing is the detector, which may consist of a photodiode for sensing light or a specialized electron detector in the case of electron microscopy (EM). The detector converts the incident electron's energy into a charge signal. This charge is then amplified and converted into a voltage by the Charge Sensitive Amplifier (CSA), typically based on the Krummenacher architecture [103]. This kind of CSA design incorporates a feedback loop and a leakage compensation mechanism to ensure

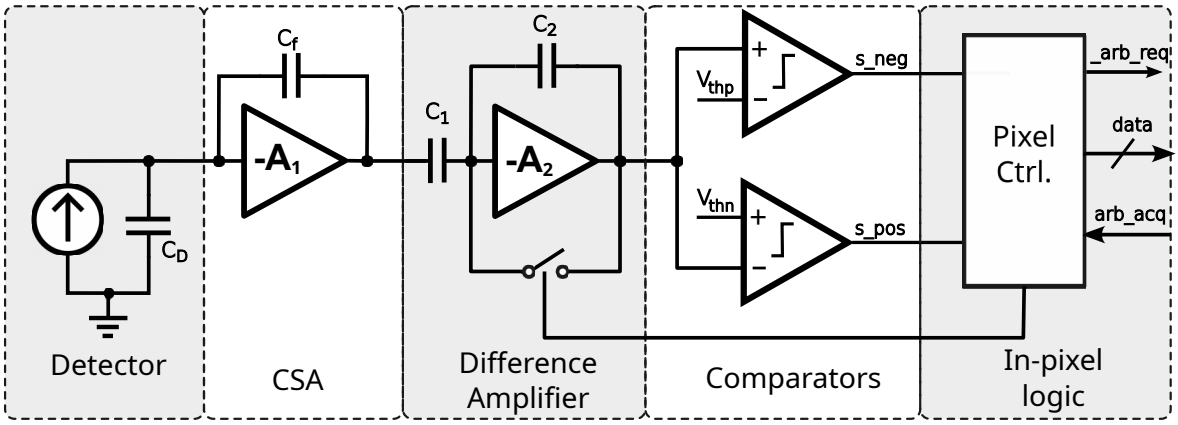

Figure 3.2: Proposed general pixel circuit schematic for an AER-based DVS pixel for charge detection in semiconductor detector applications.

accurate charge-to-voltage conversion and mitigate the effects of leakage current, which can degrade detector performance [108].

A differencing amplifier further processes the amplified voltage signal, extracting the dynamic component of the CSA's output. This step is crucial as it removes any DC offset from the CSA or detector by balancing the output to a reset level after generating an event. The gain of this change amplification stage is determined by the well-matched capacitor ratio C_1/C_2, ensuring a precise gain that reduces the impact of inevitable comparator mismatches [106]. The amplified differential signal is then fed into two comparators with adjustable thresholds (V_{thp}, V_{thn}). These comparators detect when the signal crosses the predefined thresholds, generating digital pulses that signify the occurrence of an electron impact event or a change in the pixel state. The in-pixel logic subsequently encodes these events into the AER format, including the pixel's address and a timestamp. This encoded information is transmitted through the *arb_req* and *arb_ack* signals for arbitration and communication with the AER bus.

The pixel's logic can be modified based on the specific application. For instance, the event generation can be triggered by exceeding thresholds and a counter reaching a particular value or upon satisfying other predefined conditions. This adaptability allows the pixel to be tailored for different EM modalities and experimental requirements. In its simplest form, the pixel generates an event whenever a positive or negative threshold crossing is detected, indicating the arrival of an electron with sufficient energy.

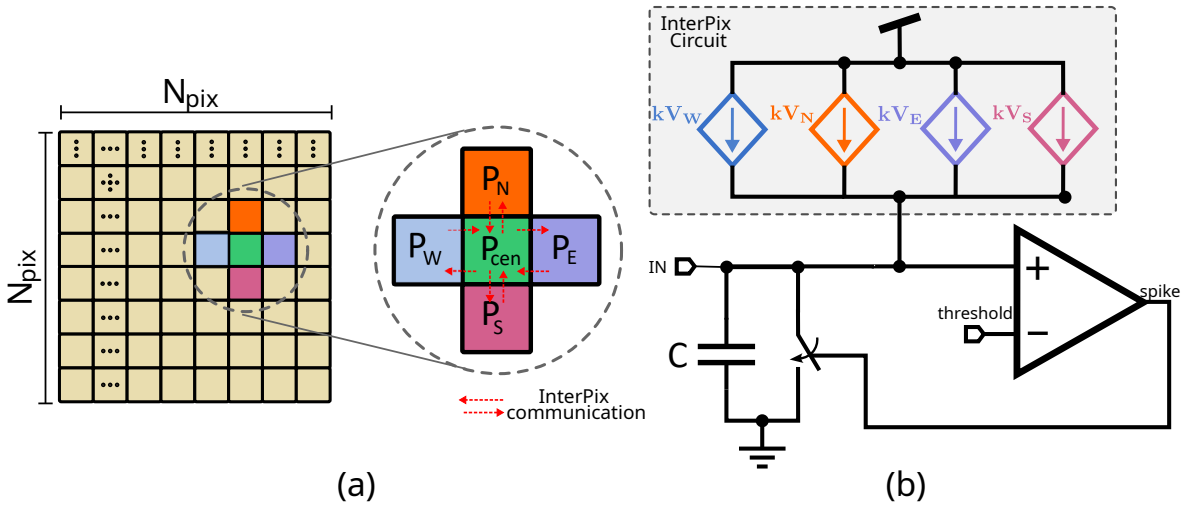

Figure 3.3: (a) Pixel array detector and neighbor pixels. (b) Neuromorphic Pixel with Inter-Pixel Communication and I&F Circuit with Charge Sharing Correction

3.1.3 Charge sharing correction and spatial resolution

As discussed in Chapter 2, charge sharing is a prevalent challenge in EMPADs, particularly when the charge cloud generated in the sensor by an incident electron becomes comparable to the pixel size or inter-pixel spacing. This phenomenon leads to charge being induced and collected across multiple pixels, distorting the energy spectrum measured by individual pixels and compromising spatial and energy resolution [109]. Charge sharing is especially problematic in single-particle counting systems, where the goal is to detect and quantify individual electron impacts accurately [110].

Correcting charge-sharing and loss is essential to maximize pixelated detectors' counting and spectroscopic performance. One approach to mitigating charge-sharing is Charge-Sharing Discrimination (CSD), where multi-pixel events are discarded [111]. However, this method sacrifices detection efficiency.

Neuromorphic approaches offer an alternative charge-sharing solution by incorporating inter-pixel communication inspired by biological neural networks. In this approach, pixels exchange information about their detected signals with neighboring pixels, allowing for a more accurate estimation of the spatial distribution of the charge cloud. This strategy can lead to improved spatial resolution and reduced charge-sharing effects. For example, a bio-inspired vision sensor utilizes inter-pixel communication to compute spatial contrast [112]. In this design, pixels send pulses to their neighbors with a frequency proportional to the received light intensity. A competition mechanism then enables pixels with higher illumination relative to their neighbors to generate events,

effectively enhancing spatial contrast and reducing the impact of charge-sharing.

Other method is depicted in Figure 3.3(a) and illustrates a central pixel (P_{cen}) surrounded by its adjacent neighbors (P_w, P_n, P_e, P_s). When a particle strikes a pixel, a mirrored version of the charge deposited in adjacent pixels is added to the charge in the central pixel. This approach, known as Charge Summing Mode (CSM), aims to recover the total charge of the event and improve energy resolution. Figure 3.3(b) illustrates a model of an Integrate-an-Fire (I&F) neuron circuit incorporating CSM charge-sharing correction. This process is achieved by adding mirrored signals of the charge deposited in four adjacent pixels multiplied by an adjustable parameter k to the charge in the central pixel. Typically, the value of k is set to one, but it can be adjusted to optimize the charge-sharing correction based on the specific detector characteristics and imaging conditions. The total accumulated charge is then integrated over time, and if it exceeds a predefined threshold, the neuron fires an event. This approach aims to reduce charge-sharing effects by reconstructing the total charge and attributing it to the central pixel. The commercial Medipix3 family of EMPADs employs a CSM circuit with inter-pixel communication to reconstruct the total charge within overlapping 2×2 pixel clusters [113]. An arbitration circuit then assigns the event to the pixel with the highest charge deposition and the complete reconstructed charge is attributed to the winning pixel within a 3×3 neighborhood.

3.2. Proposed Neuromorphic EMPAD Design

3.2.1 Specific Pixel Circuit Implementation

In response to the limitations of current EMPAD technologies, this study introduces an innovative CMOS asynchronous pixel architecture engineered explicitly for the direct detection of ionizing (beta) radiation[1]. The pixel design, compatible with the AER protocol, presents a promising avenue for its integration into radhard PADs for electron microscopy applications (direct EMPADs).

The proposed pixel circuit, shown in Figure 3.4, has been designed to discern both fluence (particle count) and charge polarity (positive or negative) of charged

[1]Ionizing radiation refers to any form of radiation that has enough energy to remove tightly bound electrons from atoms or molecules, thereby creating ions. This process is called ionization. Ionizing radiation is a form of energy released by atoms in the form of electromagnetic waves (such as X-rays or gamma rays) or particles (such as alpha particles, beta particles, or neutrons).

particles such as electrons or protons. The core of the pixel is a floating metal layer that serves as both the radiation-absorbing element and an electrical shield for the underlying readout circuitry. This layer is connected to the input of a charge-sensitive amplifier (CSA) through a coupling capacitor (C_1). The floating electrode accumulates a net electric charge upon irradiation, which amplifies the CSA. This net charge results from a balance between absorbed and re-emitted charged particles [114]. The amplifier, feedback capacitor (C_2), and C_1 form an inverting amplifier configuration with an AC gain of approximately $-C_1/C_2$ for voltages [103, 115], or equivalently, as a charge-sensitive amplifier (CSA) with a transfer function of:

$$\Delta V_{amp} = -\frac{\Delta Q_A}{C_2} \tag{3.1}$$

where ΔQ_A represents the net absorbed charge on the top plate of C_1.

To achieve a precise gain in this differencing circuit and reduce the mismatch[2] effects, capacitors C_1 and C_2 are arranged in a common-centroid layout [3] to ensure well-matched electrical characteristics [106]. This condition is achieved by selecting C_1 as mC and C_2 as nC, where m and n are integers and C is a designated unit capacitance. Minimizing C_2 maximizes the charge-to-voltage conversion, which could negatively impact pixel pitch and fluence sensitivity. Therefore, choosing $m > n$ is often advisable to maintain an appropriate pixel pitch while achieving the desired charge transfer efficiency.

Figure 3.5 illustrates the circuit's operation. Initially, the *reset* signal is asserted, activating the switch with the phase ϕ and initializing both the electrode voltage V_{top} and the amplifier output voltage V_{amp} to a reference voltage V_{REF}. Upon electron irradiation, the accumulated charge on C_1 causes the voltage V_{top} to increase or decrease, depending on the net absorbed charge. The amplifier output voltage (V_{amp}) then tracks the temporal variation of charge on the electrode with a proportionality constant of $-1/C_2$.

The proposed pixel circuit employs a differential architecture to detect and encode electron impacts as asynchronous events. As shown in Figure 3.4, two comparators

[2]Mismatch refers to the slight variations in electrical characteristics between nominally identical components within an integrated circuit.

[3]A common-centroid layout is used in integrated circuit design to minimize the mismatch between capacitors or other matched devices. It involves arranging the devices symmetrically around a central point, ensuring they experience similar process variations and environmental conditions.

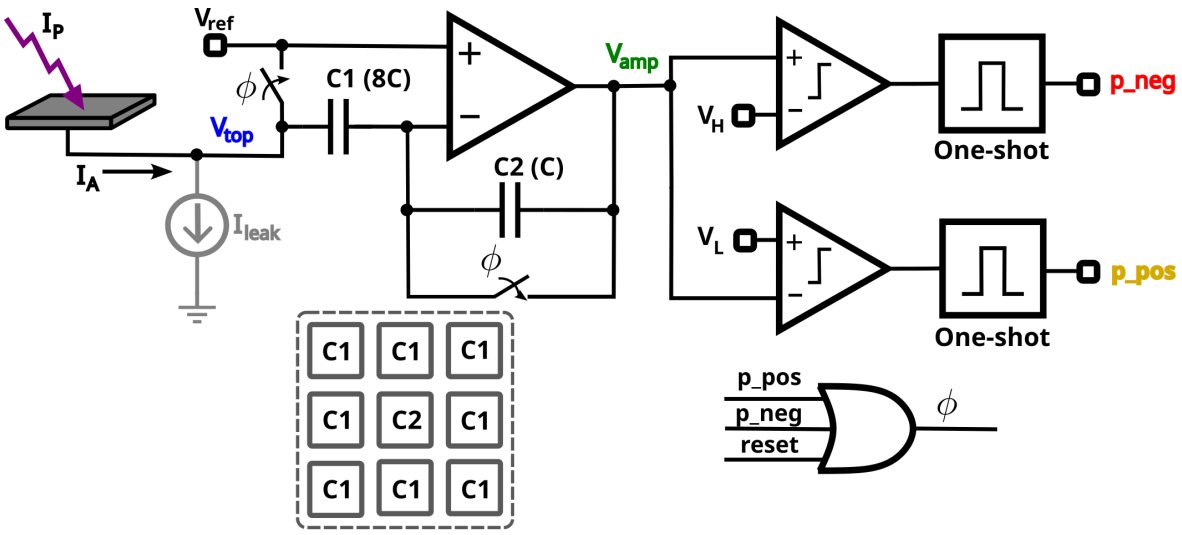

Figure 3.4: Schematic of the proposed sensor using the floating metal plate for charge sensing.

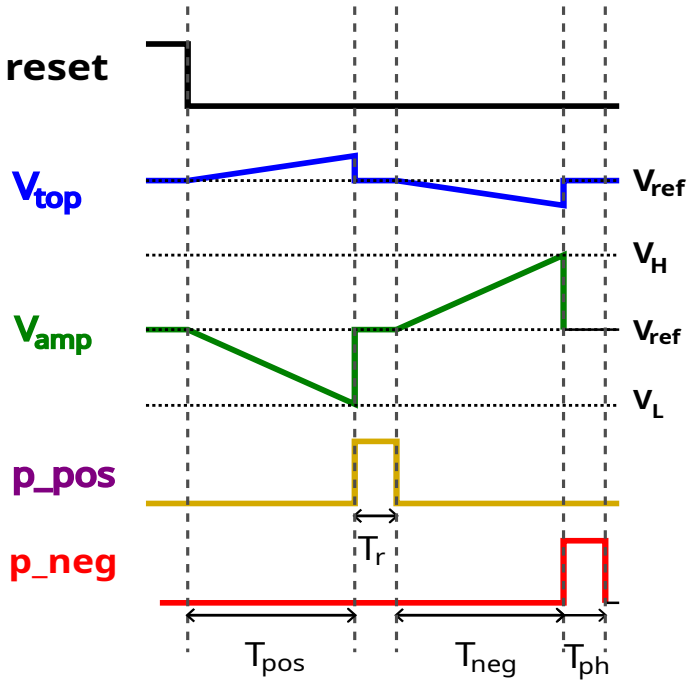

Figure 3.5: Waveforms indicating the behavior of the circuit of figure 3.4 for positive/negative charge detection

with adjustable threshold voltages (V_H and V_L) monitor the output voltage (V_{amp}) of the CSA. The detection limits are defined by the relationship $V_H > V_{REF} > V_L$, where V_{REF} is a DC bias voltage. Adjusting these thresholds can tailor the pixel's sensitivity to specific electron fluences. When a sufficient charge (Q_A) is deposited on the floating electrode over a period (T_{Q_A}), either the upper or lower comparator is triggered, generating a pulse (p_{neg} or p_{pos}) at the output of their respective one-shot

circuits. These pulses serve as the event signals, indicating the detection of an electron impact.

The circuit is reset after each event generation to ensure proper signal processing and prevent glitches. The NOR gate, activated by either comparator pulse, asserts its output (ϕ), resetting both the electrode voltage (V_{top}) and the amplifier output voltage (V_{amp}) back to the reference voltage (V_{REF}). This reset state is maintained for a duration (T_r) determined by the one-shot circuit, allowing the circuit to stabilize before detecting the next event.

The pixel's design is inherently compatible with AER communication within a pixel array. The delay elements in the single-pixel circuit can be replaced with transistors that activate row and column requests through a shared bus, following the AER protocol outlined in [7, 116].

The duration of the positive or negative pulses (T_{pos} or T_{neg}) is inversely proportional to the rate of change of the deposited charge on the electrode. Higher rates of charge deposition result in shorter pulse durations, leading to a higher pulse frequency ($f_{p,n}$), which can be expressed as:

$$f_{p,n} = \frac{1}{T_{Q_A} + T_r + T_d} \approx \frac{1}{T_{Q_A} + T_r} \tag{3.2}$$

where T_{Q_A} is the time elapsed to deposit a charge $Q_A = \Delta V_{p,n} C_2$, with $\Delta V_{p,n} = V_{H,L} - V_{REF}$; T_r is the retention time of the one-shot circuit; and T_d is the comparator's delay. For values commonly used in this work $T_r = 1\ \mu s$, and $T_{Q_A} > 5\ \mu s$, T_d can be neglected.

This frequency-encoded representation of the charge deposition rate enables efficient event information transmission through the AER protocol, minimizing data redundancy and facilitating real-time analysis in electron microscopy applications.

On the other hand, T_{Q_A} is related to the total absorbed current for the electrode I_A and the input leakage current, I_{leak}, which models the charge loss on the top MiM capacitor plate as:

$$T_{Q_A} = \frac{\Delta V_{p,n} \cdot C_2}{I_A - I_{leak}} \tag{3.3}$$

By substituting Equation (3.3) into Equation (3.2), we can define the sensitivity or gain ($K_{p,n}$) of the sensor for both positive and negative charges as the ratio of the

pulse frequency ($f_{p,n}$) to the absorbed current (I_A). This relationship is expressed as:

$$K_{p,n} = \frac{f_{p,n}}{I_A} = \frac{\left(1 - \frac{I_{leak}}{I_A}\right)}{\Delta V_{p,n} \cdot C_2 + T_r \cdot (I_A - I_{leak})} \tag{3.4}$$

By carefully adjusting these parameters, the sensitivity or gain of the pixel circuit can be tuned to match the specific requirements of the electron microscopy application.

Upon visual inspection of the curve of sensitivity in Figure 3.6 (a), $K_{p,n}$ is a nonlinear function of I_A with three distinct regions given by the following expressions:

$$K_{p,n} = \begin{cases} -\dfrac{I_{leak}}{\Delta V_{p,n} \cdot C_2 \cdot I_A} & I_A \ll I_{leak} \\ \dfrac{1}{\Delta V_{p,n} \cdot C_2} & I_{leak} < I_A < \dfrac{\Delta V_{p,n} \cdot C_2}{T_r} \\ \dfrac{1}{T_r \cdot I_A} & I_A \gg \dfrac{\Delta V_{p,n} \cdot C_2}{T_r} \end{cases} \tag{3.5}$$

The pixel circuit demonstrates a high degree of linearity, exhibiting a constant sensitivity of $1/(\Delta V_{p,n} \cdot C_2)$ over a wide range of absorbed currents (I_A). This linear range is bounded by a lower limit determined by the leakage current (I_{leak}) and an upper limit defined by the maximum non-saturating current, $I_{max} = (\Delta V_{p,n} \cdot C_2)/T_r$, where $\Delta V_{p,n}$ is the threshold voltage difference, C_2 is the feedback capacitance, and T_r is the reset time.

Consequently, within this linear operating range, we can define the sensor's dynamic range (DR) as the ratio between the maximum and minimum detectable currents, considering the noise contributions. Hence, the DR can be expressed as:

$$\text{DR} = 20 \cdot \log_{10}\left(\frac{I_{max}}{I_{min}}\right) = 20 \cdot \log_{10}\left(\frac{\Delta V_{p,n} \cdot C_2}{T_r\sqrt{I_{leak}^2 + \sigma_{I_n}^2}}\right) \tag{3.6}$$

where I_{min}, the minimum detectable current, is a function of both the leakage current I_{leak} and the input-referred noise σ_{I_n} under dark conditions, as defined in [117]. Notably, the dynamic range (DR) of the sensor can be adjusted externally through the configuration of the high and low threshold voltages (V_H) and (V_L), respectively.

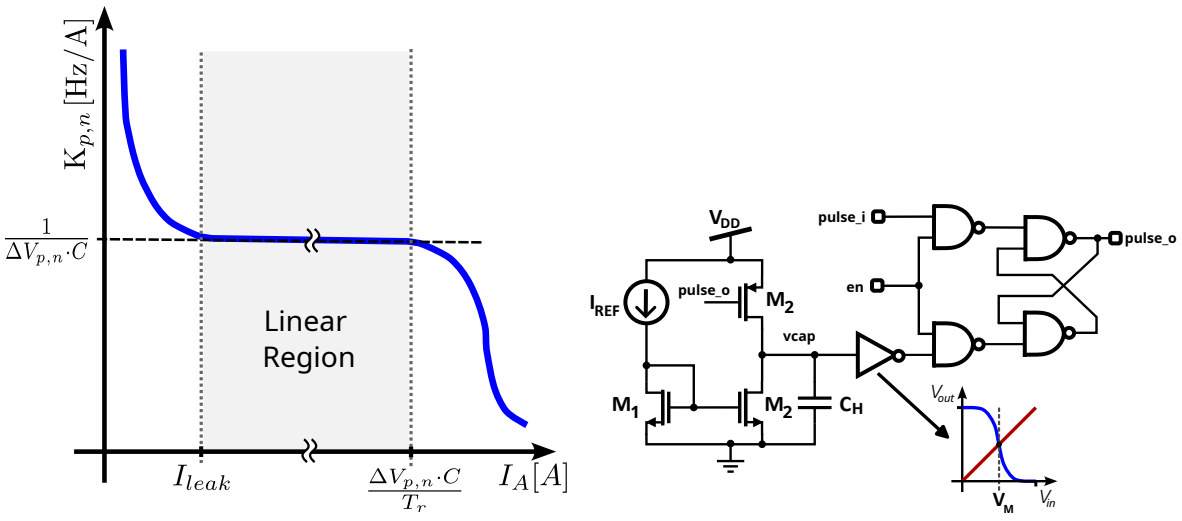

(a) (b)

Figure 3.6: (a) Sensor's sensitivity ($K_{p,n}$) versus absorbed current (I_A) showcasting the linear region of operation. (b) A one-shot circuit is created by integrating an external current I_{REF}, a latch, and a MOS capacitor C_H.

The retention time (T_r) necessary for the reset operation was generated using a one-shot circuit, as illustrated in Figure 3.6 (b). This time is related to the refractory period mentioned in Section 2.6.4. This circuit, implemented with logic gates and a capacitor (C_H), produces a pulse of the required duration, calculated as:

$$T_r = \frac{V_M \cdot C_H}{I_{REF}} \simeq \frac{V_{DD} \cdot C_H}{2I_{REF}} \tag{3.7}$$

where I_{REF} is an externally programmable reference current and V_M is the trip point of the inverter cell.

The lower limit of the retention time (T_r) is primarily dictated by the charging/discharging time of capacitors C_1 and C_2 through the transmission gates (TGs). Corner simulations indicate a minimum value of 1 µs for (T_r) to ensure reliable operation. Attempting to reduce T_r further by using minimum-length MOS devices in the TGs is impractical due to the trade-off between leakage current in the off-state and the circuit's settling time [118].

3.2.2 Pixel Layout and Structural Considerations

The spatial resolution of an EMPAD is fundamentally influenced by the layout and structure of its pixels. Pixel size, shape, and material composition are critical design

parameters that must be carefully balanced to optimize detector performance. Smaller pixels generally offer higher spatial resolution, but they can be more susceptible to the spread of charge from a single electron impact across multiple pixels, a phenomenon known as charge-sharing. This charge diffusion can lead to a degradation of image quality and a reduction in the detector's ability to accurately localize the point of electron impact. Conversely, larger pixels may mitigate charge-sharing but at the expense of spatial resolution. Additionally, the pixel shape plays a role in charge collection efficiency and can be tailored to minimize cross-talk between adjacent pixels, further enhancing the detector's performance.

Material selection is another crucial aspect. The choice of detector material impacts both the radiation hardness and the charge collection efficiency of the pixel. Radiation-hard materials are essential to mitigate the detrimental effects of prolonged exposure to the electron beam, such as creating hot pixels and degrading sensitivity.

The pixel layout, as shown in Figure 3.7(a), features a 3 $\times$ 3 array of metal-insulator-metal (MiM) capacitors, forming the core of the charge-sensing mechanism. The central capacitor (C_2) acts as the feedback capacitor, while the surrounding eight capacitors (C_1) are connected in parallel to serve as the sensing capacitor. This configuration results in an absolute voltage gain of 8 for the amplifier due to the capacitance ratio $C_1/C_2 = 8C/C$. The symmetrical arrangement of the capacitors ensures well-matched electrical characteristics, promoting precise gain in the differencing circuit [106].

The connection of the eight C_1 capacitors is achieved through a multi-layer fabrication process. Initially, an intermediate metallization layer (Metal 5) interconnects the lower electrodes, as shown in the cross-sectional view of Figure 3.7(c). Subsequently, the circuit is fabricated without a passivation layer above the top electrodes (metal top) of the C_1 capacitors, exposing them. Finally, a metal layer is deposited on top, effectively short-circuiting the eight electrodes and creating a single, large sensing capacitor. This design allows for two potential configurations: (i) After the Focused Ion Beam (FIB) deposition process, a solder bump can be added above the pixel, enabling connection to an external semiconductor detector (Figure 3.8), or (ii) the FIB-deposited metal can be left as is, serving as a protective layer against radiation effects (Figure 3.7).

The CMOS ASIC, depicted in Figure 3.9, was fabricated using UMC 0.18 µm technology and using a 3.3 V analog/digital supply. The chip was housed in a pin grid

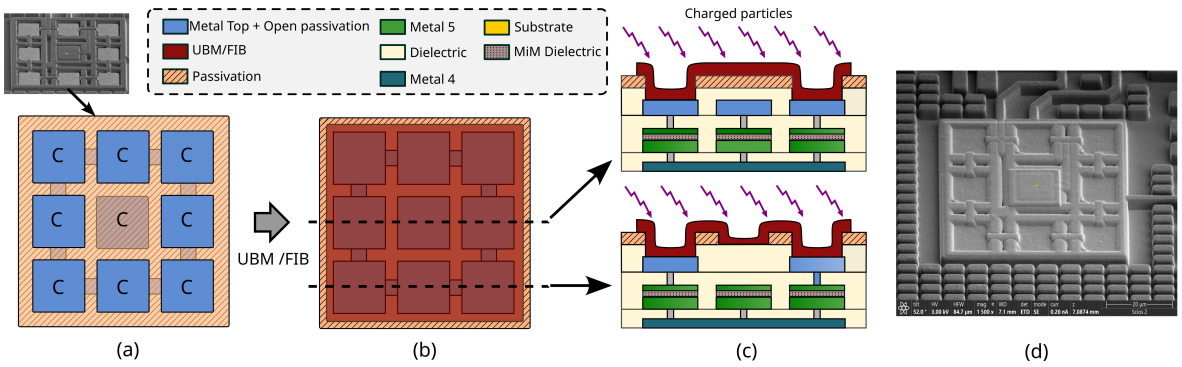

Figure 3.7: (a) Top-view of the capacitor array post-CMOS fabrication.(b) Top-view of the capacitor array after the metal deposition via FIB/UBM. (c) Cross-sectional view of the sensor arrangement illustrating the connection with the top metal and MiM capacitors. (d) Microscope image of the capacitor array after 1.2 µm Pt deposition with FIB [105].

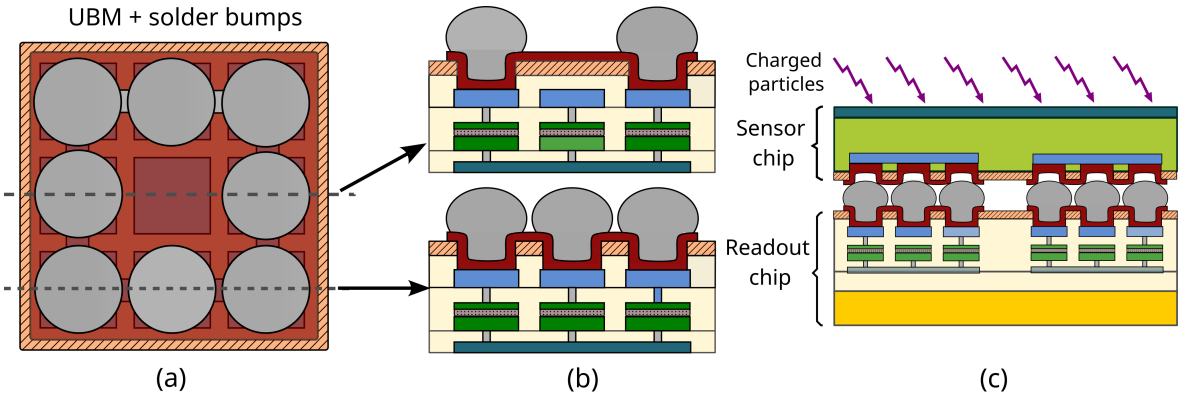

Figure 3.8: (a)Top-view of the capacitor array post-CMOS fabrication with solder bumps to connect an external detector. (b) Cross-view illustrating the connections and solder bumps. (c) Cross-view showing the connection with an external detector.

array (PGA) package with a removable cover lid to facilitate radiation exposure for testing. The microphotograph reveals a single test structure within the chip, showcasing the 3 × 3 array of MiM capacitors and surrounding circuitry, occupying an area of 55 µm × 55 µm. Each capacitor within the array measures 10.9 µm × 10.9 µm, offering a capacitance per unit area of 1 fF/µm^2 . The resulting capacitance values are $C_1 = 952$ fF (sensing capacitor) and $C_2 = 119$ fF (feedback capacitor), contributing to an absolute voltage gain of 8 for the amplifier.

The amplifier design is a streamlined adaptation of the self-biased folded-cascode differential pair presented in [119]. This configuration and two-stage comparators boasting rail-to-rail input capabilities enhance signal processing and discrimination. Transmission gates (TGs) with 600 nm channel lengths were employed for switching and control purposes. Notably, the analog circuitry was shielded by the top metal layer

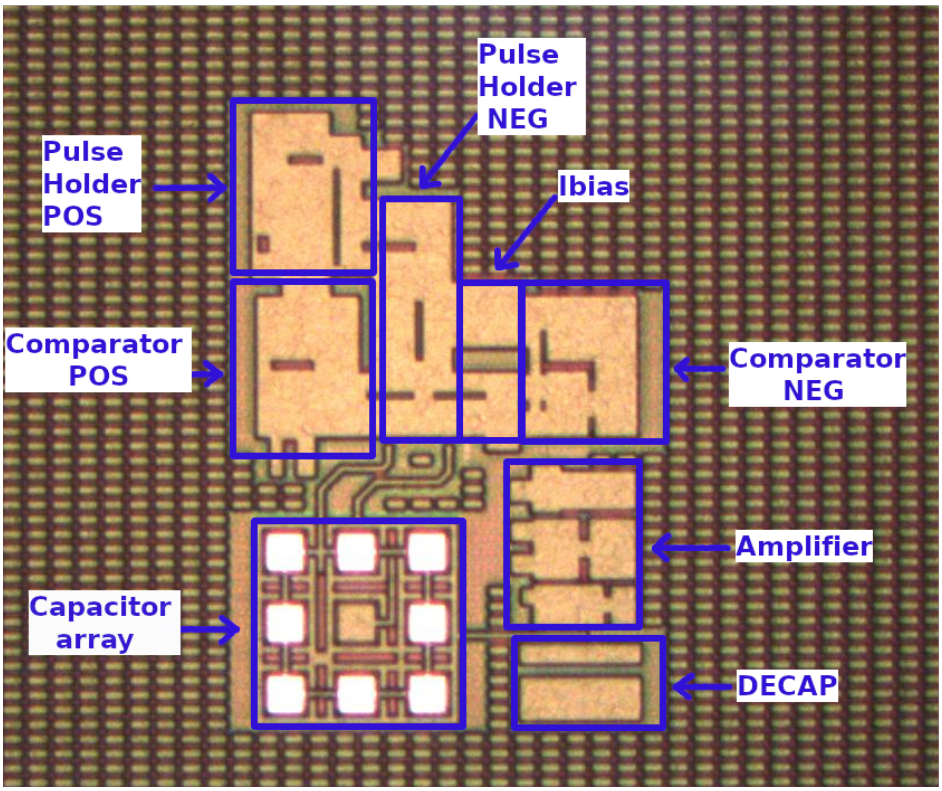

Figure 3.9: Light microscope photograph of the die portion containing the single pixel. Dimensions: Capacitor Array (55 µm × 55 µm), Amplifier (30 µm × 48 µm), Comparator (56 µm × 56 µm), Ibias (20 µm × 22 µm), Pulse Generator (22 µm × 46 µm), and DECAP capacitors (29.6 µm × 25 µm).

to mitigate potential radiation-induced damage, ensuring robust performance in the harsh EM environment.

3.2.3 Radiation hardening strategy

Following the CMOS fabrication process, a thick metallic layer was deposited on the capacitor array using a TESCAN SOLARIS UHR FESEM electron microscope equipped with a focused ion beam (FIB). This layer serves multiple crucial functions in enhancing the pixel's radiation hardness and overall performance:

- Firstly, the deposited metal layer acts as the floating electrode of the sensing capacitor (C_1), absorbing incident radiation up to a specific energy threshold determined by the metal's thickness. This deposition effectively shields the underlying readout circuitry from direct radiation exposure, preventing potential damage and ensuring stable operation.

- Secondly, the metal layer interconnects the top electrodes of the eight C_1 capac-

itors, enabling their parallel connection and contributing to the desired capacitance ratio for precise gain in the differencing circuit. This step is essential for achieving the required amplification and sensitivity of the pixel.

- Thirdly, the deposited metal is a protective shield, safeguarding any devices placed beneath it from radiation damage. This shielding is especially critical for sensitive analog components like the amplifier and comparators, which could otherwise suffer from degradation or malfunction due to prolonged radiation exposure.

- Finally, the metal layer protects the passivation oxide layer of the feedback capacitor (C_2) from electrostatic charging caused by direct electron irradiation. This charging effect can introduce noise and instability in the pixel's operation, compromising its performance and accuracy.

The choice of metal and its thickness are critical factors in determining the effectiveness of this radiation-hardening technique. The interaction of the incident electrons with the metal layer generates secondary electrons (SEs) and backscattered electrons (BSEs), quantified by their respective yields (η and δ). These yields depend on the material and the energy of the primary electrons. Therefore, the net current (I_A) absorbed by the top electrode of C_1 differs from the probe current (I_P) and can be expressed as:

$$I_A = I_P \cdot (1 - \sigma) \tag{3.8}$$

where $\sigma = \eta + \delta$ is the total electron emission yield [120]. Understanding this relationship is crucial for optimizing the design of the radiation-hardened pixel and predicting its response under various electron beam conditions.

Figure 3.10(a) illustrates Monte Carlo simulations conducted using CASINO [4] software [121] to assess the scattering losses of primary electrons impacting the pixel's metallic electrode. These simulations reveal that some electrons escape the electrode as backscattered (BSEs) and secondary electrons (SEs), while others penetrate and become trapped within the metal. The maximum penetration depth, Z_{max}, is influenced by the kinetic energy of the emitted electrons and the type of metal, as shown in Figure 3.10(b) for platinum (Pt), tungsten (W), and aluminum (Al). Due to the inherent vari-

[4] *CASINO* is a simulation software package for electron trajectory simulation in solids. It is widely used in EM research to model electron scattering and energy loss processes.

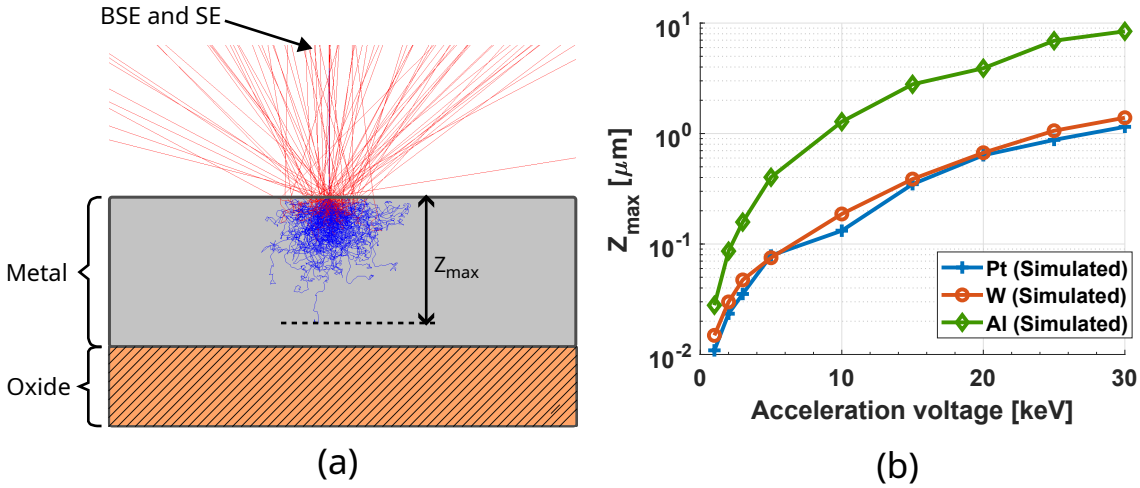

Figure 3.10: (a) Monte Carlo simulation of electron-matter interactions in SEM using Casino software, showing backscattered electrons (BSE, red) and secondary electrons (SE, blue) emitted from a metal layer on an oxide substrate. Z_{max} indicates the maximum depth primary electrons reach. (b) Maximum interaction depth (Z_{max}) as a function of acceleration voltage for different metal layers (Pt, W, and Al).

ability in deposited material properties, it is prudent to maintain a sufficient thickness margin to ensure adequate radiation protection. This study achieved reliable operation at energies up to 10 keV using a 1.2 µm platinum layer.

3.3. Results and Analysis

3.3.1 Matrix-Level Data Reduction and Efficiency

Figure 3.11 compares Address-Event Representation (AER) and sequential readout in EMPADs operating at a fixed frame rate of 100 kfps. The comparison considers varying pixel counts and incident electron flux (I_p). The data, generated through *MATLAB®* simulations, employs a discrete model for AER [5] with a uniform hit probability across all pixels.

In both subfigures (a) and (b), the blue curves represent the total number of bits transmitted per second for both AER (blue) and sequential readout (green) as a function of incident electron flux. The orange curves depict the theoretical information content per second, calculated using Shannon entropy [64], for the corresponding flux values using the equation (2.9).

[5]The AER protocol for a 2D detector is modeled as a discrete 3D matrix of size $N_{pix} \times N_{pix} \times N_{step}$, being N_{step} the number of time steps at a given time resolution, T_{res}. The *MATLAB®* code records an event as 1 when a pixel value changes and implements a simple arbitration scheme.

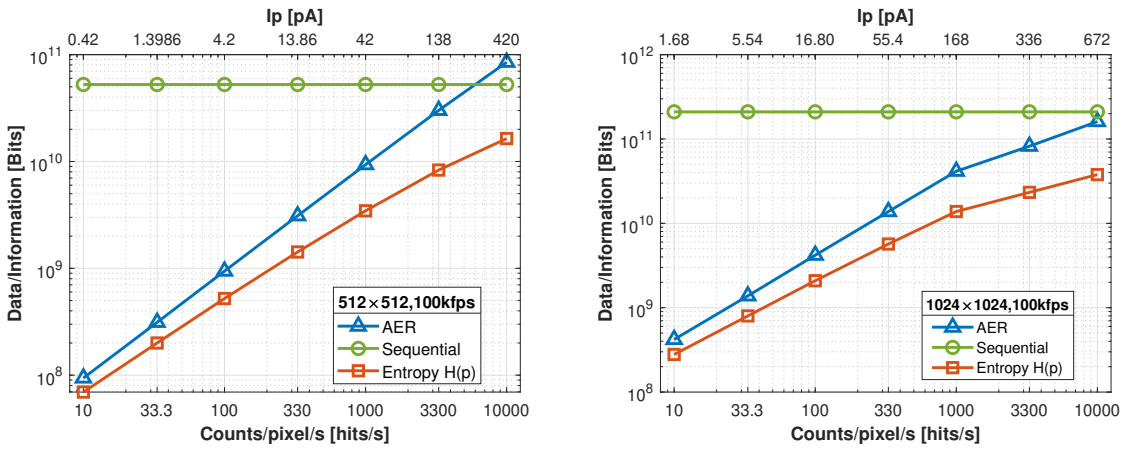

(a) (b)

Figure 3.11: Comparison of data transmission and information for AER and sequential readout in EMPADs working at 100 kfps and with varying pixel counts and exposure rates. (a) Results for a 512×512 pixel array (b) Results for a 1024×1024 pixel array.

The AER curves approach the theoretical lower limit defined by the Shannon entropy more closely than the sequential readout curves, underscoring their efficiency in transmitting only essential information. At low electron flux, the AER transmission rate reaches as low as 1.4 times the Shannon entropy, highlighting the protocol's exceptional effectiveness in minimizing data redundancy (see Section 2.4.2).

However, as the exposure rate increases, the AER data rate eventually surpasses the sequential readout. The reason is that each AER event requires transmitting both X and Y coordinates and the timestamp, leading to higher data overhead than the single value per pixel in sequential readout. While this intersection point serves as a crucial guideline for determining the optimal exposure rate for maximizing data efficiency in AER-based EMPADs, it is essential to note that the increased data rate at higher exposure rates does not pose a significant problem for AER. This increased data rate is because higher exposure rates also increase the risk of coincidence loss. Since we intend to propose AER-based EMPADs primarily for single-particle detection, they typically operate at lower exposure rates where coincidence loss is minimized, and the data reduction benefits of AER are most pronounced.

Figure 3.12 presents the results of simulations conducted using the same discrete model for an AER-based EMPAD with four different detector sizes (128×128, 256×256, 512×512, and 1024×1024 pixels), operating at a fixed exposure rate of 10^3 electrons per pixel per second (e^-/pix/s). The plot compares the data transmission rate using

AER-based (orange triangles) and frame-based (green circles) readout schemes across different frame rates. We also assess the compression ratio (R_c, purple line), defined as the ratio of data generated by the frame-based readout to that generated by the AER-based readout. A higher R_c value indicates superior data compression achieved by AER compared to frame-based approaches.

While the frame rate is a conventional concept for frame-based sensors, the refractory period, as detailed in Section 2.6.4, serves an analogous role in AER-based sensors, limiting the rate of consecutive events. In all four curves, the plot reveals two key intersection points (IPs) between the AER and frame-based data transfer curves: one at lower frame rates ($\sim 10^3$ fps), designated as IP_L and another at higher rates ($\sim 10^4$ fps), defined as IP_H. At medium frame rates (between these intersections), AER exhibits higher data transfer due to the transmission of X and Y coordinates for each hit and a timestamp, resulting in a data overhead compared to sequential transmission. However, at frame rates exceeding 10^4 fps, the benefits of AER become evident, with a significant reduction in data transfer compared to the frame-based approach, reaching compression factors (R_c) up to 7.3. This operating point is advantageous for data reduction and mitigating coincidence loss, as the probability of multiple electron hits on a pixel within a shorter frame or refractory period decreases.

Interestingly, as the frame rate decreases below 10^3 fps, the compression ratio R_c increases, indicating a growing advantage of AER regarding data reduction. This is because the number of detected hits per frame increases, and due to the DVS pixel's change-based detection mechanism, fewer differences are registered between consecutive frames, resulting in less data transmission for the AER scheme. However, operating at such low frame rates is not advisable due to the increased risk of coincidence loss, making this operating point impractical for single particle detection.

Now, let us explore the optimal operating regions for AER-based EMPADs, explicitly focusing on the range where the R_c exceeds 1, indicating a reduction in data transmission compared to frame-based readouts.

In Figure 3.13, this region is represented by the green-shaded areas, bounded by two key intersection points (IP) between the AER and frame-based data transfer curves: the lower intersection point (IP_L) and the upper intersection point (IP_H).

As the incident electron flux (count rate) increases, IP_L and IP_H shift linearly

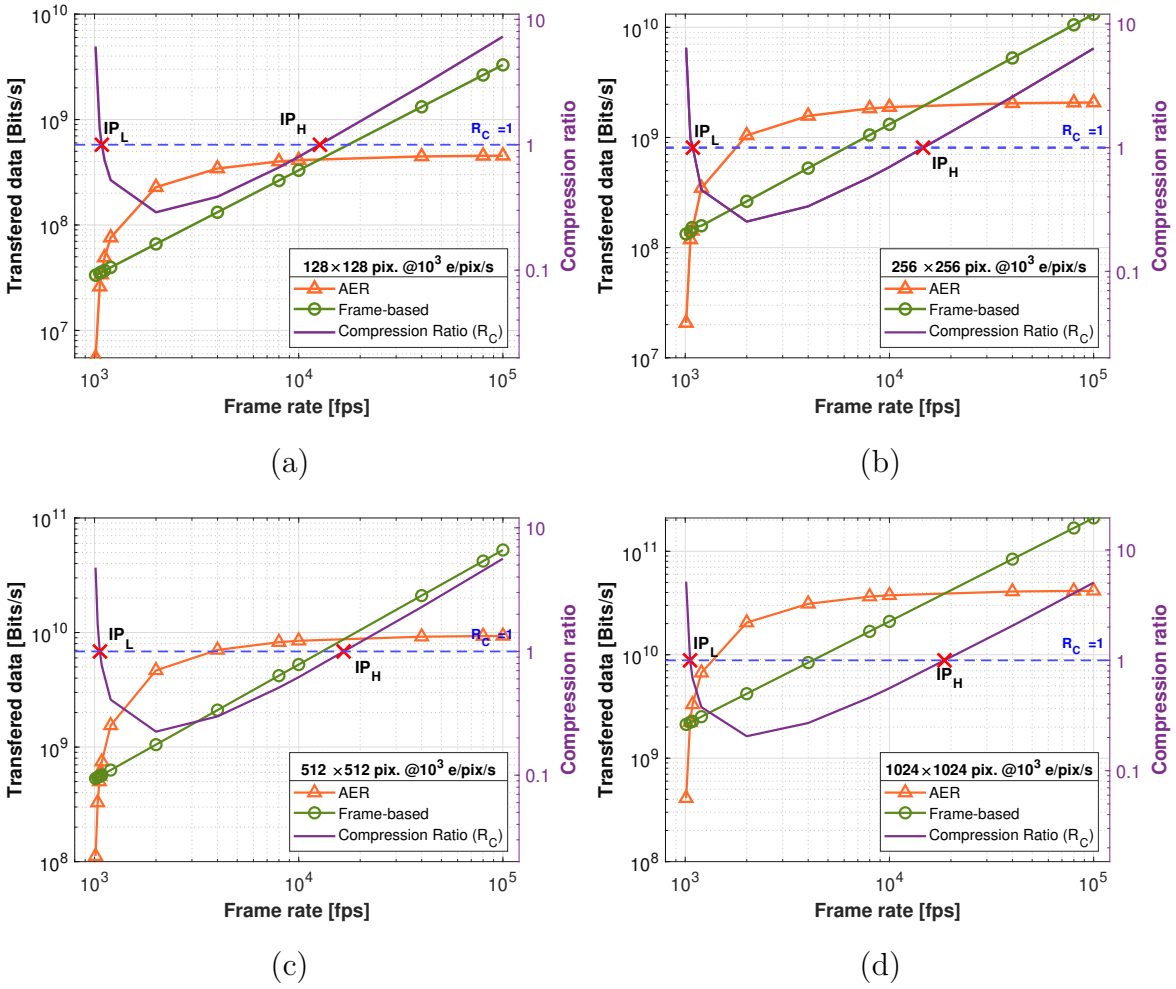

Figure 3.12: Comparison of data transmission and compression ratio between AER-based and frame-based readout schemes at a fixed exposure rate of 10^3 electrons per pixel per second (e^-/pix/s) for different pixel array sizes: (a) 128×128, (b)256×256, (c) 512×512, and (d) 1024×1024.

towards higher frame rates. The spacing between these two intersection points remains relatively constant across different count rates. This consistent behavior suggests that the optimal operating region for AER-based EMPADs scales proportionally with the incident electron flux, providing a valuable guideline for selecting appropriate frame rates to maximize data efficiency while avoiding coincidence loss.

To optimize single-particle detection of the AER-based EMPAD, operating in a regime where $R_c > 1$ and the frame rate is sufficiently high to mitigate coincidence loss is essential. This region typically corresponds to the green-shaded region in Figure 3.13 above IP_H. This region balances efficient data compression with the accurate detection and timing of individual electron events. Operating at frame rates below IP_L, while seemingly beneficial due to higher R_c values, is impractical for single-particle analysis as

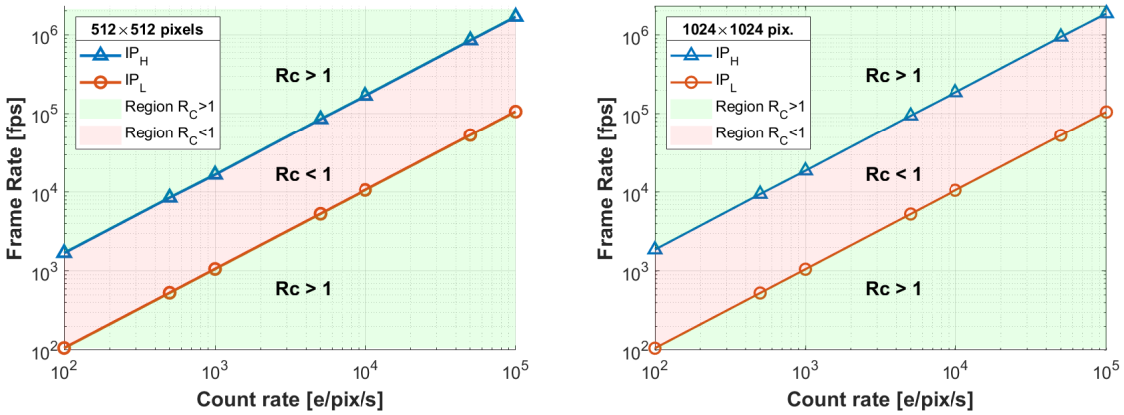

(a) (b)

Figure 3.13: Operating regions for an AER-based EMPAD, showing the relationship between frame rate (refractory period), count rate (e^-/pix/s), and R_c compared to a frame-based readout for two resolutions: (a) 512×512 (b) 1024×1024.

the increased number of events per frame leads to information loss due to coincidence losses. As mentioned before, this area can potentially be explored for operation in integration mode at the cost of degrading spatial resolution.

3.3.2 Pixel-Level Characterization

Test setup for Pixel Beam Irradiation

To validate the functionality and performance of the proposed pixel circuit, the pixel was subjected to direct irradiation under the electron beam of a TESCAN VEGA 4 scanning electron microscope (SEM) equipped with a tungsten filament. This experimental setup allowed for precise control of the electron beam current (I_P) and landing energy, which were adjustable between 1 pA - 2 nA and 200 eV - 30 keV, respectively. The nominal I_P was accurately calibrated at each step using a picoammeter Faraday cup (FC) within the SEM vacuum chamber.

As shown in Figure 3.14(a), the ASIC containing the pixel circuit was soldered onto a printed circuit board (PCB) and interfaced with an Artix-7 Opal Kelly FPGA board. This FPGA enabled control of the ASIC and facilitated data acquisition. The PCB and the ASIC were inserted into the SEM vacuum chamber, as depicted in Figure 3.14(b). A USB 3.0 feedthrough provided the necessary connection for interfacing with an external PC, allowing for seamless data transfer and real-time control of the experiment using a Python interface.

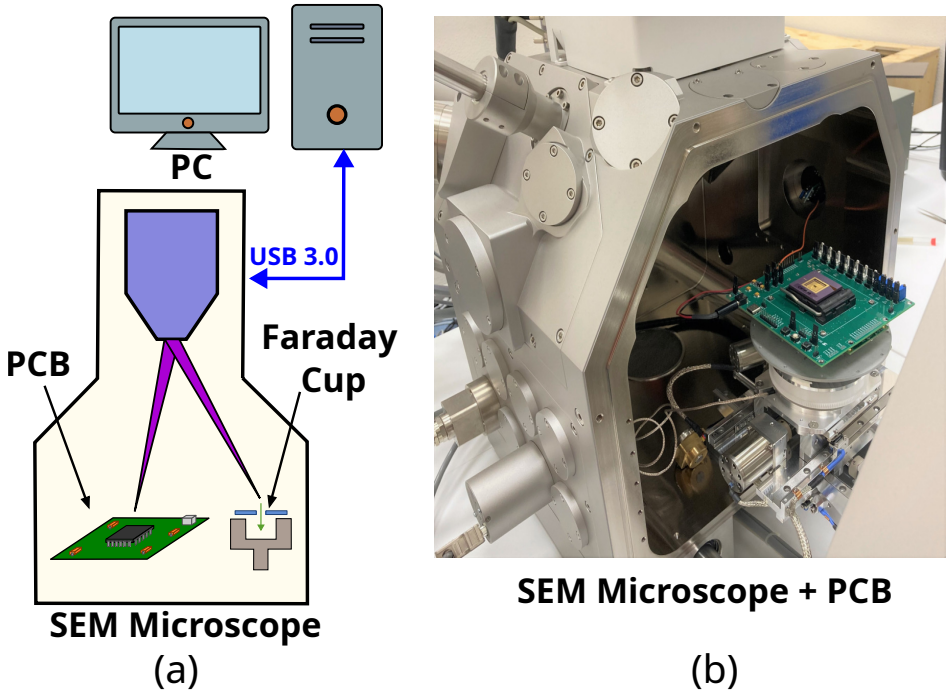

Figure 3.14: (a) Primary setup involves using an SEM with an internal field emission gun (FEG) and a PC connection. (b) Image of the PCB with the application-specific integrated circuit (ASIC) inside the SEM chamber.

The sensor was tested by irradiating the top metal layer of the capacitive array with the electron beam. The beam, focusable to a spot size smaller than 10 nm, was centered on the capacitor array of the circuit. Initially, the electron energy was fixed at 3 keV, and the signal frequency ($f_{p,n}$) generated by the circuit was measured for nine different probe currents (I_P) ranging from 1 pA to 10 nA. The same procedure was repeated with an electron energy of 10 keV and four different probe currents within the same range. For each current step, I_P was independently calibrated using the Faraday cup to accurately measure the incident electron flux.

Sensitivity Results

The sensitivity of the proposed pixel circuit was evaluated by measuring the output negative frequency (f_n) under different probe currents (I_P) and electron energies (3 keV and 10 keV), as shown in Figure 3.15 (a). Since the frequency is dependent on the actual net current (I_A) at the input electrode, the total electron emission yield (σ) was extracted by utilizing Equation 3.8 and independently calculating I_P and I_A. At higher energies, discrepancies between the experimental results and theoretical calculations were observed, possibly due to the non-uniformity of the deposited platinum layer, attributed to contamination during FIB deposition with other elements from the

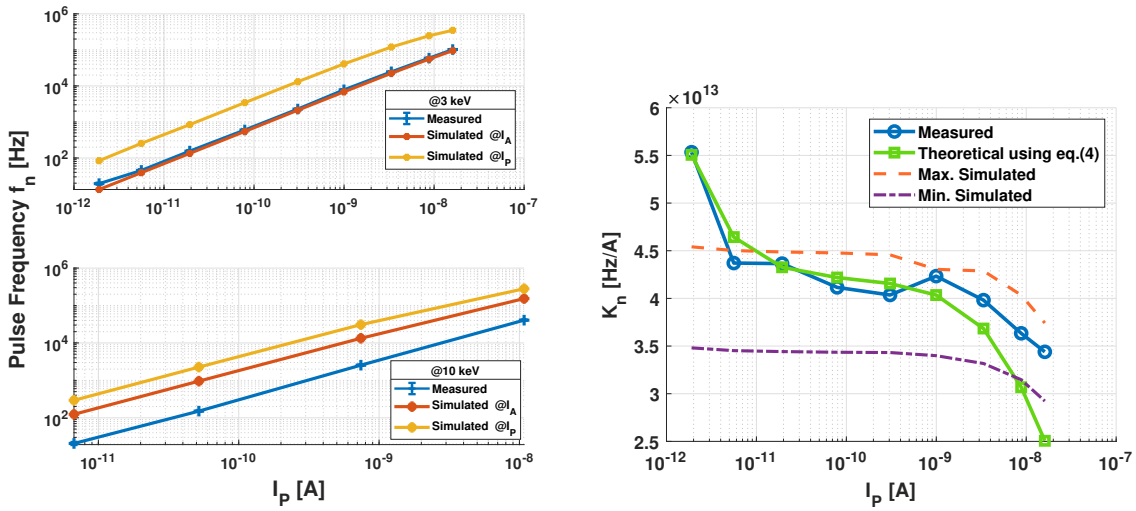

(a) (b)

Figure 3.15: (a) Investigating the correlation between pulse frequency and current probe (I_P) for negative charges at 3 keV and 10 keV energy levels. (b) The sensitivity (K_n) as a function of different current probes (I_P). This data is derived from measurement results, theoretical expressions, and simulation values.

Table 3.1. *Measurement results for the leakage in four different samples and estimation of DR using Eq. (3.6).*

Parameter	Sample			
	#1	#2	#3	#4
I_{leak} [(a)]	5.0 fA	4.7 fA	7.5 fA	13.2 fA
DR [(b)]	119 dB	119 dB	119 dB	118 dB
[(a)] Measured at $T_j = 25\ ^oC$.				
[(b)] Estimated for $\Delta V_{p,n} = 0.2$ V.				

precursor gas and residual molecules in the chamber [122].

Table 3.1 presents the estimated input current leakage (I_leak) values, derived from pulse frequency measurements without any input stimulus at a junction temperature (T_j) of 25^o C, using Equation (3.2) with a $\Delta V_{p,n} = 0.2$ V. These leakage values, primarily injected from V_{REF} through the TGs, were subsequently used to calculate the dynamic range (DR) of the sensor.

The pixel circuit's sensitivity ($K_{p,n}$) can be derived from the frequency measurements at 3 keV and plotted as a function of I_P, as shown in Figure 9. The plot includes the minimum and maximum bounds for sensitivity, considering process variations, and compares these to the theoretical model described in Equation (3.4). Treating I_{leak} as a fitting parameter, we obtained a value of -590 fA, which is higher than typically

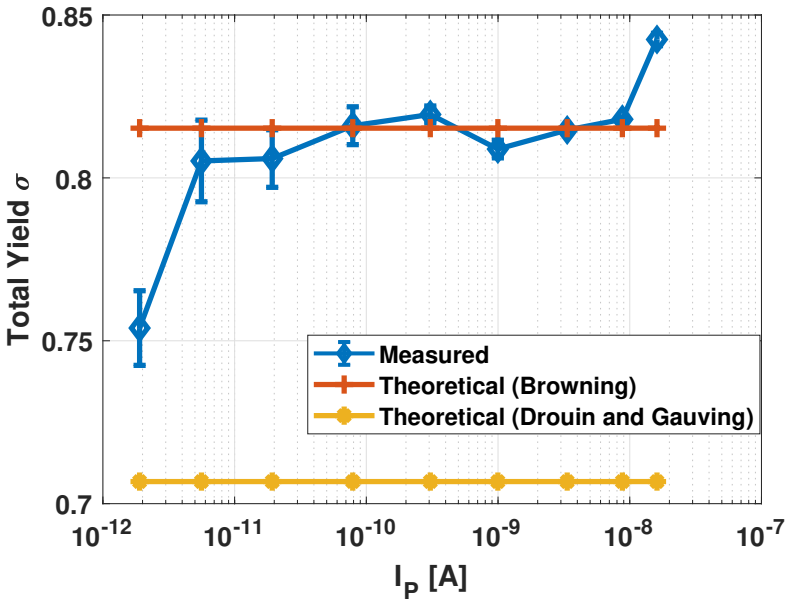

Figure 3.16: Total electron emission yield (σ) is plotted as a function of various current probes I_P using data from measurements and the models proposed by Browning [114] and Drouin and Gauvin [123].

measured values (Table 3.1) due to poor thermal dissipation within the SEM vacuum chamber. Prolonged tests revealed junction temperatures exceeding 65^oC, underscoring the need for improved thermal management strategies, potentially involving external placement of the FPGA and primary regulators.

Total electron yield

Figure 3.16 presents an extrapolation of the total electron emission yield (σ) based on the measured pulse frequencies at 3 keV and Equation (3.8). The experimental results were compared with two theoretical models of σ (Browning [114] and Drouin and Gauvin [123]) using CASINO software [121]. The Browning model best fits the experimental data, providing a more accurate representation of the electron-matter interactions in the platinum layer. It is worth highlighting that the total yield estimation (blue line) shows an inverse relationship with the sensitivity curve depicted in Figure 3.15(b). This emphasizes the importance of maintaining a highly linear sensitivity across the entire range of beam currents to ensure accurate and consistent yield estimation. The proposed pixel and the yield estimation procedure have been published in [105].

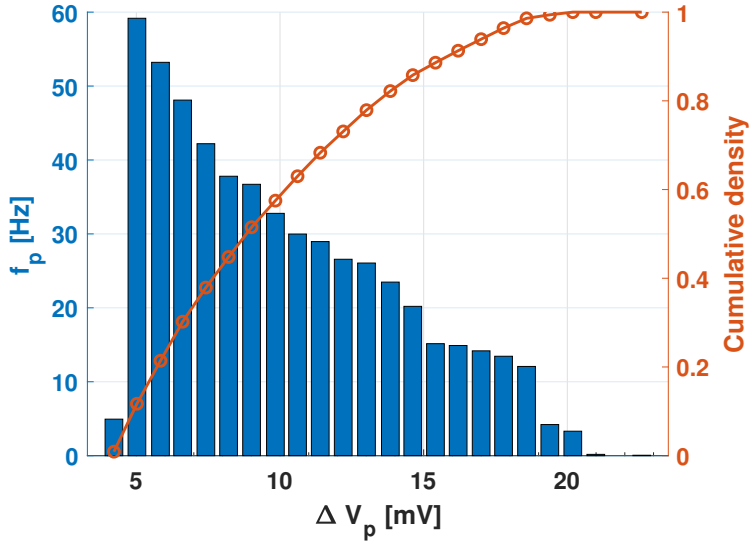

Figure 3.17: The frequency of positive pulses changes as V_H varies close to V_{REF} ($\Delta V_p = V_H - V_{REF}$) over a sampling duration of 300 s[6].

Pixel Noise

The noise characterization of the pixel circuit was conducted under dark conditions (i.e., without electron beam exposure) by systematically varying the high and low threshold voltages (V_H and V_L) around the reference voltage (V_{REF}). The first step involved a coarse adjustment of the thresholds until pulses were observed in both positive and negative directions, indicating the presence of an offset voltage (V_{OS}) in the amplifier and comparator stages. The direction of the imbalance between positive and negative sensitivities revealed the sign of V_{OS}.

Following this, a fine adjustment of the threshold associated with the offset direction (V_H or V_L) was performed. This fine-tuning was accomplished by incrementally sweeping the threshold voltage using the least significant bit (LSB) voltage (805 µV) of a 12-bit DAC (TI DAC124S085) [124]. The average frequency of the generated pulses was recorded as the threshold voltage approached V_{REF}, as shown in Figure 3.17.

By analyzing the measured data and considering the offset voltage ($V_{OS} \approx 4.6$ mV), the input-referred noise (IRN) was calculated. The resulting value for the IRN, σ_{IN}, was determined to be 24.8 fArms. This value encompasses the noise contribution from the voltage threshold references, which was not specified in the datasheet.

[6]Increasing the sampling time enables the system to capture slow fluctuations more effectively, improving the analysis and measurement of flicker noise, which is more pronounced at low frequencies.

3.3.3 Comparative Analysis

Table 3.2 compares the implemented sensor's specifications against state-of-the-art charge detection approaches. Medipix [101], a commercial direct EMPAD based on flip-chip technology, stands out for its radiation hardness and high sensitivity due to intrinsic amplification by converting incident radiation into electron-hole pairs. However, this vertical integration approach has limitations: high fabrication cost, low yield, non-linear sensitivity to energy and fluence, and the need for careful thickness adjustment of the sensing layer based on the energy range.

In contrast, the proposed sensor in this work measures net charge accumulation on a capacitor. The top metallic plate of the capacitor is irradiated with the electron beam, and an uncompensated electric charge builds up in an amount that depends on the total electron emission yield of the material used for the plate (σ). Because the emission yield is close to unity (close to 1.18 as depicted in Figure 3.16), our pixel does not inherently amplify the signal (like conventional sensors based on measuring freed e-h pairs), resulting in lower sensitivity compared to Medipix. Nevertheless, as Table 3.2 highlights, the charge-sensing approach of our pixel demonstrates competitiveness regarding dynamic range (DR), linearity, latency, and power consumption.

The proposed sensor's compatibility with standard CMOS planar integration presents a significant advantage in terms of fabrication cost and yield. While the current design is conservative, future iterations can potentially position the circuitry beneath the sensing array, further enhancing the fill ratio and transforming the test structure into a radiation-hardened pixel suitable for focal-plane arrays. The common-centroid distribution of capacitors in the sensing array minimizes offsets between adjacent pixels, reducing fixed pattern noise (FPN).

Integrating this pixel design into a matrix connected to AER arbitration circuitry eliminates the need for one-shot circuits, simplifying the overall design. Additionally, modern AER readout circuitry can handle pixel event rates up to 100 Meps [7, 116], sufficient for rendering images with pulse density modulation (PDM) encoding [127].

The compactness, high sensitivity, and compatibility with standard CMOS fabrication make this sensor design appealing for various charge detection applications beyond electron microscopy, such as mass spectrometry, space radiation detection, and biosensing based on electrostatic induction [128, 129]. While FIB deposition is not scal-

Table 3.2. *Comparative analysis of State-of-the-Art approaches.*

Parameter	This work (2023) [105]	Sakamoto (2012) [125]	Medipix (2013) [101]	Song (2020) [115]	Song (2022) [126]
Technology	0.18 µm CMOS	0.2 µm CMOS	0.13 µm CMOS	0.18 µm CMOS	0.18 µm CMOS
Manufactur.	Planar (On-chip)	Planar (On-chip)	3D Integration (Flip-Chip)	External FC (PCB)	External FC (PCB)
Supply Voltage	3.3 V	3.3 V / 1.5 V	1.5 V	1.8 V	1.8 V
Power Consumption (per pixel)	161 µW	ND	9 µW	5.5 mW	2.2 mW
Rad Hard	Yes (Low Energy)	Yes (Low Energy)	Yes (Hybrid)	Yes	Yes
Conversion Gain	1.43 $\mu V/e^-$	150 μV/ion	11.4 $\mu V/e^-$	8.9 $\mu V/e^-$	15.0 $\mu V/e^-$
Dynamic Range	118 dB[(a)]	70 dB	ND	ND	ND
IRN	7031 e^-rms	3 ions[(b)]	80 e^- to 175 e^-	475 e^-rms	221 e^-rms
Sensing Area	55 × 55 µm^2	7 × 7 µm^2	55 × 55 µm^2	1 × 1 cm^2	ND
Complexity	96 transistors	4 transistors	∼ 1600 transistors	> 23 transistors	ND
Latency	1 μs[(c)]	1 μs	491 µs/ frame	NA	NA
Dark Current	7.6 fA[(d)]	ND	−10 nA to +20 nA	30 pA	ND

[(a)] Measured at $\Delta V_{p,n} = 0.2$ V. It could reach up to 138 dB using $\Delta V_{p,n} = 1.6$ V.

[(b)] Measured at $T = 181$ K.

[(c)] In a closed-loop configuration utilizing a one-shot circuit. The delays of logic cells and collisions constrain the effective latency in AER implementations.

[(d)] Mean value with $\sigma = 3.9$ fA.

able for large pixel arrays, alternative approaches like vertical integration technologies with top surface metallurgy (TSM) can provide radiation hardening without the need for costly flip-chip hybridization [130], paving the way for future development of large-scale, radiation-hardened focal plane arrays based on this pixel design.

3.4. Final Remarks

This chapter has presented the design and implementation of a novel, asynchronous, radhard, charge-sensitive pixel for electron microscopy applications. The pixel archi-

tecture, compatible with the AER communication protocol, enables high-speed, event-driven readout of electron impact events, reducing data redundancy and facilitating real-time analysis. The pixel's radiation-hardened design, achieved through the deposition of a 1.2 μm platinum layer, ensures its robustness and longevity in the demanding environment of electron microscopy. Experimental validation using an SEM demonstrated the pixel's high dynamic range, linearity, and sensitivity to beam currents between 1 pA and 10 nA and kinetic energies between 3 and 10 keV. These results align well with simulations, further validating the efficacy of the proposed design.

This pixel design represents a significant advancement in EMPAD technology, offering a pathway toward more efficient, information-centric detectors for electron microscopy. The combination of direct charge sensing, asynchronous operation, and radiation hardness addresses traditional EMPADs' critical challenges. Future work will focus on integrating this pixel design into a focal-plane array and optimizing the underlying circuitry for enhanced performance and functionality.

Chapter 4

Implementation of a Neuromorphic EMPAD with Spectral Sensitivity

Building on the neuromorphic EMPAD design from Chapter 3, this chapter explores how to add spectral sensitivity to detect color (energy) information in electron microscopy detectors.

In this work, inspired by the Foveon X3 sensor [131], which uses stacked photodiodes to capture different light wavelengths, we propose a similar stacked diode setup for EMPADs to differentiate between electrons of various energies [132]. We will start by explaining the basics of spectral sensitivity in EMPADs and why stacked diodes are effective for energy discrimination. Then, we will describe a specific stacked diode EMPAD design, covering its architecture, pixel layout, and how it fits with the neuromorphic AER protocol. We will also review the design and layout considerations to improve spatial and spectral resolution.

We also explore integrating a neuromorphic ToT measurement approach using a derivative circuit, as discussed in Section 4.4. This method improves temporal resolution and reduces coincidence loss, enabling more accurate and efficient event detection.

In the final section, we will show experimental results demonstrating the optical imaging sensitivity and dynamic range of the stacked diode EMPAD.

4.1. Principles of Energy Discrimination in EM

In EM, analyzing the spectral distribution of energy loss in an electron beam provides invaluable insights into the composition and structure of materials at the atomic and molecular levels. Various techniques exist for spectral analysis, such as Energy Dispersive X-ray Spectroscopy (EDS), Cathodoluminescence (CL), X-ray Photoelectron Spectroscopy (XPS), and Electron Energy Loss Spectroscopy (EELS). EELS[1] that is measured with a complex detector called a spectrometer is particularly well-suited for integration with 4D-STEM techniques, offering the potential for multimodal, information-centric electron microscopy. Figure 4.1 illustrates this concept through a graphic of a specific 4D-STEM and EELS data acquisition setup. Integrating an EELS spectrometer with a pixelated detector featuring a center hole can simultaneously capture diffraction patterns $I(k_x, k_y)$ and energy loss spectra $\Delta E(c_x, c_y)$. This concurrent acquisition allows for a more detailed sample structure and composition analysis [11].

A direct electron detector, on the other hand, could, in principle, be used to simultaneously measure both the energy, E, and intensity, I, of incoming electrons, increasing the data dimensionality beyond the conventional two-dimensional spatial information $(x,\, y; I)$ of each pixel to $(x,\, y; I, E)$. The Timepix detector [82] is part of the well-established Medipix family of hybrid pixel detectors, widely used as EMPADs. It is distinguished by its ability to measure the energy of incoming radiation directly within the detector itself using Time-over-Threshold (ToT) measurements. This EMPAD utilizes a silicon sensor bump-bonded to a CMOS application-specific integrated circuit (ASIC). Each pixel in the sensor has a dedicated event counter, and incident electrons generate electron-hole pairs collected by the readout electronics under an applied bias voltage. An adjustable threshold determines the minimum energy deposition required for a count to be registered [34]. However, the charge carriers from a single primary electron can spread over multiple pixels (charge sharing), as explained in Chapter 2. Such a phenomenon can result in a variable computation per electron,

[1] EELS measures the energy lost by the electrons of a monochromatic incident electron beam as it interacts with the sample. The energy losses of the electrons are represented as a curve of probability of occurrence, distributed across a continuous range of values spanning energies from eV to approximately 2 keV. The curve of losses, known as the EELS spectrum, contains fine details encoding information of a wide range of sample excitations, from single electron excitations to plasmon resonances and core-loss ionization edges [133].

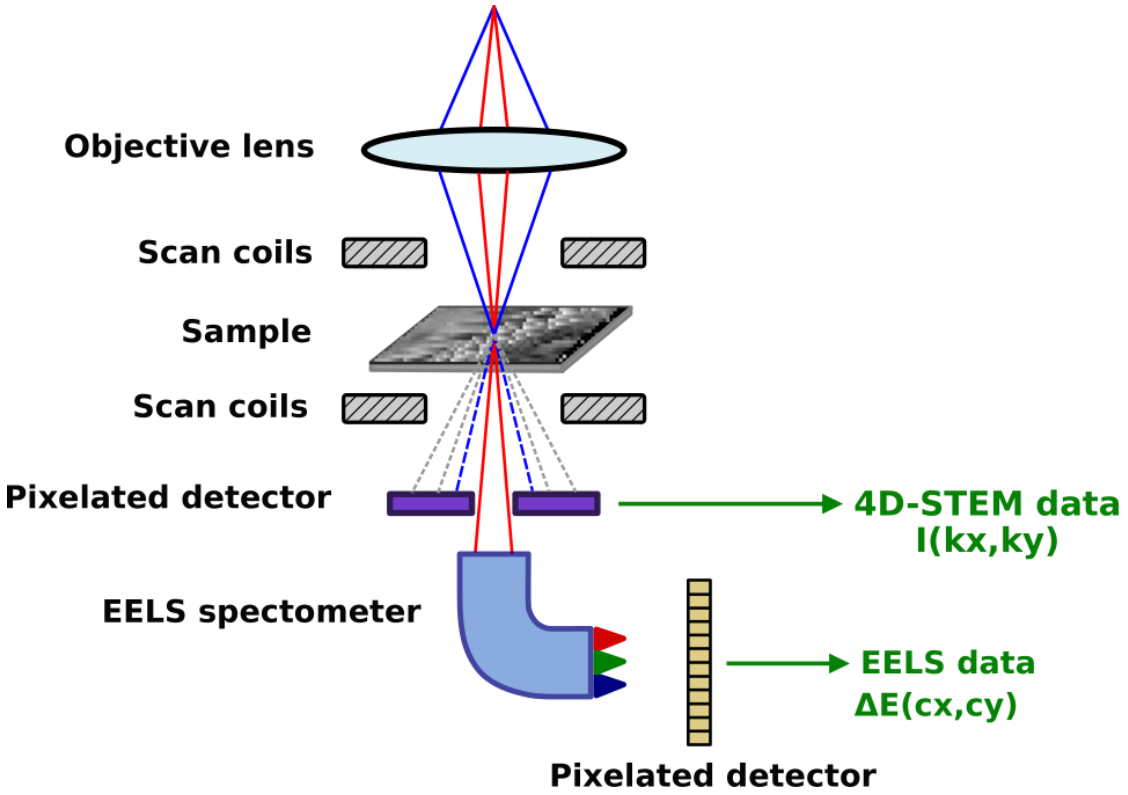

Figure 4.1: One proposed approach for simultaneous acquisition of 4D-STEM and EELS data using two fast pixelated detectors: one with a center hole to capture the CBED and the other one to capture the EELS spectra. Adapted from [16, 134].

with the count depending on factors such as the primary electron energy, detector threshold, and impact point [135]. The challenge of achieving accurate energy discrimination in EMPADs underscores the complexity of precise material analysis, opening the possibility of researching in this area. Currently, such hybrid EMPAD measurements achieve feeble energy resolutions of approximately 1 keV, compared to the resolution of a typical X-ray SDD spectrometer of 127 eV or modern EELS spectrometers of 1 eV.

In this work, we have investigated the development of EMPADs with internal spectral sensitivity by leveraging the advantages of direct electron detection. The aim is to address the challenges associated with traditional EELS detectors (they are bulky, complex, and costly) by developing EMPADs that can directly produce images in color (with energy information) associated with the energy of the electrons impacting every pixel.

4.2. Spectral Sensitivity in EMPADs

4.2.1 Depth-Based Energy Discrimination: Stacked Diodes Approach

The principle underlying particle energy measurement using stacked diodes exploits the depth-dependent energy deposition of particles as they interact with matter. Photons and electrons can create electron-hole (e^--h^+) pairs in a silicon diode by freeing charge carriers when they hit the material. Due to impact ionization, electron-hole pairs are not uniformly formed across the material. The diode depletion region, characterized by a strong electric field, favors the creation of these charge carriers. The electric field accelerates and separates the negative and positive carriers before they recombine, increasing their kinetic energy and enabling them to trigger additional ionization events.

The graph in Figure 4.2 illustrates the interaction of both light and electrons with a silicon diode, focusing on the relationship between penetration depth and energy. In the case of photons, the depth at which they interact with silicon is inversely proportional to their energy. High-energy photons (e.g., blue light) with shorter wavelengths are absorbed near the surface due to their strong absorption coefficient. In contrast, lower-energy photons (e.g., red light) with longer wavelengths penetrate deeper into the silicon before being absorbed [132,136]. Comparatively, electrons interact differently with silicon. Electrons with higher energy tend to penetrate deeper into the material, while lower-energy electrons are more likely to be absorbed closer to the surface [132]. This behavior contrasts with photons, where higher energy leads to shallower absorption depths, illustrating the fundamental difference between how light and charged particles interact with semiconductor materials like silicon.

Another essential aspect that Figure 4.2 reveals is the similarities in the electron energies that can be detected using standard CMOS stacked diodes (D1, D2, and D3) and those available in SEM microscopy. The absorption depth principle could detect energy levels of electrons coming from the primary beam or secondary/backscattered electrons or transmitted electrons from 4D-STEM in SEM, facilitating the acquisition of spatial and spectral data. The stacked diode setup takes advantage of this principle by natively placing each at a distinct depth within the silicon. By detecting which diode(s) register a signal, we can determine the incoming light's energy (or wavelength). D1, closest to the surface, primarily detects higher-energy photons, while D3, positioned

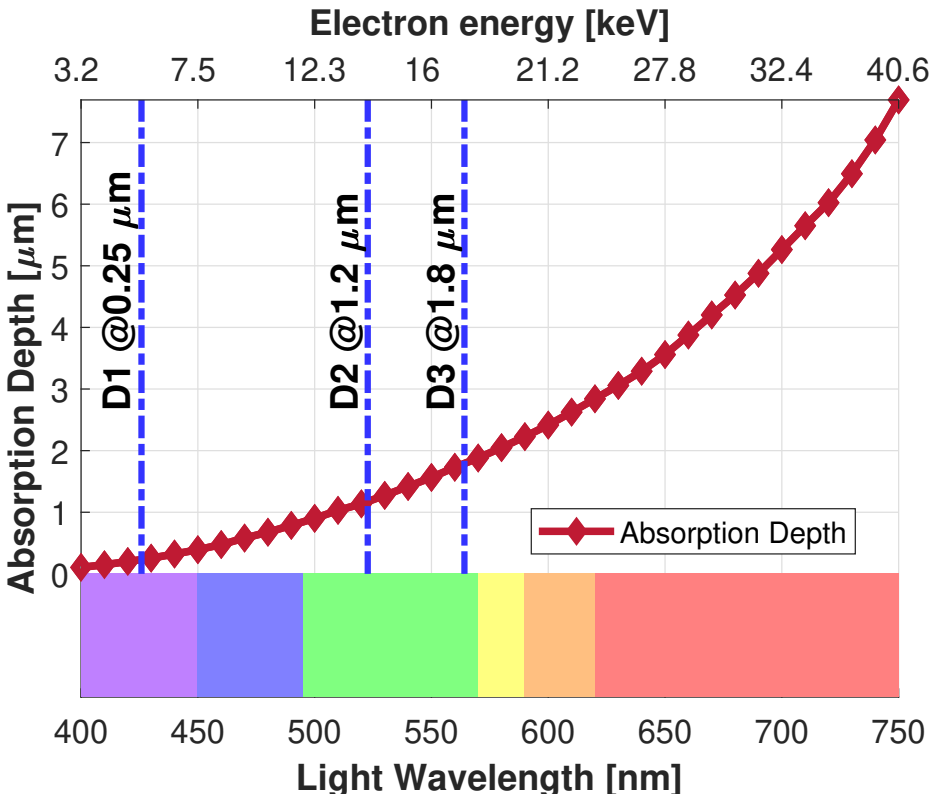

Figure 4.2: Light absorption depth vs. light wavelength. Stacked diodes (D1, D2, D3) at different depths can capture light of certain wavelengths, enabling color detection.

deeper, responds to lower-energy photons. D2 covers the intermediate range. This arrangement distinguishes various light colors or energies and forms the basis for color or spectral imaging. Stacked diode configurations like this are commercially available and can be manufactured using standard CMOS processes.

Understanding how these configurations operate also involves considering the interaction volume within the material. The interaction volume represents the region within the material where the electron that impacts a piece of material undergoes scattering and energy loss processes until it is completely absorbed or until it reaches an exit surface. The electron's penetration depth, often approximated by a spherical interaction volume with diameter R, depends on the beam energy and the material properties [132, 137]. As shown in Figures 4.3(a) and 4.3(b), the size of the interaction volume in silicon increases with the electron's energy, with a 5 keV electron exhibiting a smaller interaction volume than a 30 keV electron. This data was obtained using the Monte Carlo software *CASINO* [121].

To estimate the diameter R, representing the maximum distance traveled, you can use one of several semi-empirical formulas in the literature. For example, Kanaya

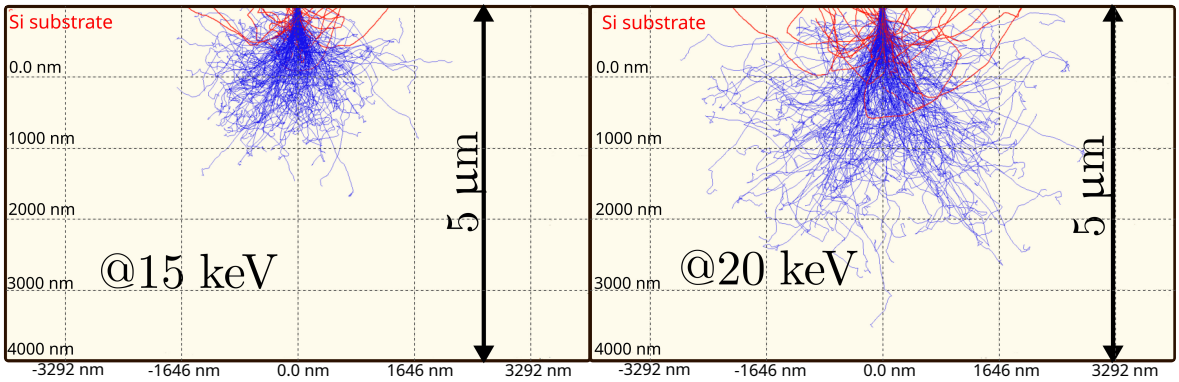

Figure 4.3: Monte Carlo simulations depicting the trajectories of electrons (absorbed and backscattered, in blue and red, respectively) in a silicon substrate at two different acceleration voltages: 15 and 20 keV.

and Okayama in [138] propose the following formula:

$$R_{K-0} = \frac{0.0276A}{\rho \cdot Z^{0.89}} E^{1.67} \quad [\mu m] \tag{4.1}$$

Alternatively, Potts in [139] provides another expression:

$$R_P = \frac{0.1}{\rho} E^{-1.5} [\mu m] \tag{4.2}$$

where A is the atomic weight in g/mol, ρ is the material's density in g/cm^3, Z represents the atomic number of the incident material, and E is the energy of the incident beam in keV.

Notably, these penetration depths are similar to those of the junctions of stacked photodiodes found in standard CMOS integration technologies [132]. This compatibility allows for designing EMPADs with multiple diode layers stacked vertically (usually up to three), each sensitive to a specific range of electron energies.

This depth-dependent energy loss is the basis for stacked diode energy discrimination. Stacking multiple diodes at different depths within the silicon substrate makes it possible to differentiate between electrons of varying energies. Lower-energy electrons will be absorbed in the shallower diodes, while higher-energy electrons will penetrate deeper into the stack before being fully absorbed. The incident electron's energy can be estimated by analyzing and combining the three signals measured at each stacked diode.

4.2.2 Time-Based Energy Discrimination: The ToT Approach

The Time-over-Threshold (ToT) method offers an alternative approach to energy discrimination in EMPADs, particularly in scenarios where fast signal processing and multi-channel readout are desired [140]. This technique measures the duration for which the amplified signal from an electron impact remains above a predefined threshold, indirectly estimating the deposited energy. However, the ToT method faces challenges due to the inherent non-linear relationship between the input charge and the resulting pulse width [141, 142].

Despite this limitation, ToT has gained popularity due to its potential for simplifying readout architectures and enabling high-speed operation. The Timepix chip [82], an evolution of the Medipix2, exemplifies this approach by allowing for independent measurement of arrival time, ToT, and event counting in each pixel.

ToT Fundamentals

The total registered charge of a pixel cluster depends on various factors, including particle energy, interaction location and depth, bias voltage, preamplifier noise, mismatch, and threshold level. As discussed in Chapter 3, charge-sharing can further complicate energy estimation.

The fundamental principle behind ToT lies in the relationship between a particle's deposited energy (E_d) and the number of generated electron-hole pairs (N) generated in the detector. The average number of electron-hole pairs generated by an electron impacting a detector is given by:

$$N = \frac{E_d}{\epsilon} \tag{4.3}$$

where ϵ is the average energy required to create an electron-hole pair in the detector's material (approximately 3.6 eV for silicon) [143]. Although the process is complex, the spatial distribution of these charge carriers is often modeled using a Gaussian distribution whose radius is influenced by the deposited energy and the specific hit location within the detector.

Figure 4.4 presents a typical circuit implementation for ToT measurements in an EMPAD pixel. The incoming signal from the detector is first processed by a Charge

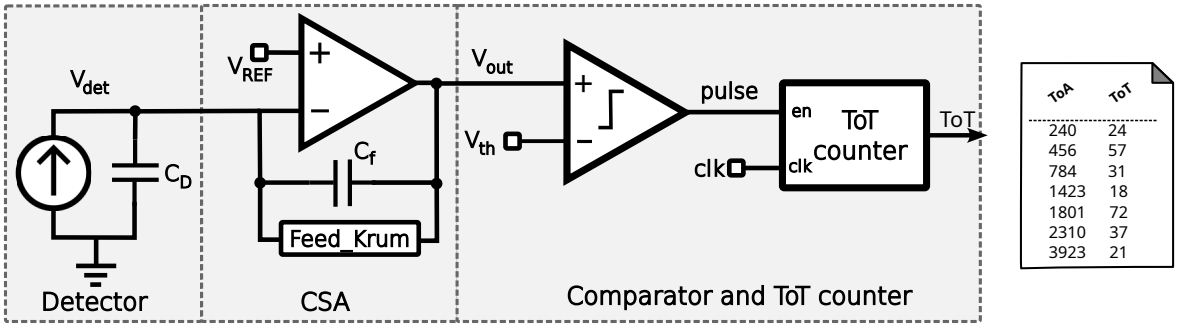

Figure 4.4: Circuit diagram for a pixel implementing Time-over-Threshold (ToT) measurement.

Sensitive Amplifier (CSA), which converts the charge generated by an electron impact into a voltage signal. Traditional CSAs utilize periodic reset signals to discharge the feedback capacitor, resulting in dead times during which the amplifier cannot process incoming signals. In contrast, Krummenacher feedback offers a continuous discharge path, enabling the CSA to operate without interruption [103]. A comparator compares the voltage against a threshold voltage (V_{th}). When the amplified signal exceeds the threshold, the comparator output triggers a pulse generator, enabling a counter through the signal *en* and recording the Time of Arrival (ToA). The counter increments with each clock cycle (*clk*) as long as the amplified signal remains above the threshold. The counter stops once the signal falls below the threshold and the ToT value is stored. This value, representing the duration the signal was above the threshold, is transmitted along with the pixel address using, for example, the AER protocol. This method indirectly estimates the signal's charge and deposited energy by measuring the number of clock ticks over this condition.

The following equation can approximate the output waveform of a CSA in response to an input charge (represented as a Heaviside step function of a short pulse) [144]:

$$V_{out}(t) = V_{max} \cdot \left(\frac{t}{\tau}\right) \exp\left(-t/\tau\right) \tag{4.4}$$

where V_{max} represents the peak output voltage of the CSA, which is directly proportional to the magnitude of the input charge or deposited energy, and τ is the circuit's time constant.

Figure 4.5 depicts the output voltage response (V_{out}) of a CSA over time. This

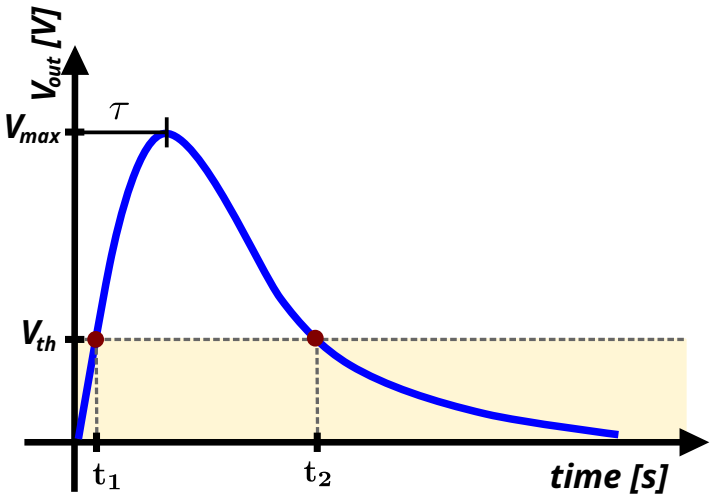

Figure 4.5: Output waveform of a Charge Sensitive Amplifier (CSA) showing Time-over-Threshold (ToT) measurement.

behavior is characteristic of the response to an input charge, such as that generated by an electron impacting a detector.

Mathematically, finding the ToT involves solving the equation $V_{out}(t) = V_{th}$. This equation has two solutions for our region of interest, t_1 and t_2, corresponding to the rising (time of arrival ToA) and falling edges of the CSA output crossing the threshold. As the graph shows, the CSA output rises above V_{th} at t_1, remains above it for the time ToT, and falls below V_{th} at t_2. Utilizing a first-order Taylor approximation, the solutions can be approximated as:

$$t_1 = \frac{\tau}{2}\left[1 - \sqrt{1 - 4\left(\frac{V_{th}}{V_{max}}\right)}\right] \tag{4.5}$$

$$t_2 = \frac{\tau \cdot a}{a-1}\left[\ln\left(\frac{a \cdot V_{max}}{V_{th}} - 1\right)\right] \tag{4.6}$$

where a is a coefficient resulting from the Taylor approximation for t_2 (around t_2/τ).

The ToT time is then defined as:

$$ToT = t_2 - t_1 \tag{4.7}$$

When the peak voltage (V_{max}) of the CSA output is slightly higher than the

threshold voltage (V_{th}), the terms involving the ratio of these voltages approach unity. In this regime, the time-over-threshold duration (t_2 - t_1) will be small and exhibit a non-linear relationship with V_{max}. This behavior is expected, as the CSA output remains above the threshold for only a brief period when its peak is marginally higher than the threshold. Conversely, when V_{max} significantly exceeds V_{th}, the term V_{th}/V_{max} becomes negligible, while V_{max}/V_{th} grows substantially. As V_{max} increases further, t_1 becomes insignificant compared to t_2. Consequently, the overall behavior of the time-over-threshold duration transitions from a non-linear regime near V_{th} to a more linear behavior as V_{max} significantly exceeds V_{th}. In this latter regime, the ToT duration primarily reflects the logarithmic behavior of t_2 and exhibits an approximately linear relationship with the logarithm of V_{max}. This inherent non-linearity poses a challenge when utilizing the time-over-threshold technique for energy measurements in EMPADs.

Figure 4.6 presents the results of *PSpice* [2] simulations exploring the relationship between electron energy, CSA output voltage, and ToT in a silicon pixel detector. As expected, in Figure 4.6(b), the peak output voltage (V_{max}) increases with higher electron energy, reflecting a higher charge deposition. Furthermore, Figure 4.6 (b) demonstrates the simulated ToT as a function of electron energy for the same pixel configuration, but at different threshold voltage differences (ΔV_{th}). As the electron energy increases, the ToT also increases, but the rate of increase diminishes, leading to a plateau at higher energies. Furthermore, increasing the threshold voltage difference decreases ToT for a given energy, demonstrating the impact of threshold selection on energy discrimination.

Calibration Procedures for ToT-based Energy Measurements

Several calibration methods, including the surrogate function modeling, are applied to achieve precise energy measurement throughout the detector's dynamic range. In certain situations, other digital processing strategies, like look-up tables, might be needed to support these calibration efforts [145]. The calibration process for ToT-based energy measurements can be quite intricate and time-consuming. For instance, in the TimePix detector, each pixel's energy response is characterized by a non-linear surrogate function with four parameters, requiring measurements at multiple calibration points [142].

[2] PSpice is a simulation program used for emulating the electrical behavior of electronic circuits. It helps engineers test and validate circuit designs before physical implementation.

[3] Simulations emulate an electron colliding with the detector as charge injection into a 55×55 μm^2 CMOS technology diode, using a capacitor C set to a corresponding voltage V of value $Q = CV$ and a behavioral model for the CSA and discriminators.

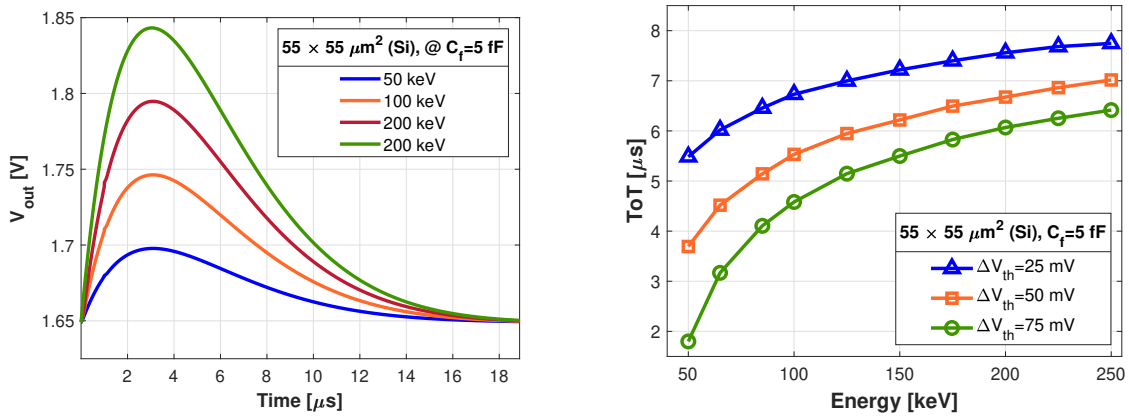

(a) (b)

Figure 4.6: *Pspice* simulations[3] results for a 55×55 μm^2 silicon pixel and $C_f = 5$ fF: (a) CSA output voltage (V_{out}) as a function of time for different energies (50,100, 200 and 250 keV), and (b) ToT as a function of electron energy at different threshold voltage differences (ΔV_{th}).

This process is further complicated by the Gaussian distribution of ToT values for each pixel and hit, making calibration a demanding task.

Although calibrating with gamma radiation sources provides high precision, it requires extensive measurements with multiple sources and intricate data analysis [142]. Alternatively, test pulse calibration strategies, as proposed in [146], enable recalibration without needing a radiation source, even when physical access is limited. However, the inherent non-linearity, particularly pronounced at low energies, can reduce the accuracy of ToT-based EELS measurements in SEM, necessitating further advancements in calibration techniques or alternative readout methods.

As illustrated in Figure 4.7, the ToT exhibits a complex, non-linear dependence on energy, particularly at lower energies. A surrogate function approach is employed to model this behavior accurately. This function, represented by the equation in the image, effectively captures the relationship between ToT and energy, incorporating four key parameters: a, b, c, and t. Each detector pixel requires specific parameters for the calibration surrogate function. These parameters can be determined carefully for every pixel, creating four parameter sets to calibrate the detector array fully. Each pixel is individually exposed to a monoenergetic radiation source to ensure accurate and tailored calibration.

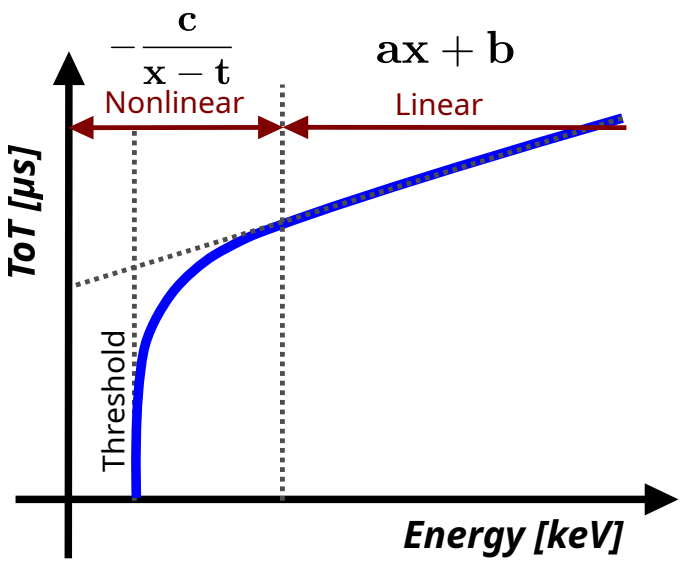

Figure 4.7: Surrogate Function Modeling of ToT-Energy Relationship.

4.3. Stacked Diodes for Electron Energy Discrimination

This biomimetic approach seeks to emulate the eye's ability to distinguish between different wavelengths of light by utilizing how photons are absorbed at varying depths in silicon. Beyond the initial trichromatic processing, the brain uses opponent channels to enhance color discrimination. These channels process signals in opposing pairs: red-green, blue-yellow, and black-white to contribute to the perception of color contrasts [147].

Inspired by similar techniques in CMOS image sensors, this design enhances sensitivity and color detection [102, 136]. Conversely, Bayer filters are commonly used in color cameras due to their simplicity and cost-effectiveness. They provide a reasonable compromise between color information and spatial resolution. However, this approach inherently sacrifices some resolution as each pixel can only capture one color, requiring interpolation to reconstruct a full-color image. In contrast, stacked diode CMOS sensors for particle detection (or visible light) offer a further advantage: the same electron (photon) can differentiate colors (spectra) regardless of its hitting position, enabling both spectral and spatial information to be extracted simultaneously without compromising resolution.

This capability allows a single electron (or photon) to be split into three or more components, improving both resolution and sensitivity. The principle of using stacked

diodes for light wavelength detection on visible and infrared bands was already patented in the 80s [148].

Consequently, this technique was further developed and transformed into a trichromatic visual sensor that was ultimately brought to market as a commercial product by Foveon (Acquired by Sigma Corporation) [149]. This concept is applied here to detect electrons across various energies used in SEM applications. By stacking multiple diodes vertically, the detector can effectively capture and convert electrons of different energies into electrical signals, thereby enhancing overall sensitivity and allowing energy discrimination, essential for differentiating between electrons of varying energies in SEM imaging.

4.3.1 Matrix Design

Figure 4.8 shows a block diagram of a stacked diode-based Active Pixel Sensor (APS) matrix integrated with an analog-to-digital converter (ADC) and associated readout circuitry, forming the proposed EMPAD. A 3T Active Pixel Sensor (APS) [4] is used for sensing the signals coming from the diodes. It is named active because it uses a MOS transistor in a source follower configuration. Modern smartphone cameras are mainly based on APS architecture to acquire images due to their flexibility, versatility, and easy implementation in standard CMOS processes.

The APS matrix consists of 44 rows (numbered from 0 to 43) and 64 columns (numbered from 0 to 63) of pixels. Each pixel is equipped with three stacked diodes (D1, D2, D3) and their respective control signals (*RST_ROW*, *SR_D1*, *SR_D2*, and *SR_D3*). In addition, they are supplied by three different DC voltages: V_{DD}, V_P, and V_N. The first one is used as a general supply, while V_P and V_N are used to set the operating voltages of the diodes. The *RST_ROW* signals reset the pixels, preparing them for charge collection. During the exposure time (T_{exp}), incident electrons generate charge in the diodes. Once the charges are collected, the signals *SR_D1*, *SR_D2*, and *SR_D3* manage the readout from each diode layer within the pixel.

Column select signals (*COL*) sequentially activate the readout of each column. The ADC converts the analog signals from the pixels into digital values using a ramp comparison technique, one row at a time. Each ramp produces 64 (8-bit) words ap-

[4] 3T-APS utilizes three transistors per pixel for its readout and control circuitry. It offers advantages in terms of reduced noise and improved signal integrity compared to other APS architectures.

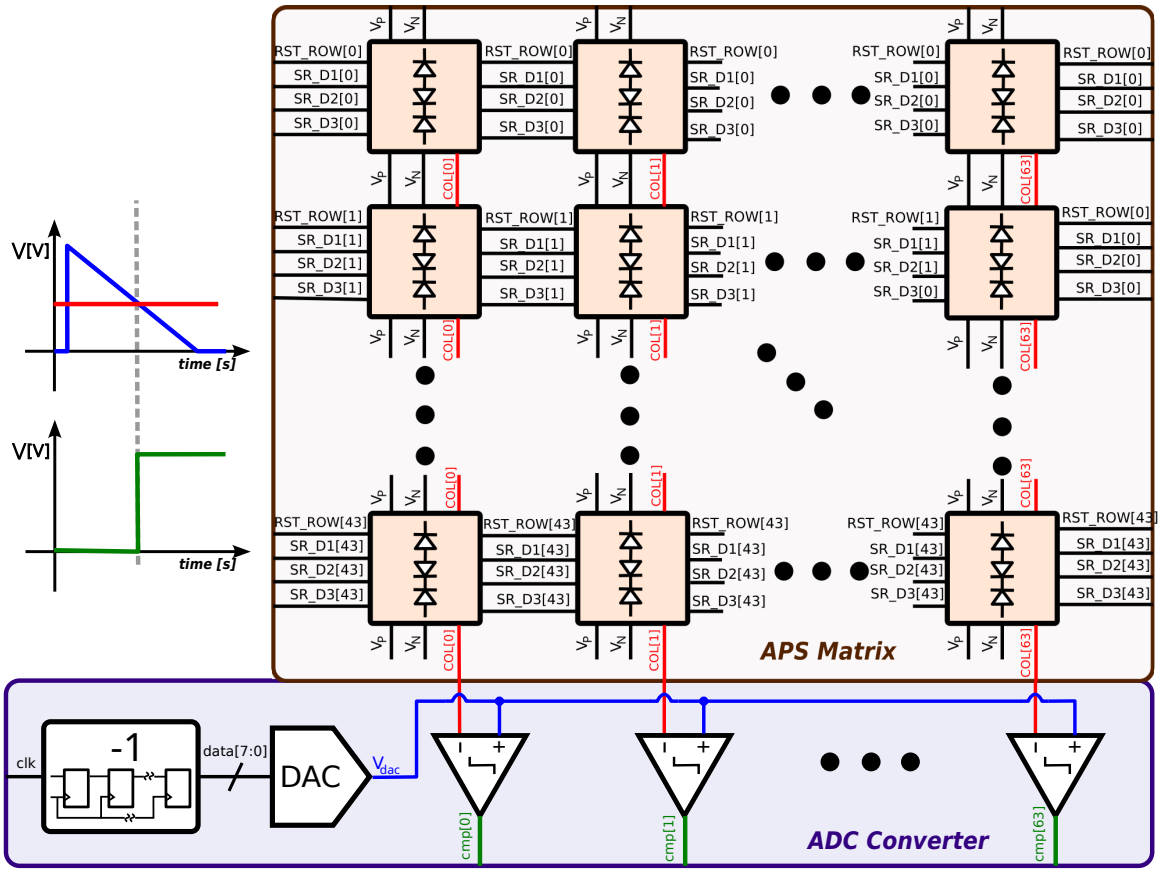

Figure 4.8: Pixel connections for the proposed APS-based matrix using stacked diodes, row-by-row readout, and a 8-bit ADC ramp converter for signal acquisition.

proximately every 256 clock cycles, with each word representing the converted value of a corresponding diode. Multiple comparators compare V_{dac} with signals from the APS matrix columns ($COL[0]$ to $COL[63]$), generating the outputs $cmp[0]$ to $cmp[63]$ based on the column values. The converted data is immediately transferred to the SRAM [5], which remains there until the next exposure time, T_{exp}. If not transferred, this data will be overwritten by the next sequence of bits (next row). The stored data is then shifted out serially for further processing or storage.

Figure 4.9 shows the prototype layout of the die designed with UMC L180 MM/RF technology, with each block highlighted and labeled. Table 4.1 provides a detailed layout area report, listing the main components of the IC die. The rectangular structures encircling the central rectangle are the input/output (I/O) cells, each consisting of a square-shaped PAD and associated interface and ESD protection circuitry. The PADs are connected to solder bumps in the IC package to give external

[5]SRAM stands for Static Random-Access Memory. It is a type of semiconductor memory that retains data bits in its memory as long as power is being supplied.

connectivity. The red squares in the Layout indicate diffusions; in the matrix region, they represent the pixel's sensing area. The blue shapes represent the polysilicon layers that form the MOS gates and some resistors. The lines extending from the chip depict the metal traces. We mainly used the lower metals Metal1 and Metal2 for supply and ground connections. Metal 3 up to Metal 5 were primarily dedicated for signal routing. The comparators are located directly beneath the pixels. The level shifters (LS) are to the right of the matrix, and a portion of the ADC converter is visible in the lower-left corner. The analog blocks are powered by 3.3 V, and the digital blocks (APS controller and SRAM memory) are powered by 1.8 V. Using multiple supply and ground pin connections, one for digital and two for analog, enhances signal integrity by reducing noise coupling and interference between the various sections of the IC.

This circuit was developed using the *Cadence Virtuoso®* [6] design tools in collaboration with the Instituto de Microelectrónica de Sevilla (IMSE) [7]. The IC development process took 14 months, from initial conception through design and validation. The process involved simulations under various Process, Voltage, and Temperature (PVT) conditions following industrial practices to ensure high yield.

The final GDSII [8] Layout of the EMPAD IC and the other test structures mentioned in this work was submitted to UMC (Taiwan) for fabrication in May 2022. Due to the complexities of the chip fabrication process, the additional time required for packaging and bounding connections, and shipment delays, the prototyped ICs were received in December 2022. This IC contains approximately $120,000$ transistors, among other components like integrated diodes, resistors, and capacitors. The significant lead time underscores the importance of careful planning and verification in IC design to minimize the risk of costly and time-consuming re-spins.

[6] *Cadence Virtuoso®* is a comprehensive software suite used for designing, simulating, and verifying analog, digital, and mixed-signal integrated circuits (ICs).

[7] The Instituto de Microelectrónica de Sevilla (IMSE) is a prominent research center focused on design microelectronics and semiconductor technology in Spain

[8] The term GDSII refers to a file format commonly used in the semiconductor industry for designing ICs.

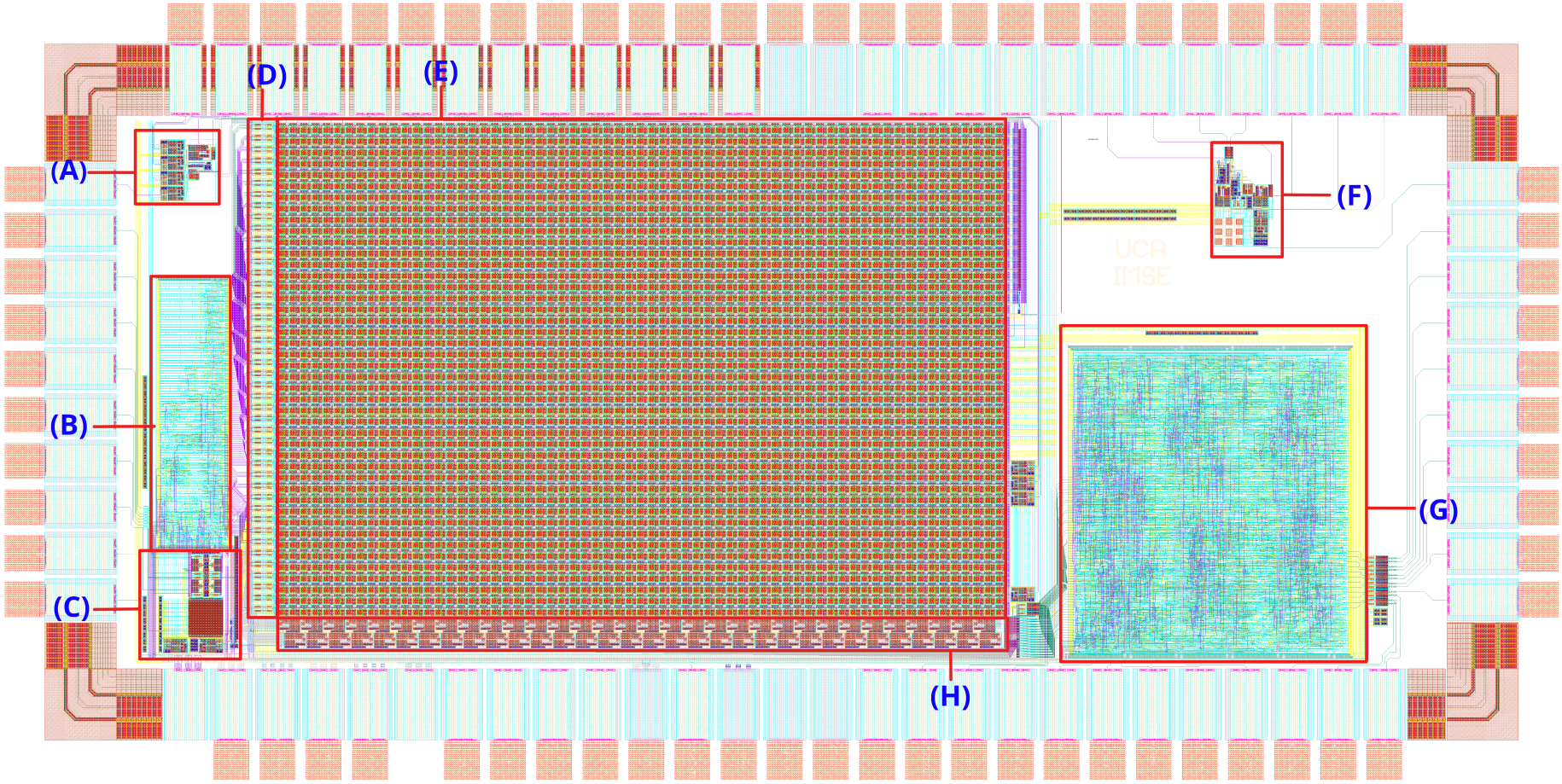

Figure 4.9: Layout of the integrated circuit (IC) highlighting the differentiation of blocks and implemented using 0.18 μm UMC technology.

Table 4.1. *Layout area summary for the key components of the prototyped IC.*

Label	**Block**	**Area**
(A)	Single stacked pixel	101 $\mu m \times 120.5\ \mu m$
(B)	APS digital control	145 $\mu m \times 534.8\ \mu m$
(C)	8-bits ADC	140.7 $\mu m \times 203\ \mu m$
(D)	Level Shifters (LS)	49.5 $\mu m \times 974.6\ \mu m$
(E)	64×44 APS matrix	1440 $\mu m \times 970\ \mu m$
(F)	CAP TOP (single pixel)	114 $\mu m \times 168\ \mu m$
(G)	3 channels SRAM memory	582 $\mu m \times 612\ \mu m$
(H)	Comparators	1440 $\mu m \times 61.9\ \mu m$
Total IC area:		3046 $\mu m \times 1520\ \mu m$

8-bit Ramp ADC with 30 ksps[9] Sampling Rate

An internal 8-bit ramp Analog-to-Digital Converter (ADC) is one of the most critical blocks in the design and digitizes the signals from the diodes for data acquisition. The R-2R topology was selected due to its inherent advantages in reduced component count. It requires fewer switches and resistors than other DAC architectures (e.g., resistive dividers). This compactness is essential to minimizing the overall area and interfacing complexity, particularly considering the additional Level Shifters (LS) requirement for each digital signal. A resistive divider instead of a ladder R-2R using an X-Y addressing scheme would represent the use of at least $2 \cdot 2^{N_{bits}/2}$ switches and hence LSs [150], increasing the area dramatically.

Moreover, the output generated by an R-2R ladder working in voltage mode is inappropriate for direct use as it requires a high-impedance buffer or amplifier for accurate voltage measurement and a low-output impedance stage to drive the DAC load effectively [151]. The R-2R ladder network has a known drawback: it can exhibit non-monotonic input-output behavior when slight mismatches in resistor values [150]. This behavior can occasionally cause the output voltage to drop, even as the digital input increases. However, in the EMPAD system context, this non-monotonic behavior is unlikely to significantly affect the overall image quality, as the introduced errors are usually minor and may go unnoticed. Each pair of ladder resistors, corresponding to each bit, was carefully matched in the Layout to reduce inter-device process variations, and dummy devices were added around them to mitigate etching effects further.

[9] ksps stands for kilo-samples per second, indicating the sampling rate of the ADC. In this case, 30 ksps means the ADC can convert 30,000 analog samples into digital values per second.

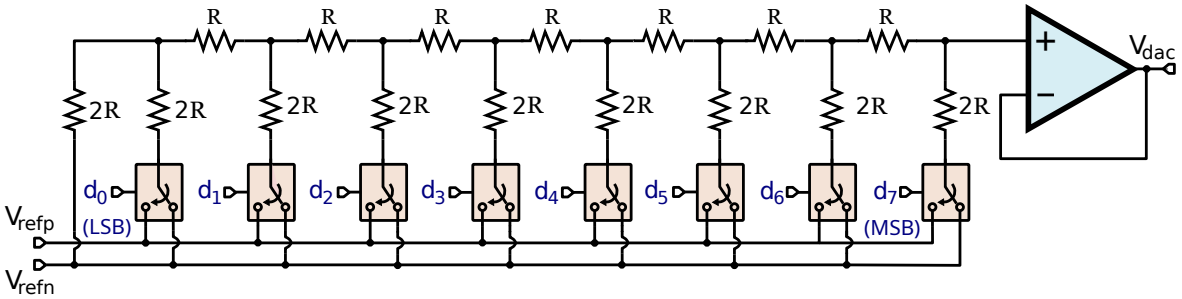

Figure 4.10: R-2R ladder digital-to-analog converter (DAC) using along the comparators to create the ADC ($R = 42.3$ kΩ).

4.3.2 Testing and Evaluation

Figure 4.11 provides an overview of the test setup used to evaluate the functionality and performance of the fabricated IC. The setup consists of several key components, each crucial for acquiring, processing, and analyzing data from the stacked diode EMPAD.

At the core of the setup is the IC, which includes the stacked diode array, APS digital control and clock/reset generation circuits, an 8-bit ramp ADC, SRAM for temporary data storage, and test circuitry with buffers. Support circuitry is essential for the diode array's operation and data readout. The 'Bias Distribution' block provides the necessary current to the APS pixels. The 'APS Digital Control & Clock/Reset Generation' block manages the timing and control signals to configure the exposure and reset times. The 'Test Circuitry & Buffers' are used for on-chip diagnostics and to condition the signals. As mentioned, generated digital data is temporarily stored in an on-chip SRAM before being sent off the chip. The communication interface can transmit up to 45 Mbits/s.

The communication bridge is an OpalKelly board (XEM 7310MT) equipped with an Artix 7 FPGA, which enables fast data transfer to an external system and handles some critical processing and control functions. The FPGA also handles critical processing and control functions, such as:

1. Generate precise and user-defined clock periods and control signals.

2. Managing the timing and synchronization of requests to prevent data loss from overwriting on-chip SRAM during each frame cycle.

3. FPGA system enables the acquisition of debug signals and the control of peripheral devices such as DACs and ADCs, facilitating the setting and measurement of

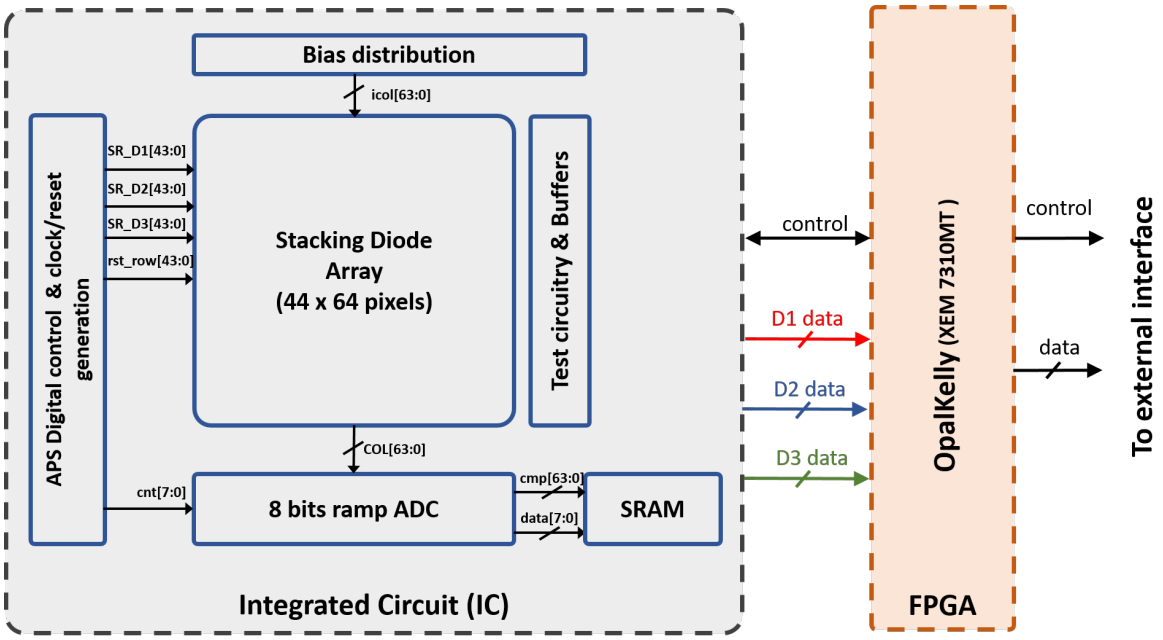

Figure 4.11: System-level implementation of an EMPAD that utilizes stacked diodes fabricated in CMOS technology for spectral resolution.

voltage signals. For instance, V_P, V_N, and V_{top} voltages can be adjusted through the test interface and transferred to their corresponding DACs for precise control.

The control logic for this implementation was designed using *Verilog*[10] and synthesized in *Vivado*[11].

Figure 4.12(a) shows the encapsulated chip in a CPGA100S ceramic package alongside a 2-cent euro coin, illustrating the chip's compact size. The IC is securely housed in this 100-pin ceramic package, which provides the necessary connections for testing and integration and ensures effective thermal dissipation. Figure 4.12(b) displays the PCB used to test the chip, including an FPGA board for control and data acquisition. The FPGA is mechanically and electrically connected to the PCB via a Samtec connector underneath, eliminating the need for cables and ensuring a stable, high-speed connection. The PCB also incorporates essential components such as ADCs, DACs, and voltage regulators, which are crucial for interfacing with the chip and enabling efficient testing. Table 4.2 lists the references and descriptions of the commercial components used in the PCB to test the prototyped IC.

[10]Verilog is a hardware description language (HDL) used to model and design digital systems, such as the FPGA or IC.

[11]Vivado is a software suite developed by Xilinx for the design and implementation of digital circuits on FPGAs and other programmable logic devices.

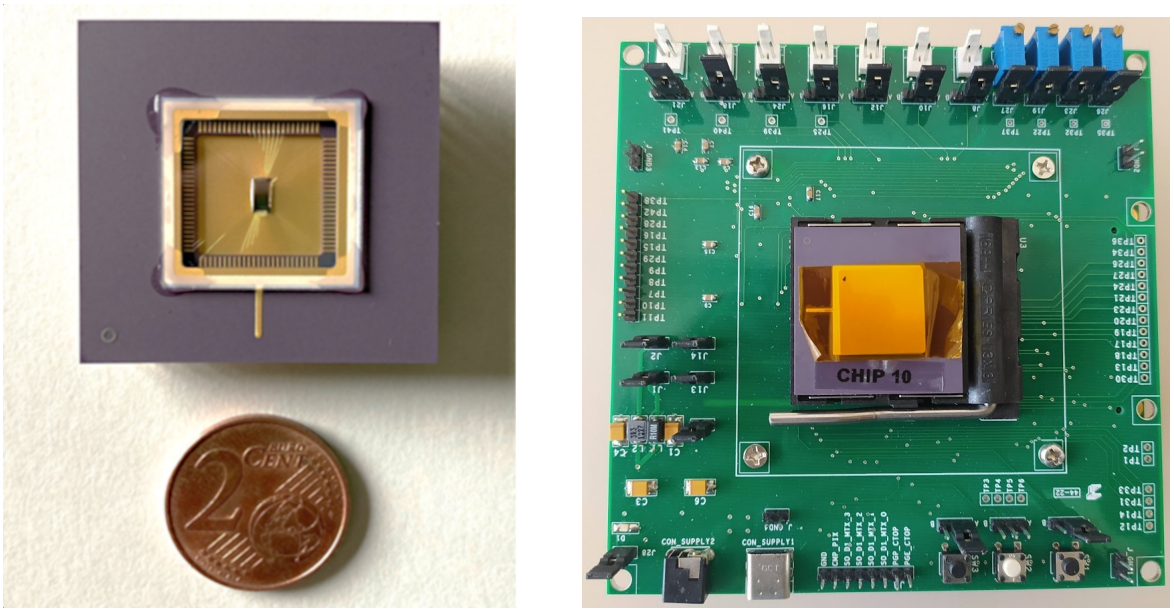

(a) (b)

Figure 4.12: (a) Comparative size of the encapsulated chip in a PGA Ceramic package with a 2-cent coin. (b) The PCB tests the chip, incorporating an FPGA board for control, data acquisition, and essential components like ADC, DAC, and voltage regulators.

Figure in 4.13 shows a Python-based Graphical User Interface (GUI) developed to control the APS matrix for the EMPAD system using the Opal Kelly board. It was developed using the package *PyGUI*. This interface allows u çsers to adjust critical parameters, such as the voltages applied to the sensor (V_P, V_N and V_{TOP}), the exposure and reset times (T_{exp} and T_{rst}), and the number of frames captured for video. These settings enable precise control over the matrix's behavior to optimize performance for different conditions (illumination and beam exposition). The tool provides the option to save the output in various formats. Images can be saved as PNG files, suitable for web and general use, or as numerical RGB vectors. Additionally, the output can be saved as an MP4 video to demonstrate dynamic content and record real-time interactions.

Figure 4.14 compares two images: (a) a photograph captured by a commercial cellphone camera and (b) an image acquired using our proposed EMPAD detector. The EMPAD image was processed with standard color calibration, which requires further refinement. The image of the air duct, captured by the designed CMOS Image Sensor (CIS), shows precise details and good contrast despite the sensor's limited resolution. These results indicate that the CIS can effectively capture essential features even with moderate resolution. Thermal effects within the chip mainly cause the lower patch to

Table 4.2. *List of the commercial IC components used in the PCB.*

Component	Reference	Description
ADC	TI ADC78H90	8-Channel, 500 kSPS, 12-Bit A/D Converter
DAC	TI DAC124S085	12-Bit QUAD DAC with Rail-to-Rail Output
Digital Buffers	TI SN74LVCZ244A	Octal Buffer/Driver with 3-State Outputs
OPAMP	TI OPA388ID	Precision, Zero-Drift, Zero-Crossover, True Rail-to-Rail, Input/Output OPAMP
FPGA	Artix-7	Low-Power FPGA designed by Xilinx

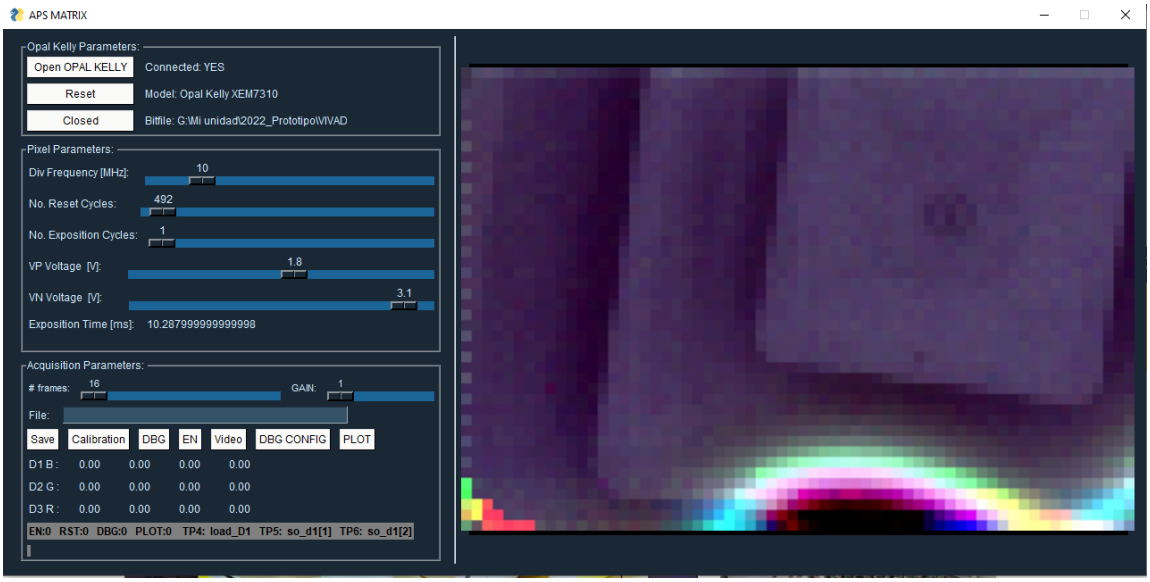

Figure 4.13: Python interface for controlling the APS matrix with adjustable settings for voltage, exposure time, and frame capture.

be seen in the acquired image (Figure 4.14) (b). The absence of a level shifter in the comparator block is causing an increased supply current, which leads to localized self-heating in this region and creates a thermal pattern (rounded shape). Other effects around the borders can be attributed to noise and coupling from adjacent pixels or blocks (for example, the differences in color in left border pixels) and can be mitigated by increasing the width and composition of the guard rings [152].

Thermal gradients across the chip can significantly affect its performance, leading to uneven signal responses. When certain areas of the chip become warmer than others (often due to factors such as high current passing through a short metal wire), localized hot spots can develop. These hot spots alter the electrical properties of the affected

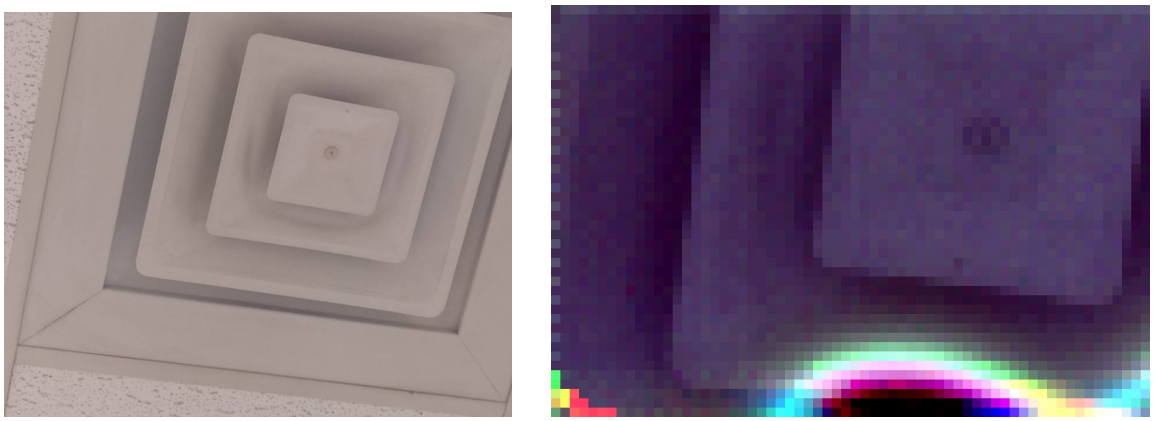

(a) (b)

Figure 4.14: Comparison of (a) an image captured by a Redmi Note 13 cellphone and (b) an image acquired by the proposed EMPAD and affected by thermal gradients.

regions (i.e., leakage currents or threshold voltages), resulting in darker spots or patches in the image output [153, 154]. Proper management of thermal distribution is essential to maintain consistent image quality and ensure the detector's reliability.

Reducing the current consumption of surrounding blocks, such as the comparator block, could help decrease overall power dissipation and heat generation near the pixel matrix. Another practical approach is reinforcing the guard rings that provide electrical and thermal isolation between the photodiodes and the surrounding circuitry. These guard rings act as barriers, preventing leakage currents and heat transfer between different regions of the chip. Strengthening these guard rings can minimize thermal coupling between the photodiodes and the heat-generating circuitry, resulting in a more uniform temperature distribution across the pixel matrix.

4.3.3 Pixel Design and Layout

We implemented the triple-stacked photodiode APS pixel in a standard UMC 180 nm technology. As depicted in Figure 4.15, the initial pn-junction consists of a heavily doped n+ implant within a lightly doped p-well. A second p-n junction is established between the p-well and the deep n-well, while a third p-n junction is formed between the deep nwell and the p-substrate. A metal top is also placed above the circuitry to prevent the light and ionizing particles from generating undesirable electrical effects like electron-hole pair generation or oxide-trapped charges. This metal is also externally controlled by a voltage V_{top}, which adjusts the electric field surrounding the pixel and may have favorable results in deflecting or attracting the particles to the sensitive area

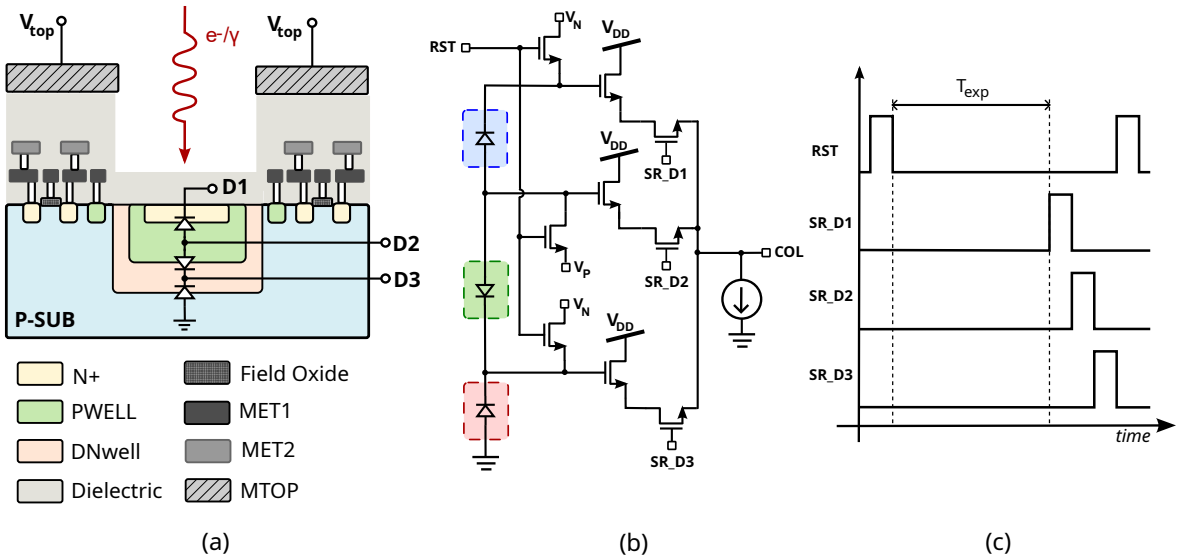

Figure 4.15: (a) Transversal view of a single pixel highlights the different junctions and the placement of the top metal. (b) APS pixel structure proposed in [131]. (c) Timing diagram used in the measurements. Exposure times are adjusted based on the light or beam intensity.

of the pixel.

The pixel circuit corresponds to a 3T-APS with three different RGB extraction channels, as proposed by Foveon [131]. The benefit of this circuit is its easy implementation on the Layout by utilizing only 3.3 V standard NMOS transistors, avoiding further process variations from different components and reducing leakage.

Initially, all diodes are set to V_P or V_N, corresponding to the p-well and deep-well bias voltages, respectively. We use $V_N = (2/3)V_{DD}$ and $V_P = (1/3)V_{DD}$ with $V_{DD} = 3.3\,V$ to prevent forward bias junction and ensure a symmetric signal excursion. Despite the higher sensitivity of triple junction photodiodes compared to single junction photodiodes, the latter has a broader signal excursion. Control signals SR_D1, SR_D2, and SR_D3 are activated after an exposure time T_{exp} to perform a non-destructive read of the junction voltages. Additional readings can be performed depending on the signal strength (i.e., light intensity or energy particles) until a new reset cycle is conducted.

Figure 4.16 shows a microphotography of a single test pixel for the 3T APS configuration. It was fabricated using the standard 0.18 µm UMC technology. The pixel size is 22.08 μm × 22.08 μm with a fill factor of 45%. Due to design rule restrictions and contact placement limitations, the photodiodes are not equally sized in the stacked configuration, with the deeper photodiode being the largest. Self-biased

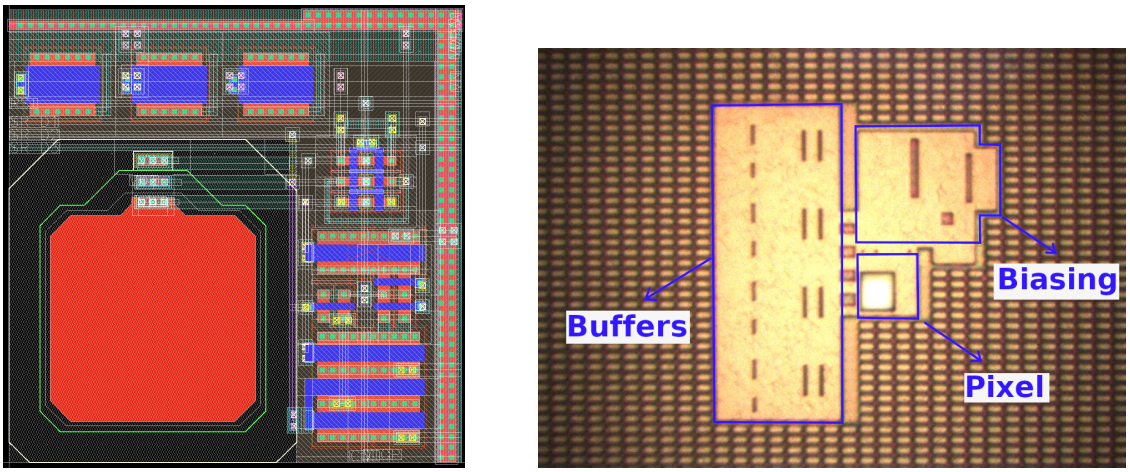

(a) (b)

Figure 4.16: (a) Layout of the stacked diodes and the pixel's circuitry. (b) Light micrograph of the fabricated die, highlighting the single-pixel test structure. Dimensions for the diodes, D1: 10.44 μm × 10.44 μm, D2: 11 μm × 11 μm and D3: 14 μm × 14μm. Dimensions for the test circuits, buffers: 47.5 μm × 120 μm and biasing: 55 μm × 38 μm.

buffers were utilized to ensure the observability of the junction and column voltages. Voltages from the PADs were measured using a 12-bit external ADC converter. At least Metal 6 (Top Metal) covered all surrounding analog circuits.

4.3.4 Stacked diodes evaluation

Color Extraction

Given that junction depths in standard CMOS processes are fixed, the light responses for Red (R), Green (G), and Blue (B) colors as shown in Figure 4.2 and based on absorption depth, do not precisely correspond to the physical depths of diodes D1, D2, or D3. It means that the sensitivity of each diode spans a range of wavelengths rather than being limited to a single color component. As a result, the voltage difference produced in an exposure time T_{exp} or voltage slope for each diode (ΔS_{D12}, ΔS_{D32} and ΔS_{D3}) includes contributions from multiple color wavelengths. This relation can be mathematically expressed as:

$$\begin{bmatrix} \Delta S_{D12} \\ \Delta S_{D32} \\ \Delta S_{D3} \end{bmatrix} = \begin{bmatrix} \alpha_1 \cdot K_{B_1} & \alpha_1 \cdot K_{G_1} & \alpha_1 \cdot K_{R_1} \\ \alpha_2 \cdot K_{B_2} & \alpha_2 \cdot K_{G_2} & \alpha_2 \cdot K_{R_2} \\ \alpha_3 \cdot K_{B_3} & \alpha_3 \cdot K_{G_3} & \alpha_3 \cdot K_{R_3} \end{bmatrix} \begin{bmatrix} B \\ G \\ R \end{bmatrix} \tag{4.8}$$

where K_{Bj}, K_{Gj} and K_{Rj} are dimensionless constants between 0 and 1 representing the percentage of blue, green, and red components, respectively, and α_j is the coefficient of the j-th junction, given by:

$$\alpha_j(\lambda) = \frac{1}{A_j \cdot [1 - r(\lambda)] \cdot P(\lambda)} \tag{4.9}$$

In this equation, P denotes the light's power per unit of area in $\mathrm{W/m^2}$, r is the silicon's reflectivity as a function of the wavelength (λ), and A_j is the area of the j-th diode. The mean values for the diode coefficients across the analyzed spectrum are $\alpha_1 = 19.1 \times 10^{-3}$ $\mu\mathrm{m}^2/(\mathrm{W/m}^2)$, $\alpha_2 = 17.2 \times 10^{-3}$ $\mu\mathrm{m}^2/(\mathrm{W/m}^2)$, and $\alpha_3 = 10.6 \times 10^{-3}$ $\mu\mathrm{m}^2/(\mathrm{W/m}^2)$. The optical properties of the silicon (i.e., reflectivity and absorption depths) were extracted from [155, 156].

In the 0.18 μm UMC process, it has been observed that not all colors affect all stacked diodes. For example, D2 is most sensitive to green light but also responds to blue light to some extent. Similarly, D3, primarily responsive to near-infrared (NIR) light, also shows sensitivity to red light and, to a lesser degree, to green light. In that way, (4.8) can be re-defined as:

$$\begin{aligned}
\Delta S_{D12} &\approx B \cdot \alpha_1 \cdot K_{B_1} + G \cdot \alpha_1 \cdot K_{G_1} \\
\Delta S_{D32} &\approx B \cdot \alpha_2 \cdot K_{B_2} + G \cdot \alpha_2 \cdot K_{G_2} \\
\Delta S_{D3} &\approx G \cdot \alpha_3 \cdot K_{G_3} + R \cdot \alpha_3 \cdot K_{R_3}
\end{aligned} \tag{4.10}$$

These findings indicate the need for a color correction algorithm to precisely separate and extract the individual color components from the raw diode signals. Essentially, this process is a form of color correction or spectral decomposition. This procedure is done by reducing the total squared differences between the measured voltage slopes (ΔS_{D12}, ΔS_{32} and ΔS_{D3}) and those predicted by the model while keeping certain constraints on the constants. Mathematically, this optimization problem can be formulated as follows:

$$
\begin{aligned}
&\underset{K_{B1},K_{G1},K_{B2},K_{G2},K_{G3},K_{R2}}{\text{minimize:}} \\
&\quad \big[(\Delta S_{D12} - B_F \cdot \alpha_1 \cdot K_{B1} - G_F \cdot \alpha_1 \cdot K_{G1})^2 \\
&\quad + (\Delta S_{D32} - B_F \cdot \alpha_2 \cdot K_{B2} - G_F \cdot \alpha_2 \cdot K_{G2})^2 \\
&\quad + (\Delta S_{D3} - G_F \cdot \alpha_3 \cdot K_{G3} - R_F \cdot \alpha_3 \cdot K_{R2})^2\big] \\
&\text{subject to:} \\
&\quad 0 \leq K_{B1} \leq 1, \quad K_{B2} = 1 - K_{B1}, \\
&\quad 0 \leq K_{G1} \leq 1, \quad 0 \leq K_{G2} \leq 1, \\
&\quad 0 \leq K_{G3} \leq 1, \quad K_{G1} + K_{G2} + K_{G3} = 1 \\
&\quad 0 \leq K_{R3} \leq 1.
\end{aligned}
\tag{4.11}
$$

where B_F, G_F, and R_F are the filtering functions for blue, green, and red wavelengths, respectively. These wavelength-dependent functions are defined as 1 for their respective color wavelengths and 0 otherwise. By solving this optimization problem, we can obtain the optimal values for the coefficients K_{B1}, K_{B2}, K_{G1}, K_{G2}, K_{G3}, and K_{R2}. The same principle, along with the electron beam sensitivities of each diode, can be used to extract the coefficients dependent on the different energies.

Light Sensitivity and Selectivity

Figure 4.17 shows the experimental setup for light responsivity measurements. The light source was a QTH Newport Halogen lamp connected to an Oriel Cornerstone 130 Monochromator. Due to the monochromator and the light source's non-uniform response, a Newport 1930-C light power meter is used to measure light intensity. A beam splitter is used to split the light beam equally into two parts, one for the chip and the other for the power meter.

All photodiodes were subjected to constant temperature during the experiments, while the narrow filter of the monochromator was varied in 10 nm steps. Silicon reflection values were not directly measured but were obtained from available reference tables [155, 156]. Since the power per unit area generated by the monochromator varies with wavelength, the sensitivity values must be normalized accordingly. Furthermore, due to design rule constraints verified by a Design Rule Checker (DRC) tool [12], the

[12]The Design Rule Checker (DRC) tool ensures that design specifications are met by verifying that all layout rules are adhered to, which helps in maintaining the integrity and functionality of the design

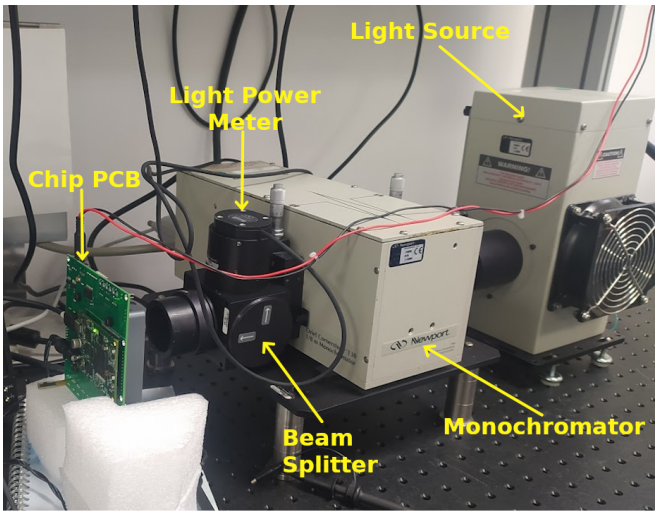

Figure 4.17: Experimental setup to characterize the photodiodes. A GPIB interface automatically controlled the Monochromator and light power meter using *MATLAB®*.

bottom, middle, and top diodes have different areas. Therefore, sensitivity values must also be normalized to the area. Figure 4.18 shows the sensitivity curves of all three photodiodes as a function of light wavelength. Diode sensitivities were estimated by measuring the time required by each photodiode to discharge its integration capacitance. The higher sensitivity of the top junction can be observed for shorter wavelengths (i.e., blue light), while the middle and bottom junctions show increased sensitivity to longer wavelengths. Notably, there is a remarkable sensitivity in the NIR band, as indicated by D3. The top photodiode primarily detects the blue component (B), with a minor contribution from the green component (G) due to potential charge sharing or spectral overlap. The middle photodiode predominantly measures the green component (G) while also registering contributions from the blue (B) and red (R) components. The bottom photodiode primarily detects the NIR components, with additional sensitivity to the red component (R) and some contribution from the green component (G) [157]. Thus, to estimate the absolute diode current values, some data post-processing is required [158].

It was possible to determine the constants using the data obtained from Figure 4.18 and by solving the optimization problem described in (4.11). With these constants ($K_{B1} = 0.8$, $K_{B2} = 0.2$, $K_{G1} = 0.025$, $K_{G2} = 0.85$, $K_{G3} = 0.125$ and $K_{R3} = 0.7$) a new plot was generated, illustrating the sensitivity of each color component (B, G, R) as a function of light wavelength (Figure 4.19). As anticipated, each color component exhibits distinct peak sensitivities within specific wavelength ranges. Blue shows the

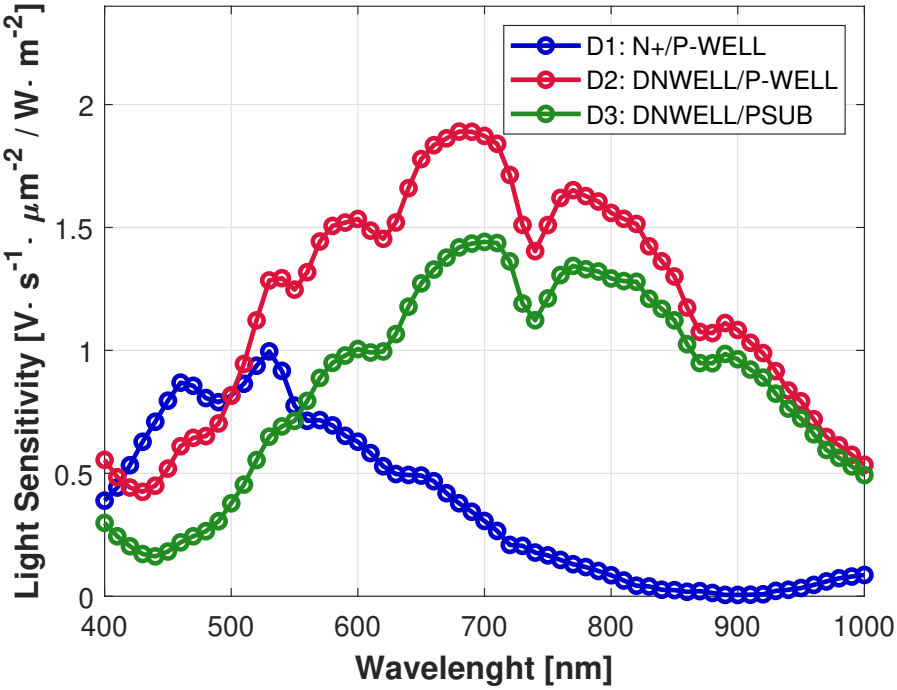

Figure 4.18: Photodiodes spectral sensitivity per unit of area vs. light wavelength. D3 shows a remarkable sensitivity in the NIR band.

highest sensitivity among the three spectral components, ranging from approximately 425 to 515 nm, corresponding to the shorter wavelength characteristic of blue light. Green peaks within the 515 to 660 nm range align with the visible spectrum's green portion. The red curve shows predominant sensitivity in the longer wavelength region, extending from 660 nm into the NIR region. This extended sensitivity into the NIR is a notable feature of the stacked diode design and may provide advantages in applications requiring the detection of both visible and NIR light.

The presence of unexpected peaks or valleys in the spectral sensitivity curve could indicate the influence of additional elements or layers on the silicon substrate in addition to the intended photodiode structure [159]. The passivation layer, typically composed of silicon dioxide or other dielectric materials and used as an insulator and passivation, exhibits a specific optical response that can affect light transmission to the underlying photodiodes. Here, it is pertinent to introduce the concept of external quantum efficiency (QE), which represents the fraction of incident electrons/photons converted into photocurrent, and dark current, which is the current that flows even without light or stimulus. External QE is influenced by internal QE, determined by the photodetector's geometry and doping, and optical efficiency (OE), accounting for

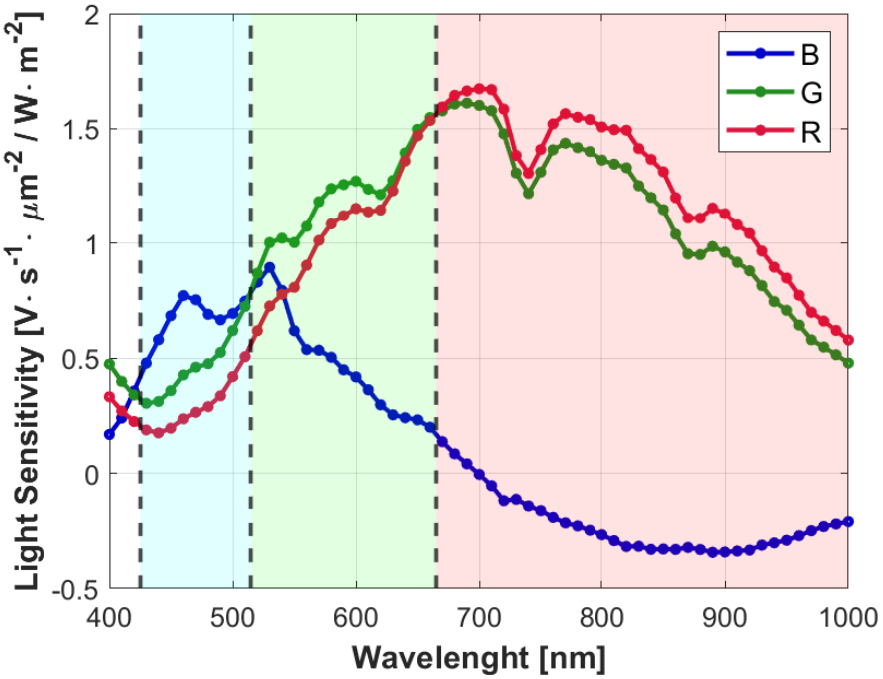

Figure 4.19: Light sensitivity of color components (B, G, R) extracted from stacked diode signals across different wavelengths.

Table 4.3. *Summary of electrical and light responsivities of three stacked diodes.*

Diodes	**Junction Depth** $[\mu m]$	λ_{max} $[nm]$	**Dark Signal Rate**[a13] $[V/s]$
D1	0.25	530	1.1
D2	1.2	680	0.2
D3	1.8	710	2.75
[a] Measured at $T = 25\ ^oC$ and for 11 μm $\times$ 11 μm pixel size.			

photon losses between the pixel surface and the photodetector [160]. Each additional layer above the photodiodes, intentional or unintentional, such as anti-reflective coatings or metal interconnects, can further modify the optical response, leading to deviations from the expected spectral sensitivity [161]. The design process of a pixel should involve the fabrication process, geometries, the composition of the various layers, and the electrical circuitry.

Table 4.3 summarizes the electrical and light responsivities obtained for the three junctions. Junctions' depths were inferred from the foundry documents. We have defined λ_{max} as the wavelength with the maximum sensitivity to the light. Proper color extraction requires all three signal components, even if only one color is extracted.

4.3.5 Electron beam sensitivity

We exposed a single pixel to varying direct electron beam current levels using a Tescan Vega 4 SEM Microscope. In the context of semiconductor detectors, the relationship between photodiode current I_{PD} and beam current I_{beam} is characterized by responsivity, which can be mathematically defined as:

$$R_M = \frac{I_{PD}}{I_{beam}(E/e)} \tag{4.12}$$

where E is the electron landing energy and e is the unit charge of the electron [162].

The pixel's sensitivity to different beam currents normalized to the current beam is shown in Figure 4.20. An electron beam with an energy of 10 keV was centered on the pixel photodiodes using a probe size diameter smaller than 10 nm. In contrast to light, the electron incidence in this experiment was punctual, making the incident power independent of the area. However, the diode's beam sensitivities ratio depends on the beam current value. Thus, it is possible to detect the beam current by processing the diode's responses.

Passivation and isolation layers, typically composed of SiO_2, are essential in energy-detecting pixels for structural integrity and component isolation. However, these layers limit electron detection capabilities. The Annex A provides cross-view images of the stacked diode pixel and various AFM topographical analyses, illustrating the metallization and isolation layers. The interaction of electrons with SiO_2 can lead to several undesirable effects. Firstly, electrons can be scattered or deflected by the insulator layer, altering their trajectories and potentially causing them to miss the intended detection region [163]. Secondly, electrons can lose a significant portion of their energy through inelastic collisions with the SiO_2 molecules, reducing their ability to generate electron-hole pairs in the active material. Lastly, electrons can become trapped within the oxide layer, diminishing the signal and contributing to noise. The cumulative impact of these effects is a reduction in the detector's overall electron collection efficiency. These phenomena can manifest as decreased sensitivity, reduced signal-to-noise ratio, and impaired energy resolution.

[13]Dark signal rate, or dark current rate, tracks the sensor's voltage change over time when no stimulus (i.e., light) is present. If photodiode-associated capacitance is unknown, dark current is calculated by measuring the voltage change rate (expressed in volts per second).

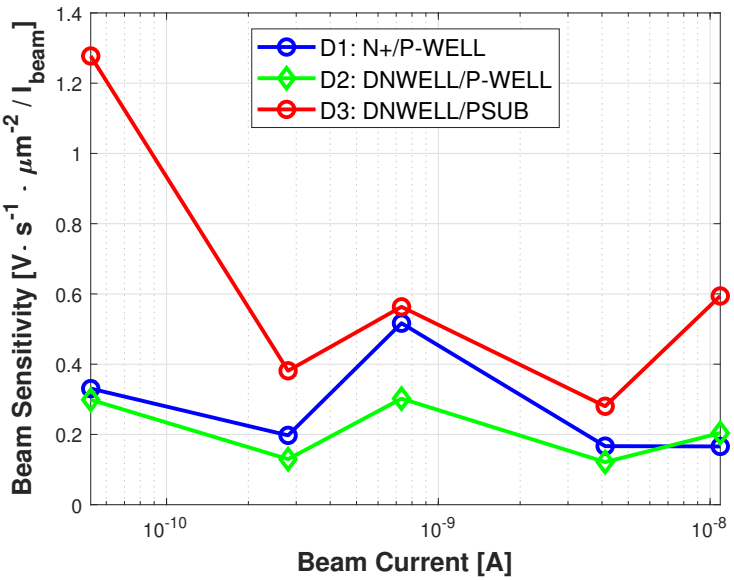

Figure 4.20: Photodiodes electron beam sensitivity per unit of area in function of beam current I_{beam}. The values were normalized to I_{beam} to assess the capability to distinguish between different current values.

In addition, temperature-related issues arising from the vacuum conditions in the SEM chamber and the heat dissipation of components on the PCB, such as the FPGA and regulators, can be mitigated through adequate thermal dissipation strategies, including the use of heat sinks, thermal pads, and active cooling systems. Nonetheless, further measurements are required in a more stable temperature environment to ensure accurate detection.

4.4. Neuromorphic ToT Measurement with Derivative Circuit

Neuromorphic vision sensors, such as the Dynamic Vision Sensor (DVS) [9], have attracted significant interest because they detect changes in a scene asynchronously, responding only to movement or variations in light (or stimulus). This selective response reduces data redundancy and power usage compared to traditional cameras, which capture entire frames continuously. However, DVS pixels typically only signal that a change in light has occurred without measuring the extent of that change. To address this limitation, DVS can be enhanced to capture additional information, such as ToT measurements, a technique commonly used in TimePix sensors to gauge the energy of incoming particles, the number of single particles, and the ToA [82].

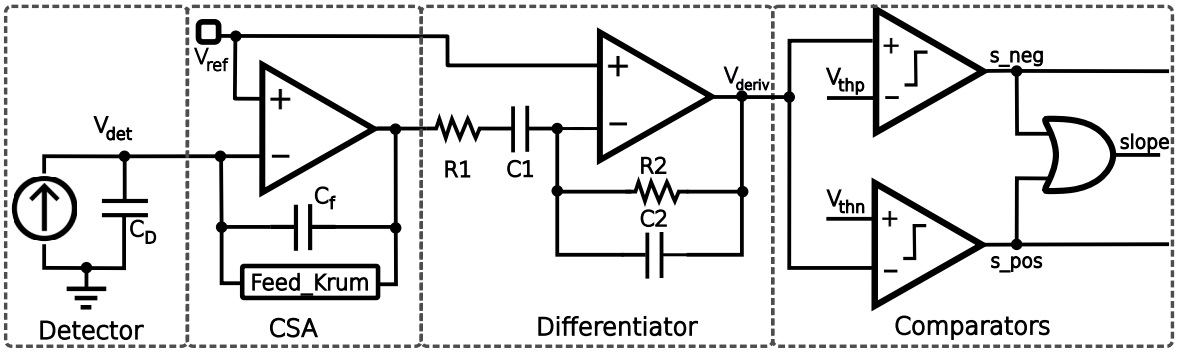

Figure 4.21: Derivative-Based DVS pixel for ToT Extraction

4.4.1 ToT DVS pixel

The transition to ToT-capable pixels involves adding circuitry to capture the temporal dynamics of pixel events, as shown in Figure 4.21. This setup includes a Charge Sensitive Amplifier (CSA), a differentiator stage, and comparators. The CSA converts the charge generated by the detector into a voltage signal, which is then passed through a differentiator circuit made up of resistors and capacitors or two capacitors (as shown in Figure 3.4) to generate a signal proportional to the rate of change in the input voltage.

This differentiated signal is compared against two thresholds using comparators, which generate digital pulses marking the start and end of events, thereby enabling Time-over-Threshold (ToT) measurement.

This derivative-based ToT measurement approach has several benefits. It utilizes the existing DVS pixel structure, requiring minimal modifications to add ToT functionality. The circuit operation is event-driven, consuming power only when a pixel event occurs, consistent with the low-power nature of neuromorphic systems. Additionally, ToT information enhances the sensor's capabilities, supporting tasks like object tracking, depth estimation, and scene segmentation.

Figure 4.22 illustrates the derivative-based and AER-compatible DVS pixel operation for ToT extraction. When an event occurs, such as an electron hitting the detector, the input voltage V_{in} rapidly increases according to equation (4.4). The differentiator picks up this change, generating a positive peak in V_{deriv}. When V_{deriv} surpasses the positive threshold V_{thp}, it triggers the p_{pos} signal, marking the start of the ToT measurement, or Time-of-Arrival (ToA) at t_1. As V_{in} decreases, V_{deriv} turns negative and crosses the negative threshold V_{thn}, activating p_{neg} and signaling the end of the event. The interval between p_{pos} and p_{neg} corresponds to the ToT, providing insights into

the intensity or duration of the detected event. The time resolution is determined by the clock period of the counter shown in Figure 4.4. Reducing this period can have the side effect of increasing power consumption and causing self-heating in the device. This method not only facilitates ToT measurement but also allows for determining the peak time of the input signal. Additionally, by incorporating an Analog-to-Digital Converter (ADC), the peak value of V_{in} can be captured, offering further information about the event's intensity. Using a differentiator circuit also has an additional advantage: it can reduce static mismatches between the pixels and eventually ease the calibration process.

Figure 4.22 depicts the results of ToT measurements using a DVS pixel, illustrating how ToT correlates with the energy of incident electrons. Two distinct ToT values are observed, similar to those acquired by circuits such as Timepix.

The plot shows two ToT curves: one corresponding to a positive threshold crossing (ToT_{Dpos}) and the other to a negative threshold crossing (ToT_{Dneg}). The positive correlation between ToT and electron energy is consistent with the expectation that higher-energy electrons produce a more significant number of charge carriers in the detector. This results in a stronger signal and a steeper slope in the V_{in} waveform. Consequently, the differentiated signal (V_{deriv}) takes longer to cross the comparator thresholds, leading to a higher ToT value. The observation that both ToT_{Dpos} and ToT_{Dneg} times follow this trend further validates the measurement and confirms the principle of ToT-based energy discrimination.

Interestingly, the ToT_{Dneg} curve is consistently higher than the ToTDpos curve. This behavior suggests that the negative pulse produced by the differentiator circuit lasts longer than the positive pulse. This difference is due to the varying shapes of the positive and negative slopes of the differentiated signal, as seen in Figure 4.22. To address these differences, separate threshold voltages (ΔV_{th_p} and ΔV_{th_n}) were used to detect positive and negative slopes, respectively.

The extended duration of the negative pulse can offer several benefits. It may improve time resolution by providing a longer window for accurate timing measurements. Additionally, it allows for a more relaxed clock period, reducing system speed requirements and potentially lowering power consumption.

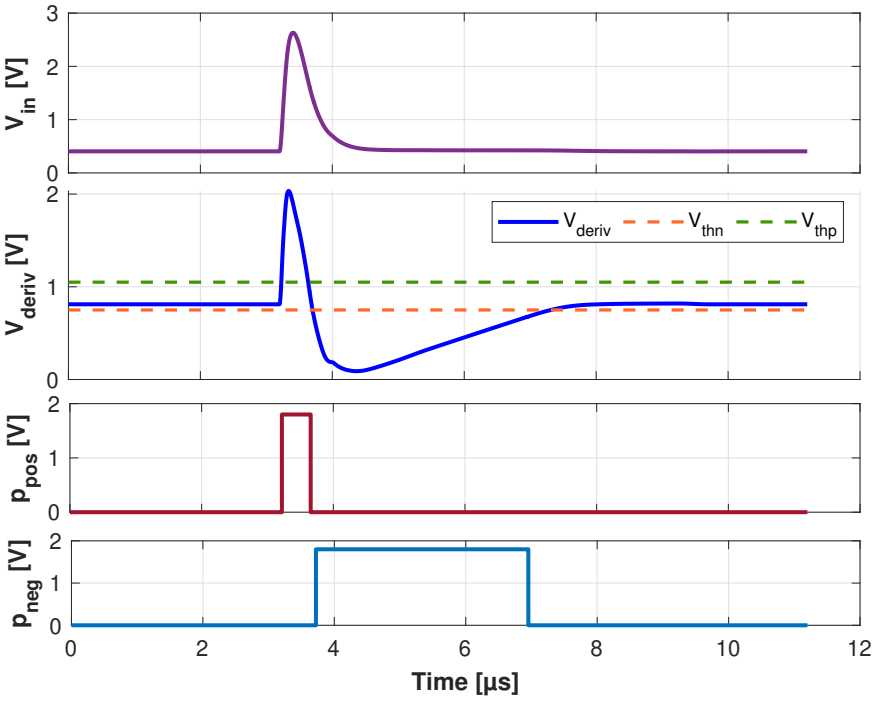

Figure 4.22: Waveforms illustrating the operation of a DVS pixel adapted for ToT measurement using a derivative-based circuit.

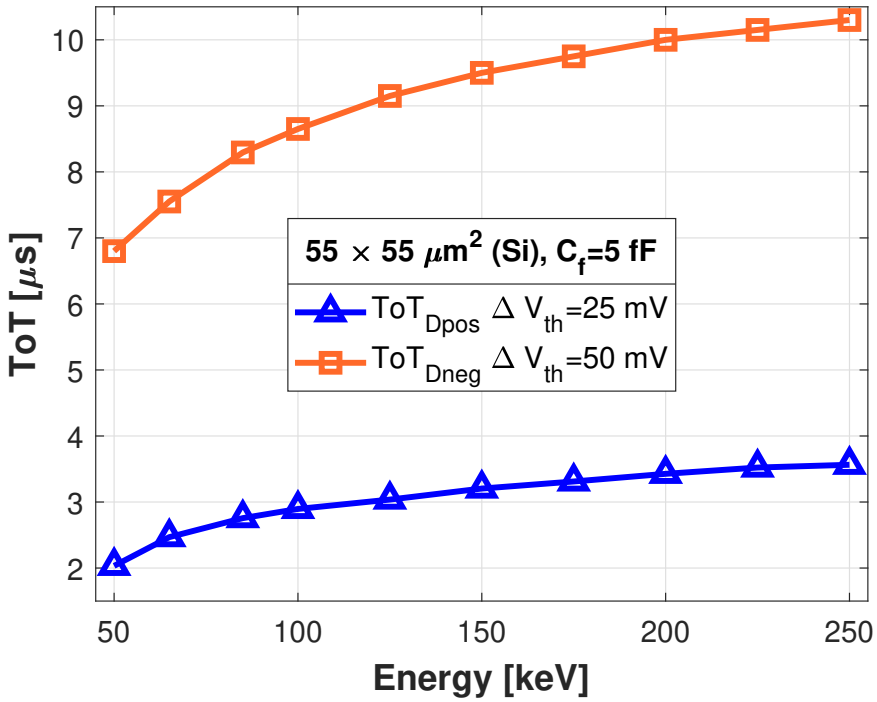

Figure 4.23: Demonstrating energy-dependent ToT behavior in a DVS pixel opens up potential applications in electron microscopy.

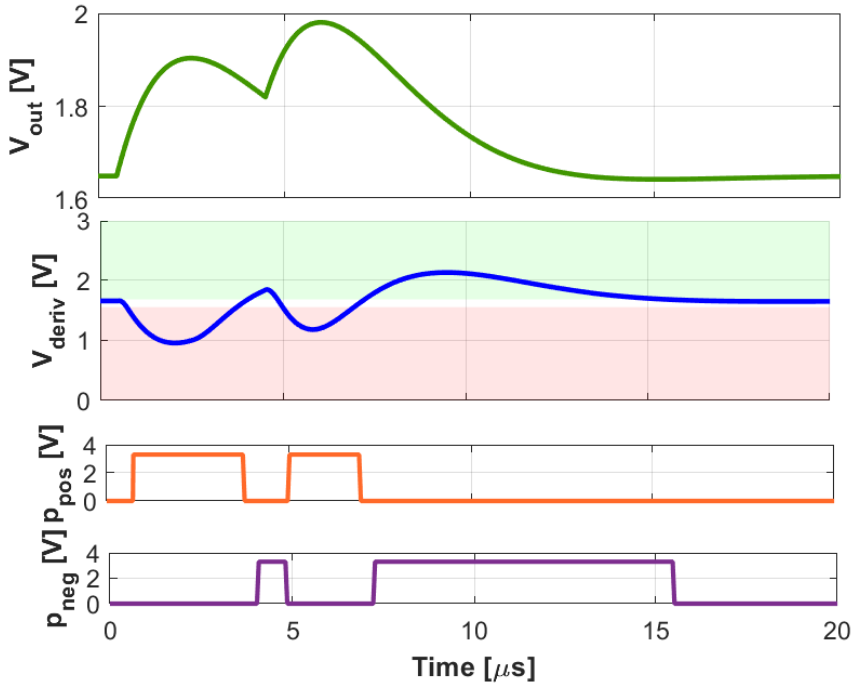

Figure 4.24: Mitigating Coincidence Loss in DVS Pixels: Resolving Closely Spaced Events with Dual-Trigger Functionality.

4.4.2 ToT DVS pixel for coincidence loss mitigation

In traditional Timepix pixels, closely spaced events frequently cause coincidence loss, a typical limitation of conventional detectors. This issue arises because the pixel cannot distinguish between individual events within a brief interval, often shorter than the pixel's recovery time. As a result, the pixel may record these multiple events as a single event with a prolonged ToT duration, which leads to an underestimation (undercounting) of the accurate event count (see Section 2.2.2).

Figure 4.24 shows that the DVS pixel's architecture solves this problem on the microsecond scale. The green and red shaded areas indicate the slope values of the differentiated signal (V_{deriv}) that trigger positive and negative events, respectively. When two events happen close together, the derivative signal may have multiple crossings within the positive and negative threshold region, as seen in the plots p_{pos} and p_{neg}. This feature allows the DVS pixel to detect and register both events, effectively reducing the chances of coincidence loss.

An arbitration protocol ensures that both events are accurately transmitted and processed. This protocol would detect multiple threshold crossings within a short time

frame (limited to a few microseconds by the AER practical implementation [8]) and interpret them as distinct events. By implementing this approach, the DVS pixel can effectively reduce coincidence loss, providing a more accurate count of the actual event rate, even in environments with high event densities. The DVS pixel's ability to distinguish closely spaced events is vital in applications where precise counting is crucial, such as high-energy physics experiments or radiation detection systems. The DVS pixel in Figure 4.21 overcomes the limitations of conventional counting methods, enhancing the performance and reliability of event-driven sensing systems, particularly in demanding settings such as high electron flux environments, radiation-intense conditions, and applications requiring high temporal resolution and low latency.

4.5. Final Remarks

Spectroscopy is essential for advanced electron microscopy applications, particularly in analyzing complex materials at the atomic scale. In this chapter, we introduced two innovative approaches to enhancing the spectral sensitivity of EMPADs by incorporating neuromorphic principles and stacked diode architectures. These designs can be used to implement energy discrimination in sensors for electrons or add spectral sensitivity in EMPADs.

Employing neuromorphic principles in EMPADs diverges from traditional designs and opens the possibility of asynchronous data processing and minimizing data redundancy. Implementing a Time-over-Threshold (ToT) measurement technique achieves efficient, event-driven sensing and minimizes coincidence loss, addressing critical limitations of existing EMPAD technology.

Our stacked diode EMPAD, fabricated using a 0.18 µm CMOS process, successfully captures images with distinct energy components similar to those of a commercial color camera. Experimental results have demonstrated the efficacy of this approach in achieving energy discrimination.

Further research is needed to explore these designs fully. Still, our results show that neuromorphic and stacked diode approaches can significantly enhance electron microscopy and help to obtain a more precise and efficient analysis of materials at the nanoscale.

Chapter 5

Conclusions and Future Work

This chapter summarizes the results obtained in this research, highlighting the successful application of neuromorphic principles in designing novel electron microscopy sensors, including EMPADs. The chapter also outlines future research directions, identifying critical areas for further exploration and advancement.

5.1. Conclusions

The successful fabrication and testing in an SEM of both a neuromorphic pixel prototype and a stacked diode concept, realized using a standard 0.18 μm UMC CMOS process, validate the feasibility and potential impact of these neuromorphic innovations in transforming EM.

The following are the conclusions of the present work:

1. **Comprehensive analysis of the limitations of EMPADs in the state of the art:**

   During this work, we identified and analyzed the bottlenecks impeding the advancement of EMPAD technology, including limitations in spatial and temporal resolution, sensitivity, efficiency, radiation hardness, and cost-effectiveness.

   Factors contributing to these limitations, such as charge sharing and coincidence loss, are treated, along with the inherent trade-offs between sensitivity, efficiency, dynamic range, pixel size, and count. The relationship between dwell times in state-of-the-art detectors and specimen electron dose in modern EM techniques

like 4D-STEM is emphasized. Reducing the beam exposure time of the sample and, consequently, the image acquisition exposure time is crucial for improving EM analysis efficiency (speeding experiments) and enabling the imaging of highly beam-sensitive materials by minimizing the electron dose. However, reducing dwell times will significantly increase data generation rates, which presents a considerable challenge in transferring them to a processing unit or memory. The urgency to address this challenge has made other researchers actively explore innovative solutions in EM.

2. **Investigation of the application of an asynchronous protocol in EM-PADs :**

   In this work, the Address-Event Representation (AER) protocol and neuromorphic design principles offered promising solutions for managing the high data throughput generated in techniques like 4D-STEM. As outlined in Chapter 3, this biologically inspired approach achieved through simulations a data reduction or compression ratios (R_c) of up to 7.5 times at electron fluences of 10^5 e^-/pix/s for detector arrays ranging in size from 128 $\times$ 128 to 1024 $\times$ 1024 pixels, which are typical sizes found in commercial detectors. This strategy significantly reduces data redundancy and enables real-time processing, which is crucial for modern EM challenges. Additionally, it eases the bandwidth and processing demands on the data transmission channel and lowers power consumption and heat dissipation within the pixel, enhancing energy efficiency and thermal stability.

   Moreover, dwell times have an intrinsic relation with a refractory period defined in neuromorphic systems, not only in the amount of data generated but also in their relation to coincidence loss. If this time is shorter than the refractory period, the detector might omit electron impacts during its recovery phase, leading to undercounting. Conversely, a dwell time significantly longer than the refractory period increases the likelihood of multiple electrons hitting the same pixel within that timeframe, potentially causing coincidence loss. **Section 3.3.1 showed how the benefits of data compression of AER protocol are more pronounced at lower refractory periods, indicating its suitability for reducing coincidence loss in EM applications that require reduced dwell times**.

   A neuromorphic pixel compatible with the AER concept, shown in Figure 3.4, was fabricated using a standard CMOS process in 0.18 µm and employing the

UMC foundry[1] from Taiwan. This process is commonly utilized for commercial devices such as cameras, smartphones, automotive sensors, and microcontrollers. The fabricated pixel was tested under SEM beam irradiation, demonstrating four key capabilities:

(a) The ability to capture electron charges and generate outputs based on the rate of change of these charges (current) rather than their absolute values.

(b) Radiation hardening up to 10 keV is achieved through a deposited metal shield. Moreover, this range is very flexible and can be extended easily to much higher energies by thickening the deposited metal layer.

(c) This charge detection method provides a wide dynamic range and linear response, eliminating the need for p-n junctions and ensuring compatibility with different diode detectors. Similarly, it remains highly independent of temperature and process variations.

(d) There is potential to reach an almost 100% fill ratio and to condense the circuitry underneath the detector, maximizing the active sensing area.

Another key achievement of this research was successfully measuring the pixel's total electron emission yield (σ) from the metal electrode (Figure 3.16). By irradiating the pixel with a calibrated electron beam and analyzing the frequency of the resulting output signal, the total electron emission yield was experimentally determined and compared with theoretical models. The close match between the experimental results and the Browning model [114] validated the accuracy of the measurements. It confirmed the effectiveness of the pixel design in detecting and quantifying electron impacts. This accomplishment highlights the potential of the proposed pixel architecture for applications that require precise measurement of electron-matter interactions, such as electron microscopy and radiation detection.

3. **Exploring Stacked Diodes for Energy Discrimination in EMPADs**

We have investigated the design of a pixel array capable of spectral sensitivity. This design is based on a stacked diodes architecture, which has demonstrated promising results in achieving energy discrimination with low-energy electrons in the range of energies used in SEMs [132]. In particular, we have designed and

[1] In the semiconductor industry, a foundry refers to a company that manufactures integrated circuits (ICs) for other companies based on their designs.

fabricated a 44 × 64 pixel matrix of (three) stacked diodes in the 0.18 µm UMC process. This IC can capture images containing three distinct color components like a camera, as illustrated in Figure 4.14. This prototype also confirmed the stacked diode's sensitivity to the electron beam, which remains highly constant for currents between 0.28 nA and 10 nA, as shown in Figure 4.20. However, sensitivity can be further enhanced by reducing the thickness or altering the composition of the passivation layer inherent to the CMOS process.

In addition, a spectra (color) correction algorithm has been developed and implemented to address the undesired spectral overlap between stacked diodes. The algorithm considers the band frequencies of the extracted components and can be extended beyond the typical three-color (R, G, B) model, making it suitable for multichannel spectroscopy. This extension allows for capturing more detailed spectral information, increasing the energy resolution and further improving the versatility of EMPADs in advanced EM techniques. It also holds the potential for enhancing color fidelity in CMOS image sensors.

An EMPAD with an array of stacked diodes would enable the simultaneous acquisition of spatial and spectral data, offering a richer insight into a sample's composition and structure without using complex and bulky spectrometers. It aligns with multimodal STEM concepts (Section 1.1.1) and information-centric data acquisition (Section 2.4) aborded in the present work. It is cheap to implement since it is compatible with STEM in SEM and utilizes a standard CMOS process highly integrated with pixel analog/digital circuitry [132, 136, 164].

4. **Radhard DVS pixel:**

In this research, we have explored and evaluated new strategies to mitigate radiation damage in EMPADs, and in particular, for fabricating novel radhard sensors without relying on hybrid architectures like the ones used in commercial EMPADs such Medipix family (Section 2.2). A notable innovation developed in our research is designing a novel radhard pixel. The pixel structure is based on using a capacitor array instead of a diode as the sensing element and depositing a thick metallic layer on the top plane of the capacitor array using Focused Ion Beam (FIB) technology. This layer can be seen as a radiation-absorbing element, shielding the underlying readout circuitry from direct exposure. Experimental tests lasting approximately two hours at currents up to 10nA using a scanning

electron microscope (SEM) showed radiation hardness at energy levels up to 10 keV.

Moreover, it was also possible to correlate the thickness of the deposited metal layer with the electron's energy and current landing in the pixel, with the appearance of unexpected pulses at the pixel's output without any stimulus (dark current). This unintended response was mainly caused by the electrons trapped in the oxide interface around the MiM capacitors. It highlights the importance of following structural design procedures, as mentioned in Section 3.2.2.

5. **DVS Pixel for Radiation Dosimetry:**

   This work has demonstrated the potential of a novel DVS pixel design with applications extending beyond electron microscopy. The proposed pixel described in Section 3.2.1 can be adapted as a sensor for radiation dosimetry. The reported pixel's sensitivity to accumulated charge in the oxide interface, coupled with the tunable energy threshold provided by the deposited metal layer (Section 3.2.2), opens exciting possibilities for its use as a cost-effective Total Ionizing Dose (TID) dosimeter[2]. This functionality could be precious in applications where real-time dose monitoring is critical, and the sensor's non-destructive nature is not a primary requirement, or what is equal cannot be reused.

6. **DVS Pixel for Electron Energy Measurement in EM**

   This work demonstrates the effectiveness of leveraging temporal dynamics inspired by biological nervous systems to enhance the performance of EMPAD circuits. DVS pixels significantly improve ToT measurements, particularly in high-rate environments such as 4D-STEM, by concentrating on signal changes rather than absolute values. This approach can enhance temporal resolution and, hence, energetic resolution and mitigate coincidence loss for events within a window frame of about 2 µs (Figure 4.24). For instance, it could enable the measurement setup in Figure 4.1 to utilize a single detector instead of two. Moreover, with only some nanoseconds of delay in the arbitration scheme, generating a good time resolution is possible without requiring in-pixel clocking and additional consuming power. This strategy was also applied with certain modifications during

[2]TIDs are devices used to measure the cumulative dose of ionizing radiation absorbed by a material. They are widely used in various fields, including medical physics, radiation protection, and the nuclear industry

a research stay in the USA to perform intelligent data compression of Electrocardiogram (ECG) signals, and that has been published in [165]

5.2. Future Work

Improving the design of the Radhard DVS pixel:

1. The current design, though functional, can be further optimized by strategically positioning the surrounding circuitry shown in Figure 3.9 beneath the pixel's sensing area. This improvement would significantly increase the sensing area, making a radiation-hardened pixel suitable for focal-plane arrays with a high fill ratio. The common-centroid distribution of capacitors in the sensing part offers an additional advantage: minimize offsets between adjacent pixels, thereby reducing FPN. These pixels could also be arranged in a matrix and connected to AER arbitration circuitry so the need for one-shot circuits can be eliminated, further streamlining the design. Future work will focus on integrating these AER-compatible pixels into a matrix architecture for focal plane implementation. Modern AER readout circuitry channels can easily handle pixel event rates of up to 100 Meps, with PDM encoding sufficient for rendering images using this method [127]. This integration would enhance the EMPAD's performance and efficiency and clear the path for its practical implementation in many EM applications.

2. Despite the current implementation of the DVS-compatible pixel in Figure 3.4 utilizes Focused Ion Beam (FIB) deposition for metallization, future iterations can explore alternative techniques such as Chemical Vapor Deposition (CVD), Physical Vapor Deposition (PVD), Top Surface Metallurgy (TSM) [166], or electroplating to achieve industrial-scale production. The methods mentioned above can deposit a protective metal layer directly onto the CMOS die, eliminating the requirement for costly and complex FIB or back-thinning processes.

Improvement of the design of the Stacked Diode EMPAD:

1. Exploring the integration of scintillators with energy-dependent responses alongside the stacked diode EMPAD matrix described in Chapter 4 could provide a promising approach for developing a radhard EMPAD with spectral sensitivity. This strategy combines the strengths of scintillator-based detectors — such as

their durability and broad dynamic range —with the capability for color discrimination offered by the stacked diode architecture.

2. Future refinements of the pixel design should focus on improving the controllability of the reference voltages through on-chip implementation. This task would reduce the overall noise level and enhance signal integrity, improving sensitivity and accuracy in electron detection. Integrating on-chip reference voltage generation would also contribute to a more compact and robust pixel design, ultimately optimizing the overall performance of the EMPAD.

3. The impact of thermal effects on EMPAD performance, particularly the increase in dark current, necessitates further research into advanced thermal management strategies. This problem is so critical that on-chip temperature sensors are used for real-time monitoring and compensation for thermally induced variations in dark current [167]. Investigating efficient cooling solutions, optimizing heat dissipation pathways within the packaging, developing innovative layout structures to minimize thermal gradients, and designing inherently low-power circuits are crucial steps toward the commercialization of this technology.

4. Improving surface transmission (lowering reflectivity) for both light and electrons in the proposed pixel of Figure 4.15, combined with minimizing the thickness of isolation layers, can significantly boost the OE and overall detector sensitivity. Achieving this requires exploring advanced materials and fabrication methods tailored to capture more electrons (and photons) with minimal energy loss while maintaining the structural and functional integrity of the detector.

Improved Matrix Design and Arbitration for EM:

The inherent sparsity of CBED signals in 4D-STEM [18, 65], where most pixels within a diffraction pattern remain dark, aligns well with the event-driven nature of neuromorphic sensors. However, capturing the bright center disk, which contains a very high electron flux, introduces a challenge for arbitration in AER-based systems. The high electron fluence in the central region could monopolize the communication bus, potentially leading to an undercount of events in the sparser areas of the diffraction pattern.

Future research should explore developing alternative arbitration schemes or bus request states that can wisely prioritize events based on their spatial location and in-

tensity. Novel strategies could use adaptive thresholding mechanisms, where the event trigger threshold is dynamically adjusted based on the local electron flux [165]. Alternatively, the arbitration system could also incorporate spatial awareness, giving preference to events originating from less active regions of the detector.

An alternative approach is to explore using multiple AER buses or hierarchical arbitration schemes, where events from different detector regions are handled separately. This strategy would allow for more balanced data transmission and prevent the bright center disk from overwhelming the communication channel. Neuromorphic EMPADs need to address these arbitration challenges to fully harness the benefits of 4D-STEM. Thus, the pixel array can simultaneously capture bright and faint features in the CBED pattern without compromising data integrity or temporal resolution.

The current research, however, focused on validating their effectiveness using sparse signals rather than actual 2D diffraction patterns. Despite this, the AER approach's data reduction capabilities apply to various data types, including those in 4D-STEM.

Appendix A

Annex A: FIB and AFM images

This annex includes microscope images captured during the FIB deposition process to illustrate the technique. Atomic Force Microscopy (AFM), known for its high-resolution surface imaging capabilities, played a crucial role in characterizing the topography and dimensions of the fabricated structures. AFM images are also provided to demonstrate the technique's ability to reveal nanoscale features. This annex offers a concise overview of the principles, instrumentation, and applications of both FIB and AFM, emphasizing their relevance to the research objectives of this dissertation.

A.1. FIB images

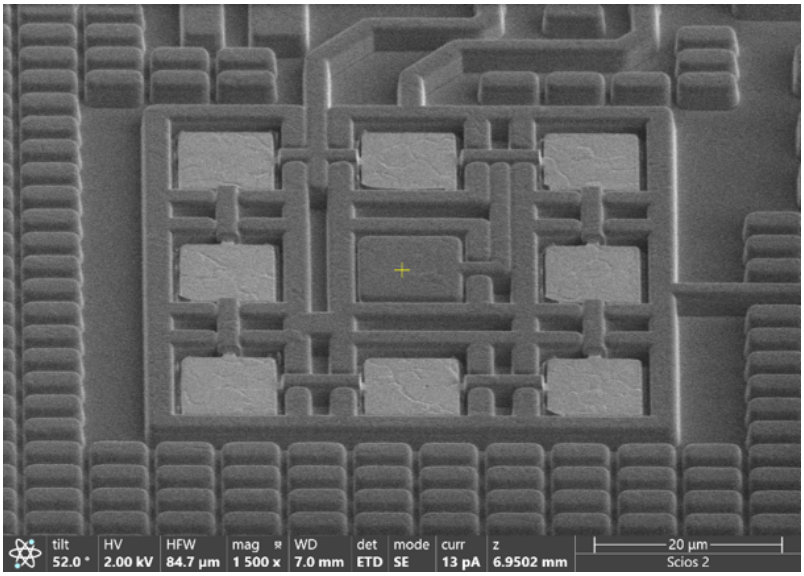

(a)

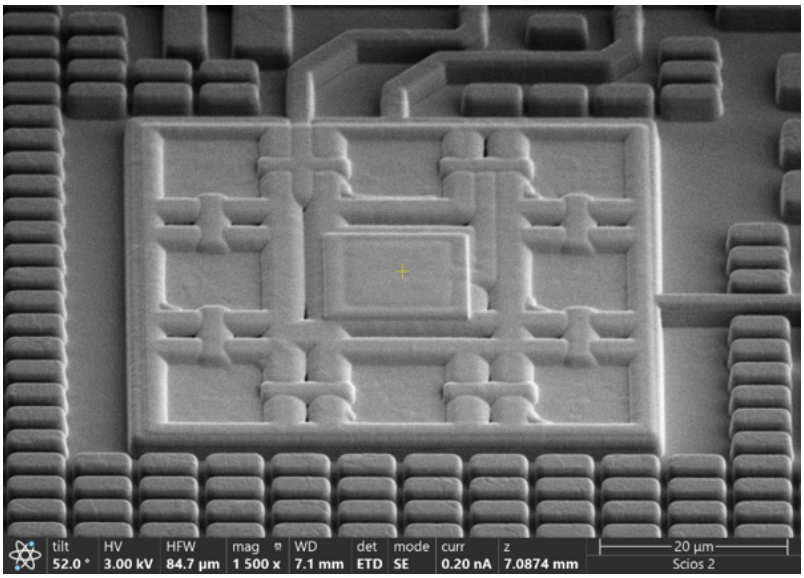

(b)

Figure A.1: Electron microscope images of the pixel with a top metal layer: (a) before and (b) after Platinum deposition using Focused Ion Beam (FIB).

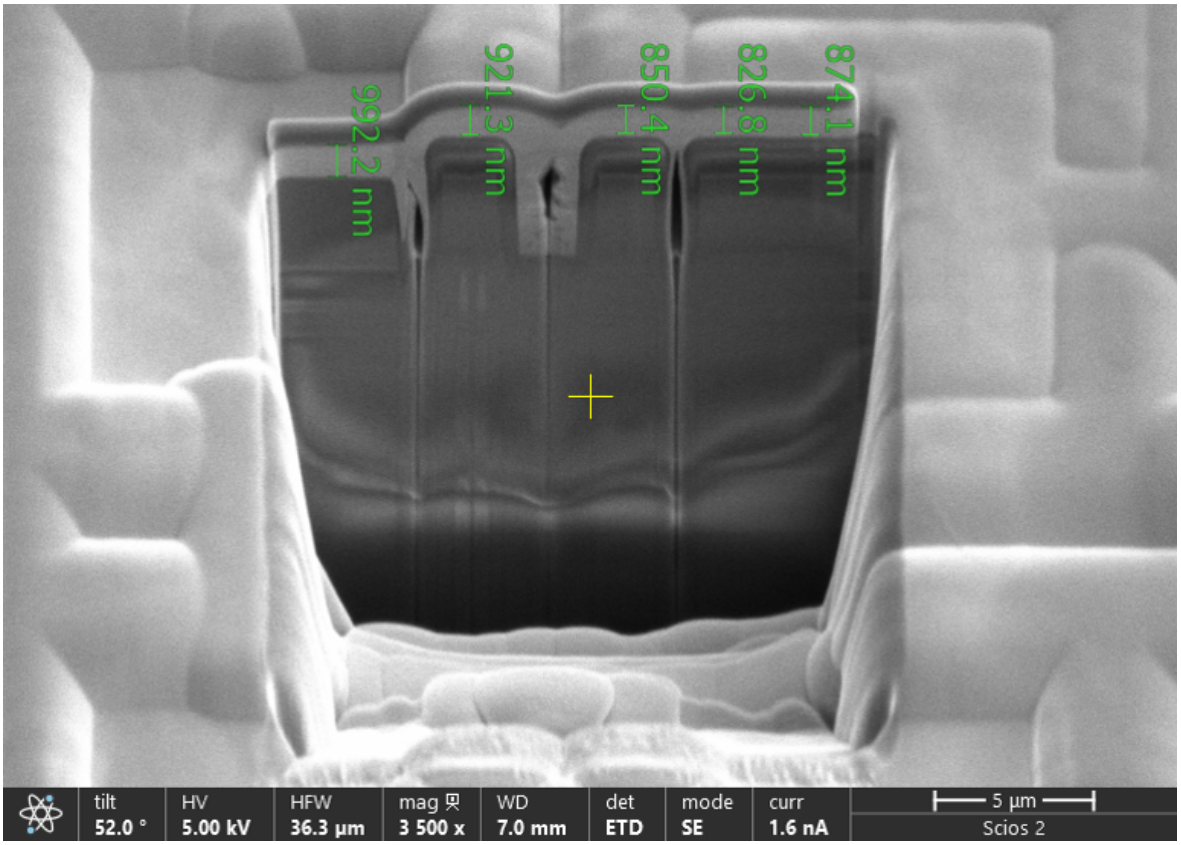

Figure A.2: Cross-sectional electron microscope image of the capacitor array, highlighting the varying thickness of the platinum layer deposited via FIB.

A.2. AFM images

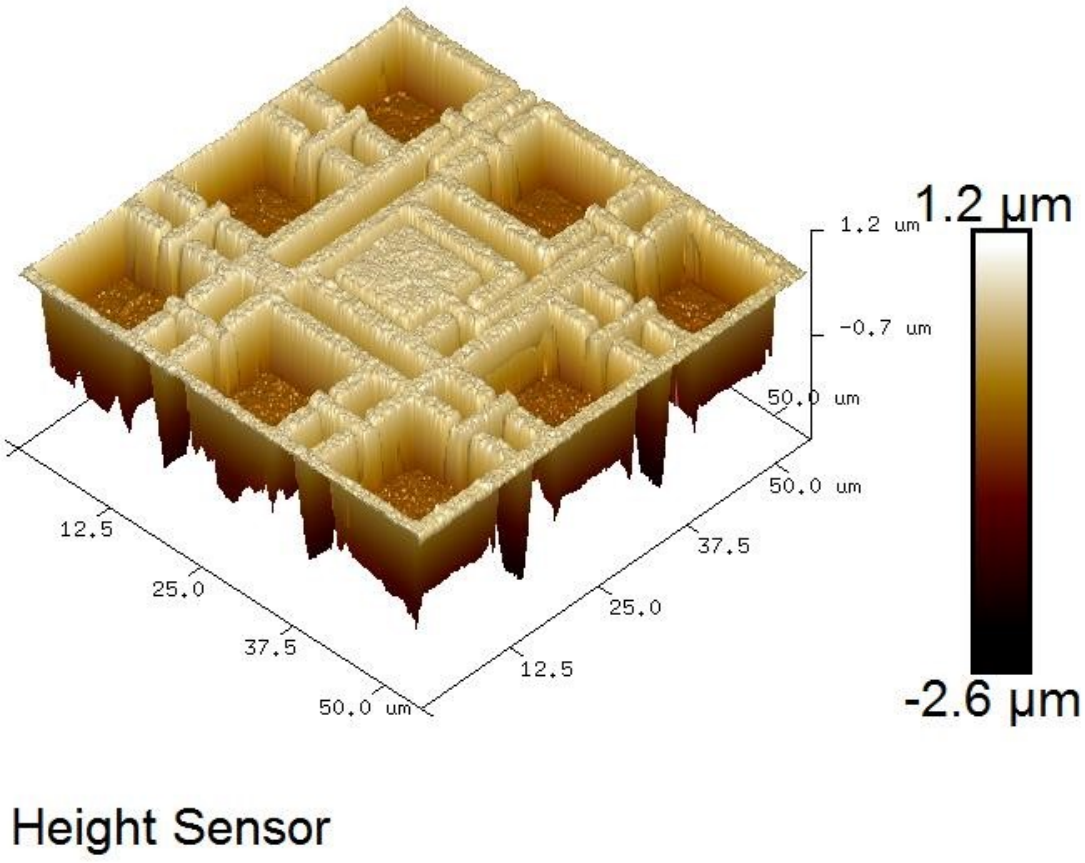

Figure A.3: AFM image of the capacitor array, acquired using a TESPA-V2 probe in tapping mode. Theimagee reveals the surface topography of the silicon dioxide and metal layers, highlighting their distinct heights.

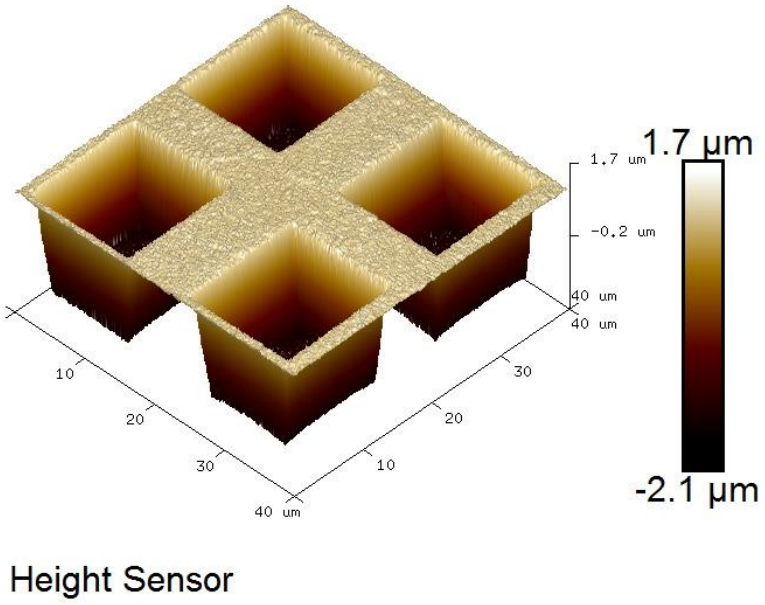

Figure A.4: AFM image (TESPA-V2 probe, tapping mode) of a section of the stacked diode array, showing the silicon dioxide and metal layer topography.

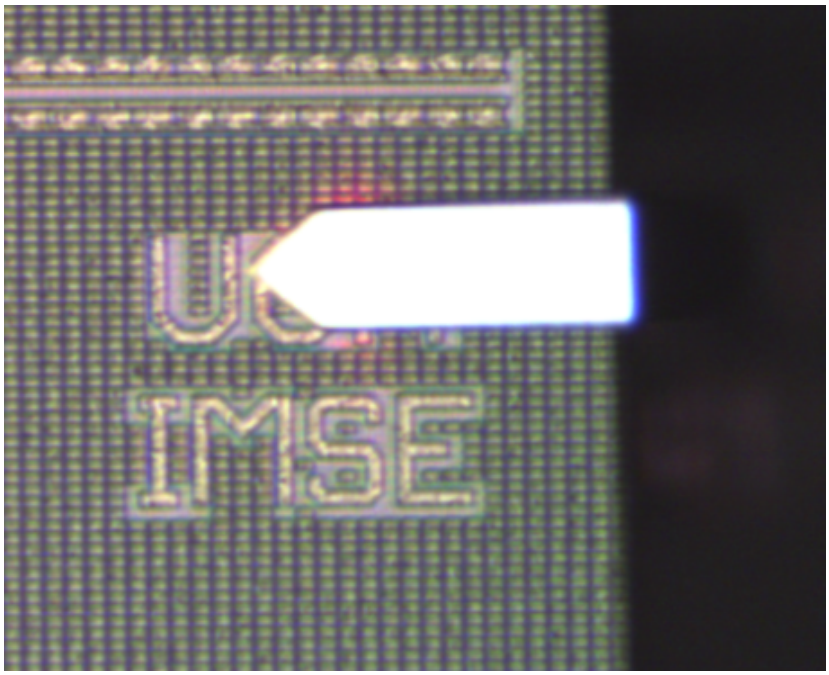

Figure A.5: Image showing the AFM's tip positioned near the analyzed structure

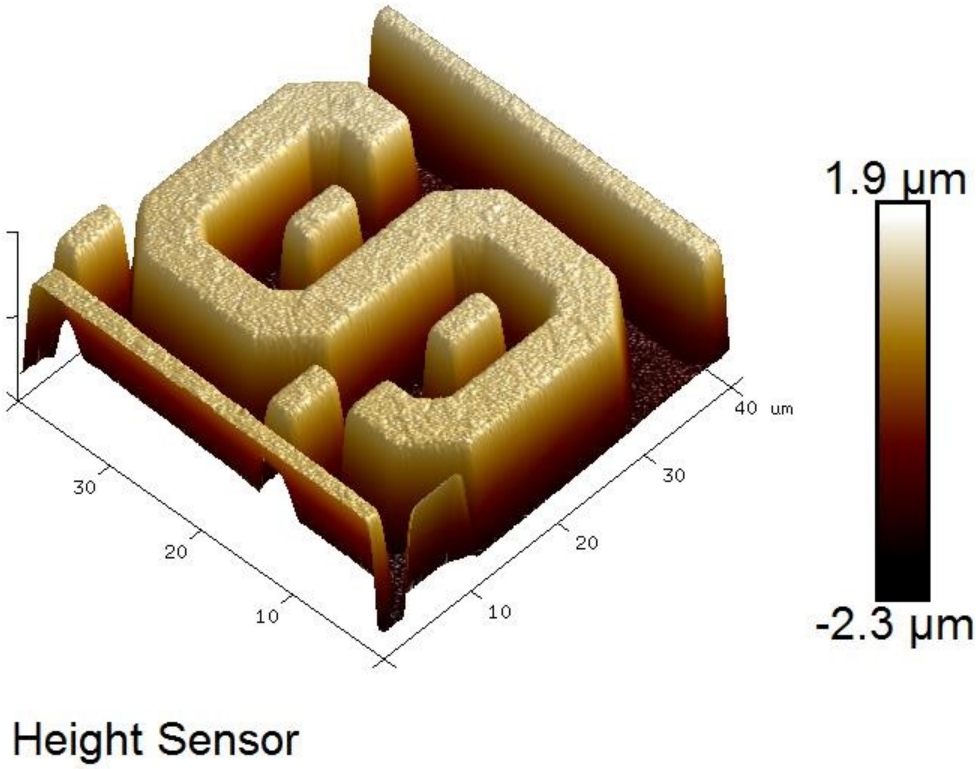

Figure A.6: AFM image reveals the surface topography of the letter "S" from the word "IMSE," which was fabricated using the top metal layer.

A.3. I&F neuron simulation for charge detection

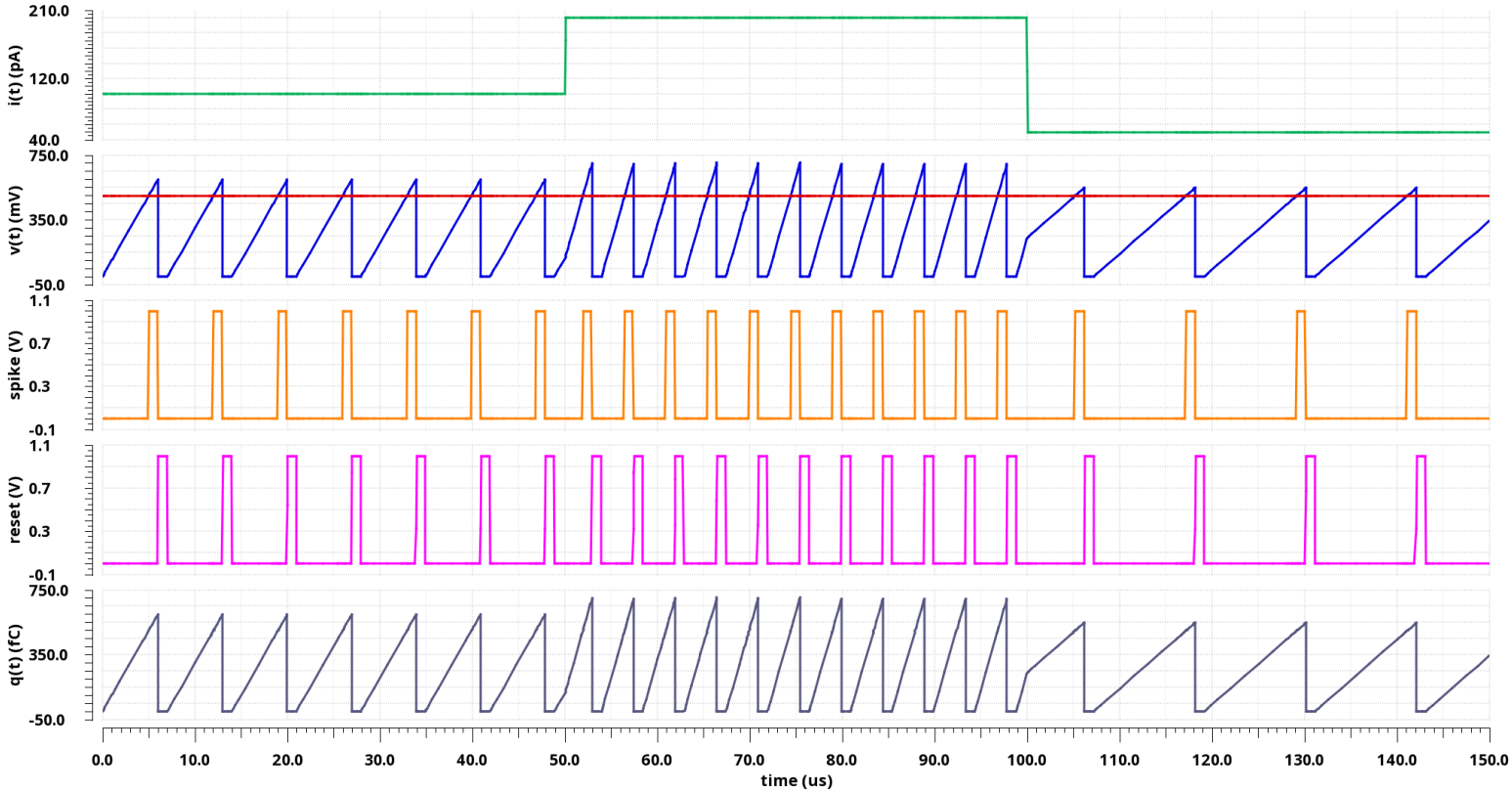

Figure A.7: Simulated spiking activity of the I&F neuron shown in Figure 2.6(a) as a $i(t)$ function and with $C = 1$ fF .

List of Publications

PAPER I:

Saenz-Noval Jorge J., Leñero Bardallo J.A., Gómez Merchán R, Cervera Gontard L. "Procesamiento en el plano focal para un tratamiento de macrodatos más eficiente". *Actas de las Jornadas de Investigación Predoctoral en Ingeniería Informática: Proceedings of the Doctoral Consortium in Computer Science (JIPII 2021)*. Cádiz: Universidad de Cádiz; 2021. pp. 26-30.

PAPER II:

Saenz-Noval, Jorge J., Juan A. Leñero-Bardallo, and Lionel C. Gontard. 2021. "Sensor de imagen con resolución energética para microscopía electrónica." *Actas de las II Jornadas de Investigación Predoctoral en Ingeniería Informática*, 26–30. Cádiz, Spain: Universidad de Cádiz.

PAPER III:

Saenz-Noval Jorge J., Gómez-Merchán R, Leñero-Bardallo J.A., Gontard L.C. "TEMAS: A Flexible Non-AI Algorithm for Metrology of Single-Core and Core-Shell Nanoparticles from TEM Images." *Particle and Particle Systems Characterization*. 2023;40(2).

PAPER IV:

Sáenz-Noval J. J., Leñero-Bardallo J. A., Carmona-Galán R., and Gontard L. C., "A Rad-hard on-chip CMOS charge detector with high dynamic range," *IEEE Sensors Journal*, vol. 23, no. 21, pp. 25971–25979, 2023.

PAPER V:

Sáenz-Noval J. J., Leñero-Bardallo J. A., Gontard L. C., and Tang W., "Dynamic slope detection: A high-compression fidelity-preserving approach for ECG signal acquisition," in *2024 IEEE International Midwest Symposium on Circuits and Systems (MWSCAS)*, IEEE, 2024.

References

[1] L. Chua and L. Yang, "Cellular neural networks: theory," *IEEE Transactions on Circuits and Systems*, vol. 35, no. 10, pp. 1257–1272, 1988.

[2] C. Mead, *Analog VLSI and Neural Systems*. Addison-Wesley VLSI system series, Addison-Wesley, 1989.

[3] M. Mahowald, "VLSI analogs of neuronal visual processing : Thesis by," *Technology*, vol. 1992, 1992.

[4] L. C. Gontard, R. Carmona-Galán, and A. Rodriguez-Vazquez, "Cellular-neural-network focal-plane processor as pre-processor for convnet inference," in *2020 IEEE International Symposium on Circuits and Systems (ISCAS)*, IEEE, Oct. 2020.

[5] M. Silvilotti, *Wiring Considerations in Analog VLSI Systems with Application to Field-programmable Networks*. PhD thesis, Cal. Inst. of Tech., Pasadena, California, 1991.

[6] A. Mortara, E. Vittoz, and P. Venier, "A communication scheme for analog VLSI perceptive systems," *IEEE Journal of Solid-State Circuits*, vol. 30, no. 6, pp. 660–669, 1995.

[7] K. A. Boahen, "Point-to-point connectivity between neuromorphic chips using address events," *IEEE Transactions on Circuits and Systems II*, vol. 47, no. 5, pp. 416–434, 2000.

[8] C. Brandli, R. Berner, M. Yang, S.-C. Liu, and T. Delbruck, "A 240×180 130dB 3µs latency global shutter spatio-temporal vision sensor," *Solid-State Circuits, IEEE Journal of*, vol. 49, pp. 2333–2341, Oct 2014.

[9] P. Lichtsteiner, C. Posch, and T. Delbruck, "A 128 × 128 120dB 15μs latency asynchronous temporal contrast vision sensor," *IEEE Journal of Solid-State Circuits*, vol. 43, pp. 566–576, February 2008.

[10] J. A. Leñero-Bardallo, T. Serrano-Gotarredona, and B. Linares-Barranco, "A 3.6µs latency asynchronous frame-free event-driven dynamic-vision-sensor," *IEEE Journal of Solid-State Circuits*, vol. 46, pp. 1443–1455, June 2011.

[11] K. Jarausch, P. Thomas, D. N. Leonard, R. Twesten, and C. R. Booth, "Four-dimensional STEM-EELS: Enabling nano-scale chemical tomography," *Ultramicroscopy*, vol. 109, no. 4, pp. 326–337, 2009.

[12] H. Yang, L. Jones, H. Ryll, M. Simson, H. Soltau, Y. Kondo, R. Sagawa, H. Banba, I. MacLaren, and P. D. Nellist, "4D STEM: High efficiency phase contrast imaging using a fast pixelated detector," *Journal of Physics: Conference Series*, vol. 644, p. 012032, Oct. 2015.

[13] M. W. Tate, P. Purohit, D. Chamberlain, K. X. Nguyen, R. Hovden, C. S. Chang, P. Deb, E. Turgut, J. T. Heron, D. G. Schlom, D. C. Ralph, G. D. Fuchs, K. S. Shanks, H. T. Philipp, D. A. Muller, and S. M. Gruner, "High dynamic range pixel array detector for scanning transmission electron microscopy," *Microscopy and Microanalysis*, vol. 22, p. 237–249, Jan. 2016.

[14] K. Müller-Caspary, F. F. Krause, T. Grieb, S. Löffler, M. Schowalter, A. Béché, V. Galioit, D. Marquardt, J. Zweck, P. Schattschneider, J. Verbeeck, and A. Rosenauer, "Measurement of atomic electric fields and charge densities from average momentum transfers using scanning transmission electron microscopy," *Ultramicroscopy*, vol. 178, pp. 62–80, 2017. FEMMS 2015.

[15] N. Shibata, T. Seki, G. Sánchez-Santolino, S. D. Findlay, Y. Kohno, T. Matsumoto, R. Ishikawa, and Y. Ikuhara, "Electric field imaging of single atoms," *Nature Communications*, vol. 8, May 2017.

[16] M. Huth, B. Eckert, S. Aschauer, E. Hedley, P. Nellist, P. Majewski, L. Struder, and H. Soltau, "Combine 4D STEM and EELS Using a Fast Pixelated Direct Detector with Center Hole," *Microscopy and Microanalysis*, vol. 29, pp. 401–402, 07 2023.

[17] C. Shi, Z. Cheng, M. R. Jones, and Y. Han, "In-situ and Multi-modal 4D-STEM of Core@Shell Nanoparticles Interdiffusion," *Microscopy and Microanalysis*, vol. 29, pp. 254–255, 07 2023.

[18] B. D. Levin, C. Zhang, B. Bammes, P. M. Voyles, and R. B. Bilhorn, "4D STEM with a direct electron detector," *Microscopy and Analysis*, vol. 34, pp. 20–2, 2020.

[19] J. M. Bekkevold, J. J. P. Peters, R. Ishikawa, N. Shibata, and L. Jones, "Ultra-fast digital DPC yielding high spatio-temporal resolution for low-dose phase characterisation," 2024.

[20] J. Lv, H. Zhang, D. Zhang, L. Liu, and Y. Han, "Low-dose electron microscopy imaging of electron beam-sensitive crystalline materials," *Accounts of Materials Research*, vol. 3, no. 5, pp. 552–564, 2022.

[21] A. R. Faruqi and R. Henderson, "Electronic detectors for electron microscopy," *Current Opinion in Structural Biology*, vol. 17, pp. 549–555, 2007.

[22] X. Sang and J. M. LeBeau, "Characterizing the response of a scintillator-based detector to single electrons," *Ultramicroscopy*, vol. 161, pp. 3–9, 2 2016.

[23] B. D. A. Levin, "Direct detectors and their applications in electron microscopy for materials science," *Journal of Physics: Materials*, vol. 4, p. 042005, July 2021.

[24] A. Faruqi and G. McMullan, "Direct imaging detectors for electron microscopy," *Nuclear Instruments and Methods in Physics Research Section A: Accelerators, Spectrometers, Detectors and Associated Equipment*, vol. 878, p. 180–190, Jan. 2018.

[25] L. C. Gontard, G. Moldovan, R. Carmona-Galán, C. Lin, and A. I. Kirkland, "Detecting single-electron events in TEM using low-cost electronics and a silicon strip sensor," *Microscopy*, vol. 63, pp. 119–130, 01 2014.

[26] A. Faruqi, "Prospects for hybrid pixel detectors in electron microscopy," *Nuclear Instruments and Methods in Physics Research Section A: Accelerators, Spectrometers, Detectors and Associated Equipment*, vol. 466, p. 146–154, June 2001.

[27] A. Faruqi, D. Cattermole, R. Henderson, B. Mikulec, and C. Raeburn, "Evaluation of a hybrid pixel detector for electron microscopy," *Ultramicroscopy*, vol. 94, p. 263–276, Apr. 2003.

[28] J. C. Kim, S. E. Anderson, W. Kaye, F. Zhang, Y. Zhu, S. J. Kaye, and Z. He, "Charge sharing in common-grid pixelated CdZnTe detectors," *Nuclear Instruments and Methods in Physics Research Section A: Accelerators, Spectrometers, Detectors and Associated Equipment*, vol. 654, p. 233–243, Oct. 2011.

[29] S. S. Hsieh, "Coincidence counters for charge sharing compensation in spectroscopic photon counting detectors," *IEEE Transactions on Medical Imaging*, vol. 39, pp. 678–687, 2020.

[30] K. Mathieson, M. Passmore, P. Seller, M. Prydderch, V. O'Shea, R. Bates, K. Smith, and M. Rahman, "Charge sharing in silicon pixel detectors," *Nuclear Instruments and Methods in Physics Research Section A: Accelerators, Spectrometers, Detectors and Associated Equipment*, vol. 487, p. 113–122, July 2002.

[31] X. Li, P. Mooney, S. Zheng, C. R. Booth, M. B. Braunfeld, S. Gubbens, D. A. Agard, and Y. Cheng, "Electron counting and beam-induced motion correction enable near-atomic-resolution single-particle cryo-EM," *Nature Methods*, vol. 10, p. 584–590, May 2013.

[32] X. Xie, L. Barba Flores, B. Bejar Haro, A. Bergamaschi, E. Fröjdh, E. Müller, K. Paton, E. Poghosyan, and C. Remlinger, "Enhancing spatial resolution in mÖnch for electron microscopy via deep learning," *Journal of Instrumentation*, vol. 19, p. C01020, Jan. 2024.

[33] M. Tencé, J.-D. Blazit, X. Li, M. Krajnak, E. N. del Busto, R. Skogeby, L. Cambou, M. Kociak, O. Stephan, and A. Gloter, "Electron energy-loss spectroscopy using merlinEM - Medipix3 detector," *Microscopy and Microanalysis*, vol. 26, p. 1940–1942, July 2020.

[34] B. Plotkin-Swing, G. J. Corbin, S. D. Carlo, N. Dellby, C. Hoermann, M. V. Hoffman, T. C. Lovejoy, C. E. Meyer, A. Mittelberger, R. Pantelic, L. Piazza, and O. L. Krivanek, "Hybrid pixel direct detector for electron energy loss spectroscopy," *Ultramicroscopy*, vol. 217, 10 2020.

[35] W. Wong, J. Alozy, R. Ballabriga, M. Campbell, I. Kremastiotis, X. Llopart, T. Poikela, V. Sriskaran, L. Tlustos, and D. Turecek, "Introducing Timepix2, a frame-based pixel detector readout ASIC measuring energy deposition and arrival time," *Radiation Measurements*, vol. 131, p. 106230, 2020.

[36] X. Li, S. Q. Zheng, K. Egami, D. A. Agard, and Y. Cheng, "Influence of electron dose rate on electron counting images recorded with the K2 camera," *Journal of Structural Biology*, vol. 184, pp. 251–260, 11 2013.

[37] M. S. Barnaby D.A. Levin and B. Bammes, "Event-based direct detectors and their applications in electron microscopy," *Microscopy and Analysis*, vol. 64, p. 15, 2023.

[38] A. I. Ruskin, Z. Yu, and N. Grigorieff, "Quantitative characterization of electron detectors for transmission electron microscopy," *Journal of Structural Biology*, vol. 184, p. 385–393, Dec. 2013.

[39] M. Wu, D. G. Stroppa, P. Pelz, and E. Spiecker, "Using a fast hybrid pixel detector for dose-efficient diffraction imaging beam-sensitive organic molecular thin films," *Journal of Physics: Materials*, vol. 6, p. 045008, Sept. 2023.

[40] A. Belianinov, R. Vasudevan, E. Strelcov, C. Steed, S. M. Yang, A. Tselev, S. Jesse, M. Biegalski, G. Shipman, C. Symons, A. Borisevich, R. Archibald, and S. Kalinin, "Big data and deep data in scanning and electron microscopies: deriving functionality from multidimensional data sets," *Advanced Structural and Chemical Imaging*, vol. 1, May 2015.

[41] S. Jesse, M. Chi, A. Belianinov, C. Beekman, S. V. Kalinin, A. Y. Borisevich, and A. R. Lupini, "Big data analytics for scanning transmission electron microscopy ptychography," *Scientific Reports*, vol. 6, May 2016.

[42] D. Weber, A. Clausen, and R. E. Dunin-Borkowski, *Next-Generation Information Technology Systems for Fast Detectors in Electron Microscopy*, p. 83–120. World Scientific, Mar. 2020.

[43] G. Zanella, "DQE as quantum efficiency of imaging detectors," *arXiv preprint physics/0211112*, 2002.

[44] M. Bath, "Evaluating imaging systems: practical applications," *Radiation Protection Dosimetry*, vol. 139, p. 26–36, Feb. 2010.

[45] P. Zambon, "Enhanced DQE and sub-pixel resolution by single-event processing in counting hybrid pixel electron detectors: A simulation study," *Frontiers in Physics*, vol. 11, Feb. 2023.

[46] G. McMullan, S. Chen, R. Henderson, and A. R. Faruqi, "Detective quantum efficiency of electron area detectors in electron microscopy," *Ultramicroscopy*, vol. 109, pp. 1126–1143, 8 2009.

[47] G. McMullan, R. Turchetta, and A. R. Faruqi, "Single event imaging for electron microscopy using MAPS detectors," *Journal of Instrumentation*, vol. 6, p. C04001, apr 2011.

[48] N. Brodusch, H. Demers, A. Gellé, A. Moores, and R. Gauvin, "Electron energy-loss spectroscopy (EELS) with a cold-field emission scanning electron microscope at low accelerating voltage in transmission mode," *Ultramicroscopy*, vol. 203, p. 21–36, Aug. 2019.

[49] R. Egerton, Y.-Y. Yang, and S. Cheng, "Characterization and use of the gatan 666 parallel-recording electron energy-loss spectrometer," *Ultramicroscopy*, vol. 48, p. 239–250, Mar. 1993.

[50] J. L. Hart, A. C. Lang, A. C. Leff, P. Longo, C. Trevor, R. D. Twesten, and M. L. Taheri, "Direct detection electron energy-loss spectroscopy: A method to push the limits of resolution and sensitivity," *Scientific Reports*, vol. 7, 12 2017.

[51] S. Kujawa and D. Krahl, "Performance of a low-noise CCD camera adapted to a transmission electron microscope," *Ultramicroscopy*, vol. 46, p. 395–403, Oct. 1992.

[52] Y. Auad, M. Walls, J.-D. Blazit, O. Stéphan, L. H. Tizei, M. Kociak, F. De la Peña, and M. Tencé, "Event-based hyperspectral EELS: towards nanosecond temporal resolution," *Ultramicroscopy*, vol. 239, p. 113539, Sept. 2022.

[53] W. R. Dawes, "Overview of radiation hardening for semiconductor detectors," *Nuclear Inst. and Methods in Physics Research, A*, vol. 288, pp. 54–61, 1990.

[54] J. Zhang, E. Fretwurst, R. Klanner, I. Pintilie, J. Schwandt, and M. Turcato, "Investigation of X-ray induced radiation damage at the Si-SiO2interface of silicon sensors for the european XFEL," *Journal of Instrumentation*, vol. 7, p. C12012–C12012, Dec. 2012.

[55] V. Re, L. Gaioni, M. Manghisoni, L. Ratti, E. Riceputi, and G. Traversi, "Ionizing radiation effects on the noise of 65 nm CMOS transistors for pixel sensor readout

at extreme total dose levels," *IEEE Transactions on Nuclear Science*, vol. 65, no. 1, pp. 550–557, 2018.

[56] D. Kobayashi, "Scaling trends of digital single-event effects: A survey of SEU and SET parameters and comparison with transistor performance," *IEEE Transactions on Nuclear Science*, vol. 68, no. 2, pp. 124–148, 2021.

[57] M. Campbell, G. Anelli, M. Burns, E. Cantatore, L. Casagrande, M. Delmastro, R. Dinapoli, F. Faccio, E. Heijne, P. Jarron, M. Luptak, A. Marchioro, P. Martinengo, D. Minervini, M. Morel, E. Pernigotti, I. Ropotar, W. Snoeys, and K. Wyllie, "A pixel readout chip for 10-30 mrad in standard 0.25 /spl mu/m CMOS," in *1998 IEEE Nuclear Science Symposium Conference Record. 1998 IEEE Nuclear Science Symposium and Medical Imaging Conference (Cat. No.98CH36255)*, vol. 2, pp. 827–831 vol.2, 1998.

[58] P. Ercius, I. J. Johnson, P. Pelz, B. H. Savitzky, L. Hughes, H. G. Brown, S. E. Zeltmann, S.-L. Hsu, C. C. S. Pedroso, B. E. Cohen, R. Ramesh, D. Paul, J. M. Joseph, T. Stezelberger, C. Czarnik, M. Lent, E. Fong, J. Ciston, M. C. Scott, C. Ophus, A. M. Minor, Denes, and Peter, "The 4D camera: an 87 kHz direct electron detector for scanning/transmission electron microscopy," 2023.

[59] M. Caselle, T. Blank, F. Colombo, A. Dierlamm, U. Husemann, S. Kudella, and M. Weber, "Low-cost bump-bonding processes for high energy physics pixel detectors," *Journal of Instrumentation*, vol. 11, p. C01050–C01050, Jan. 2016.

[60] D. P. Magalhaes, J. Rinkel, and A. Tomal, "Radiation damage impact on hybrid-pixel detectors data," *Radiation Physics and Chemistry*, vol. 160, pp. 63–67, jul 2019.

[61] B. W. Caplins, J. D. Holm, R. M. White, and R. R. Keller, "Orientation mapping of graphene using 4D STEM-in-SEM," *Ultramicroscopy*, vol. 219, p. 113137, 2020.

[62] S. R. Spurgeon, C. Ophus, L. Jones, A. Petford-Long, S. V. Kalinin, M. J. Olszta, R. E. Dunin-Borkowski, N. Salmon, K. Hattar, W.-C. D. Yang, *et al.*, "Towards data-driven next-generation transmission electron microscopy," *Nature Materials*, vol. 20, no. 3, pp. 274–279, 2021.

[63] S. R. Spurgeon, K. Yano, C. Doty, S. Akers, and M. Olszta, "Revealing the latent atomic world through data-driven microscopy," *Microscopy and Analysis*, vol. 69,

p. S3, 2023.

[64] C. E. Shannon, "A mathematical theory of communication," *Bell System Technical Journal*, vol. 27, no. 3, pp. 379–423, 1948.

[65] H. C. Ni, R. Yuan, J. Zhang, and J. M. Zuo, "Framework of compressive sensing and data compression for 4D-STEM," *Ultramicroscopy*, vol. 259, 5 2024.

[66] A. Faruqi and G. McMullan, "Direct imaging detectors for electron microscopy," *Nuclear Instruments and Methods in Physics Research Section A: Accelerators, Spectrometers, Detectors and Associated Equipment*, vol. 878, pp. 180–190, 2018.

[67] D. Gadkari, K. Shanks, H. Philipp, M. Tate, J. Thom-Levy, and S. Gruner, "Characterization of an architecture for front-end pixel binning in an integrating pixel array detector," *Journal of Instrumentation*, vol. 15, p. T11002–T11002, Nov. 2020.

[68] L. Clark, T. Petersen, T. Williams, M. Morgan, D. Paganin, and S. Findlay, "High contrast at low dose using a single, defocussed transmission electron micrograph," *Micron*, vol. 124, p. 102701, Sept. 2019.

[69] Z. Dong, Y. Zhang, C.-C. Chiu, S. Lu, J. Zhang, Y.-C. Liu, S. Liu, J.-C. Yang, P. Yu, Y. Wang, and Z. Chen, "Sub-nanometer depth resolution and single dopant visualization achieved by tilt-coupled multislice electron ptychography," 2024.

[70] C. Liu, O. Lin, S. Pidaparthy, H. Ni, Z. Lyu, J.-M. Zuo, and Q. Chen, "4D-STEM mapping of nanocrystal reaction dynamics and heterogeneity in a graphene liquid cell," *Nano Letters*, vol. 24, p. 3890–3897, Mar. 2024.

[71] M. Hanwell, "Open source platform for live processing of high data rate electron microscopy (SBIR phase i award topic 15, subtopic b, final scientific/technical report)," tech. rep., Kitware Inc., Clifton Park, NY (United States), 2020.

[72] A. Clausen, D. Weber, K. Ruzaeva, V. Migunov, A. Baburajan, A. Bahuleyan, J. Caron, R. Chandra, S. Halder, M. Nord, K. Müller-Caspary, and R. Dunin-Borkowski, "LiberTEM: Software platform for scalable multidimensional data processing in transmission electron microscopy," *Journal of Open Source Software*, vol. 5, p. 2006, June 2020.

[73] D. Mukherjee, K. M. Roccapriore, A. Al-Najjar, A. Ghosh, J. D. Hinkle, A. R. Lupini, R. K. Vasudevan, S. V. Kalinin, O. S. Ovchinnikova, M. A. Ziatdinov, and

N. S. Rao, "A roadmap for edge computing enabled automated multidimensional transmission electron microscopy," *Microscopy Today*, vol. 30, p. 10–19, Nov. 2022.

[74] K. Kimoto, J. Kikkawa, K. Harano, O. Cretu, Y. Shibazaki, and F. Uesugi, "Unsupervised machine learning combined with 4D scanning transmission electron microscopy for bimodal nanostructural analysis," *Scientific Reports*, vol. 14, Feb. 2024.

[75] H. Guo, E. Franken, Y. Deng, S. Benlekbir, G. Singla Lezcano, B. Janssen, L. Yu, Z. A. Ripstein, Y. Z. Tan, and J. L. Rubinstein, "Electron-event representation data enable efficient cryoEM file storage with full preservation of spatial and temporal resolution," *IUCrJ*, vol. 7, p. 860–869, Aug. 2020.

[76] J. V. Stone, *Information Theory.* A Tutorial Introduction Book, Sheffield, England: Sebtel Press, Apr. 2014.

[77] S. Yamada, T. Ito, K. Gouhara, and Y. Uchikawa, "Electron-count imaging in SEM," *Scanning*, vol. 13, no. 2, pp. 165–171, 1991.

[78] H. Mateos, A. Ferretti, L. Mele, and I. Perić, "Development of CMOS sensors for electron microscopy," *Journal of Instrumentation*, vol. 14, p. C12002–C12002, Dec. 2019.

[79] P. Smeets, R. dos Reis, A. Pakzad, and D. Joester, "Assessing the structure-property relationship in enamel at the nanoscale using 4D-STEM," *Microscopy and Microanalysis*, vol. 26, p. 1484–1486, July 2020.

[80] I. Lazić, M. Wirix, M. L. Leidl, F. de Haas, D. Mann, M. Beckers, E. V. Pechnikova, K. Müller-Caspary, R. Egoavil, E. G. T. Bosch, and C. Sachse, "Single-particle cryo-EM structures from iDPC–STEM at near-atomic resolution," *Nature Methods*, vol. 19, p. 1126–1136, Sept. 2022.

[81] X. Llopart, M. Campbell, D. San Segundo, E. Pernigotti, and R. Dinapoli, "Medipix2, a 64k pixel read out chip with 55 /spl mu/m square elements working in single photon counting mode," in *2001 IEEE Nuclear Science Symposium Conference Record (Cat. No.01CH37310)*, vol. 3, pp. 1484–1488 vol.3, 2001.

[82] X. Llopart, R. Ballabriga, M. Campbell, L. Tlustos, and W. Wong, "Timepix, a 65k programmable pixel readout chip for arrival time, energy and/or pho-

ton counting measurements," *Nuclear Instruments and Methods in Physics Research, Section A: Accelerators, Spectrometers, Detectors and Associated Equipment*, vol. 581, no. 1-2 SPEC. ISS., pp. 485–494, 2007.

[83] R. Ballabriga, J. Alozy, G. Blaj, M. Campbell, M. Fiederle, E. Frojdh, E. Heijne, X. Llopart, M. Pichotka, S. Procz, *et al.*, "The Medipix3RX: a high resolution, zero dead-time pixel detector readout chip allowing spectroscopic imaging," *Journal of Instrumentation*, vol. 8, no. 02, p. C02016, 2013.

[84] D. Jannis, C. Hofer, C. Gao, X. Xie, A. Béché, T. Pennycook, and J. Verbeeck, "Event driven 4D STEM acquisition with a timepix3 detector: Microsecond dwell time and faster scans for high precision and low dose applications," *Ultramicroscopy*, vol. 233, p. 113423, 2022.

[85] S. Seifer, P. Kirchweger, K. M. Edel, and M. Elbaum, "Optimizing contrast in automated 4D STEM cryotomography," *Microscopy and Microanalysis*, 2024.

[86] S. Huang and P. M. Voyles, "5D-STEM of real- and reciprocal-space resolved dynamics in a metallic liquid," *Microscopy and Microanalysis*, vol. 29, p. 272–273, July 2023.

[87] D. Chatterjee, S. Huang, K. Gu, J. Ju, J. Yu, H. Bock, L. Yu, M. D. Ediger, and P. M. Voyles, "Using 4D STEM to probe mesoscale order in molecular glass films prepared by physical vapor deposition," *Nano Letters*, vol. 23, p. 2009–2015, Feb. 2023.

[88] R. Peng, X. Fu, J. H. Mendez, P. S. Randolph, B. E. Bammes, and S. M. Stagg, "Characterizing the resolution and throughput of the apollo direct electron detector," *Journal of Structural Biology: X*, vol. 7, p. 100080, 2023.

[89] P. Häfliger and J. A. Leñero, "Neuromorphic Electronics Lecture Notes," tech. rep., University of Oslo, 2005.

[90] C. D. Schuman, T. E. Potok, R. M. Patton, J. D. Birdwell, M. E. Dean, G. S. Rose, and J. S. Plank, "A survey of neuromorphic computing and neural networks in hardware," 2017.

[91] M. A. Sivilotti, *Wiring considerations in analog VLSI systems, with application to field-programmable networks.* PhD thesis, Computer Science, 1991.

[92] M. Mahowald, *An Analog VLSI System for Stereoscopic Vision.* Kluwer, 1994.

[93] K. Boahen, "A throughput-on-demand address-event transmitter for neuromorphic chips," in *Proceedings 20th Anniversary Conference on Advanced Research in VLSI*, IEEE, 1999.

[94] A. Mortara and E. A. Vittoz, "A communication architecture tailored for analog VLSI artificial neural networks: intrinsic performance and limitations," *IEEE Transactions on Neural Networks*, vol. 5, pp. 459–466, May 1994.

[95] J. T. Marienborg and T. S. Lande, "Analog state transmission with digital hardware," in *NORCHIP 1998*, p. 249–256, 1998.

[96] A. M. T. Linn, D. A. Tuan, C. Shoushun, and Y. K. Seng, "Adaptive priority toggle asynchronous tree arbiter for AER-based image sensor," in *2011 IEEE/IFIP 19th International Conference on VLSI and System-on-Chip*, pp. 66–71, Oct 2011.

[97] P. N. McMahon-Crabtree, L. Kulesza, B. J. McReynolds, D. S. O'Keefe, A. Puttur, D. Maestas, C. P. Morath, and M. G. McHarg, "Event-based camera refractory period characterization and initial clock drift evaluation," in *Unconventional Imaging, Sensing, and Adaptive Optics 2023* (S. R. Bose-Pillai, J. J. Dolne, and M. F. Spencer, eds.), SPIE, Oct. 2023.

[98] I. MacLaren, T. MacGregor, C. Allen, and A. Kirkland, "Detectors-the ongoing revolution in scanning transmission electron microscopy and why this important to material characterization, apl mater. 8 (2020) 110901."

[99] M. Fiederle, S. Procz, E. Hamann, A. Fauler, and C. Fröjdh, "Overview of GaAs und CdTe pixel detectors using medipix electronics," *Crystal Research and Technology*, vol. 55, Aug. 2020.

[100] N. Wermes, "Pixel detectors for particle physics and imaging applications," *Nuclear Instruments and Methods in Physics Research Section A: Accelerators, Spectrometers, Detectors and Associated Equipment*, vol. 512, p. 277–288, Oct. 2003.

[101] R. Ballabriga, M. Campbell, and X. Llopart, "ASIC developments for radiation imaging applications: The medipix and timepix family," *Nuclear Instruments and Methods in Physics Research Section A: Accelerators, Spectrometers, Detectors and Associated Equipment*, vol. 878, pp. 10–23, 2018. Radiation Imaging Techniques and Applications.

[102] J. A. Leñero-Bardallo, R. Carmona-Galán, and A. Rodríguez-Vázquez., "A bio-inspired vision sensor with dual operation and readout modes," *Sensors Journal, IEEE*, vol. 16, pp. 317–330, January 2016.

[103] F. Krummenacher, "Pixel detectors with local intelligence: an IC designer point of view," *Nuclear Instruments and Methods in Physics Research Section A: Accelerators, Spectrometers, Detectors and Associated Equipment*, vol. 305, no. 3, pp. 527–532, 1991.

[104] R. Gomez-Merchan, R. de la Rosa-Vidal, J. A. Leñero-Bardallo, and A. Rodríguez-Vázquez, "Load reduction and adaptive pull-up strategies for time delay reduction in high-resolution AER sensors," in *2023 IEEE International Symposium on Circuits and Systems (ISCAS)*, pp. 1–5, 2023.

[105] J. J. Sáenz-Noval, J. A. Leñero-Bardallo, R. Carmona-Galán, and L. C. Gontard, "A rad-hard on-chip CMOS charge detector with high dynamic range," *IEEE Sensors Journal*, vol. 23, no. 21, pp. 25971–25979, 2023.

[106] P. Lichtsteiner, C. Posch, and T. Delbruck, "A 128 x 128 120dB 30mW asynchronous vision sensor that responds to relative intensity change," in *2006 IEEE International Solid State Circuits Conference - Digest of Technical Papers*, pp. 2060–2069, 2006.

[107] Y. Suh, S. Choi, M. Ito, J. Kim, Y. Lee, J. Seo, H. Jung, D.-H. Yeo, S. Namgung, J. Bong, S. Yoo, S.-H. Shin, D. Kwon, P. Kang, S. Kim, H. Na, K. Hwang, C. Shin, J.-S. Kim, P. K. J. Park, J. Kim, H. Ryu, and Y. Park, "A 1280×960 dynamic vision sensor with a 4.95-μm pixel pitch and motion artifact minimization," in *2020 IEEE International Symposium on Circuits and Systems (ISCAS)*, pp. 1–5, 2020.

[108] V. Sriskaran, J. Alozy, R. Ballabriga, M. Campbell, N. Egidos, J. Fernandez-Tenllado, E. Heijne, I. Kremastiotis, A. Koukab, X. Llopart, J. Sallese, and L. Tlustos, "New architecture for the analog front-end of Medipix4," *Nuclear Instruments and Methods in Physics Research Section A: Accelerators, Spectrometers, Detectors and Associated Equipment*, vol. 978, p. 164412, Oct. 2020.

[109] R. Ballabriga, M. Campbell, E. Heijne, X. Llopart, and L. Tlustos, "The Medipix3 prototype, a pixel readout chip working in single photon counting mode with

improved spectrometric performance," *Nuclear Science, IEEE Transactions on*, vol. 54, pp. 1824 – 1829, 11 2007.

[110] S. Bugby, K. Koch-Mehrin, M. Veale, M. Wilson, and J. Lees, "Energy-loss correction in charge sharing events for improved performance of pixellated compound semiconductors," *Nuclear Instruments and Methods in Physics Research Section A: Accelerators, Spectrometers, Detectors and Associated Equipment*, vol. 940, p. 142–151, Oct. 2019.

[111] M. Veale, S. Bell, D. Duarte, A. Schneider, P. Seller, M. Wilson, and K. Iniewski, "Measurements of charge sharing in small pixel CdTe detectors," *Nuclear Instruments and Methods in Physics Research Section A: Accelerators, Spectrometers, Detectors and Associated Equipment*, vol. 767, p. 218–226, Dec. 2014.

[112] J. A. Lenero-Bardallo, P. Hafliger, R. Carmona-Galan, and A. Rodriguez-Vazquez, "A bio-inspired vision sensor with dual operation and readout modes," *IEEE Sensors Journal*, vol. 16, p. 317–330, Jan. 2016.

[113] V. Sriskaran, J. Alozy, R. Ballabriga, M. Campbell, P. Christodoulou, E. Heijne, A. Koukab, T. Kugathasan, X. Llopart, M. Piller, A. Pulli, J.-M. Sallese, and L. Tlustos, "High-rate, high-resolution single photon X-ray imaging: Medipix4, a large 4-side buttable pixel readout chip with high granularity and spectroscopic capabilities," 2023.

[114] R. Browning, T. Z. Li, B. Chui, J. Ye, R. F. Pease, Z. Czyzewski, and D. C. Joy, "Empirical forms for the electron/atom elastic scattering cross sections from 0.1 to 30 keV," *Journal of Applied Physics*, vol. 76, no. 4, pp. 2016–2022, 1994.

[115] Y. Song, J. Rozsa, J. B. de Magalhaes, S. Smith, B. Karlinsey, W. Kinnison, E. Gustafson, D. E. Austin, A. R. Hawkins, and S.-H. W. Chiang, "A solid-state charge detector with gain calibration using photocurrent," *IEEE Transactions on Instrumentation and Measurement*, vol. 69, no. 12, pp. 9398–9407, 2020.

[116] P. Häfliger, *A spike based learning rule and its implementation in analog hardware*. PhD thesis, ETH Zürich, Switzerland, 2000. http://www.ifi.uio.no/~hafliger.

[117] D. X. D. Yang and A. E. Gamal, "Comparative analysis of SNR for image sensors with enhanced dynamic range," in *Electronic imaging*, 1999.

[118] K. Roy, S. Mukhopadhyay, and S. Member, "Leakage Current Mechanisms and Leakage Reduction Techniques in Deep-Submicrometer CMOS Circuits," *Proceedings of the IEEE*, vol. 91, no. 2, pp. 305–327, 2003.

[119] C.-W. Lu, "High-speed driving scheme and compact high-speed low-power rail-to-rail class-B buffer amplifier for LCD applications," *IEEE Journal of Solid-State Circuits*, vol. 39, no. 11, pp. 1938–1947, 2004.

[120] L. Reimer, *Scanning electron microscopy: Physics of image formation and microanalysis*. Springer, 2010.

[121] D. Drouin, A. Real Couture, R. Gauvin, P. Hovington, P. Homy, and H. Demers, "Casino a free software package for Monte Carlo simulation of electron trajectories in solids."

[122] Y. W. Lan, W. H. Chang, Y. C. Chang, C. S. Chang, and C. D. Chen, "Effect of focused ion beam deposition induced contamination on the transport properties of nano devices," *Nanotechnology*, vol. 26, no. 5, p. 55705, 2015.

[123] R. Gauvin and D. Drouin, "A formula to compute total elastic Mott cross-sections," *Scanning*, vol. 15, no. 3, pp. 140–150, 1993.

[124] Texas Instrument, *12-bit, micropower, quad-channel, digital-to-analog converter (DAC) with rail-to-rail output*, 2006. Rev. 2016.

[125] N. Sakamoto, S. Aoyama, S. Kawahito, and H. Yurimoto, "Development of highly sensitive ion imager corresponding to real-time readout having single-ion detectability," *Japanese Journal of Applied Physics*, vol. 51, p. 076701, jun 2012.

[126] Y. Song, S. Smith, B. Karlinsey, A. R. Hawkins, and S.-H. W. Chiang, "The digital-assisted charge amplifier: A digital-based approach to charge amplification," *IEEE Transactions on Circuits and Systems I: Regular Papers*, vol. 69, no. 8, pp. 3114–3123, 2022.

[127] J. A. Leñero-Bardallo, R. Carmona-Galán, and A. Rodríguez-Vázquez, "Applications of event-based image sensors –Review and analysis," *International Journal of Circuit Theory and Applications*, vol. 46, 08 2018.

[128] J. Fritz, E. B. Cooper, S. Gaudet, P. K. Sorger, and S. R. Manalis, "Electronic detection of dna by its intrinsic molecular charge," *Nat. Acad. Sci. USA*, vol. 99, p. 14142–14146, october 2002.

[129] J. Musayev, Y. Adlgüzel, H. Külah, S. Eminoglu, and A. Tayfun, "Label-free DNA detection using a charge sensitive CMOS microarray sensor chip," *IEEE Sensors Journal*, vol. 14, no. 5, pp. 1608–1616, 2014.

[130] O. Skorka and D. Joseph, "Design and fabrication of vertically-integrated CMOS image sensors," *Sensors*, vol. 11, no. 5, pp. 4512–4538, 2011.

[131] R. B. Merrill, "Color separation in an active pixel cell imaging array using triple-well structure," Oct. 3 1999. US Patent 5,965,207.

[132] L. C. Gontard, J. A. Leńero-Bardallo, F. M. Varela-Feria, and R. Carmona-Galán, "Vertically stacked CMOS-compatible photodiodes for scanning electron microscopy," in *2020 IEEE International Symposium on Circuits and Systems (ISCAS)*, vol. 9, p. 1–5, IEEE, Oct. 2020.

[133] J. L. S.Amelinckx, D.van Dyck and G. Tendeloo, *Electron Microscopy: Principles and Fundamentals*. Wiley, June 1997.

[134] R. Sagawa, H. Hashiguchi, A. Nakamura, S. Shibagaki, Y. Kazama, M. Muth, Y. E. Imari, V. Kroner, and S. Aschauer, "Simultaneous Acquisition of 4D and EELS Data by Newly Developed Pixelated STEM Detector," *Microscopy and Microanalysis*, vol. 30, p. ozae044.948, 07 2024.

[135] G. McMullan, D. Cattermole, S. Chen, R. Henderson, X. Llopart, C. Summerfield, L. Tlustos, and A. Faruqi, "Electron imaging with medipix2 hybrid pixel detector," *Ultramicroscopy*, vol. 107, p. 401–413, Apr. 2007.

[136] J. A. Leñero-Bardallo, M. Delgado-Restituto, R. Carmona-Galán, and Á. Rodríguez-Vázquez, "Enhanced sensitivity of CMOS image sensors by stacked diodes," *IEEE Sensors Journal*, vol. 16, pp. 8448–8455, Dec 2016.

[137] K. Kanaya and S. Okayama, "Penetration and energy-loss theory of electrons in solid targets," *Journal of Physics D: Applied Physics*, vol. 5, p. 43–58, Jan. 1972.

[138] K. Kanaya and S. Okayama, "Penetration and energy-loss theory of electrons in solid targets," *Journal of Physics D: Applied Physics*, vol. 5, no. 1, p. 43, 1972.

[139] P. J. Potts, *A handbook of silicate rock analysis*. Springer Science & Business Media, 2012.

[140] Sharma *et al.*, "Estimating relationship between the time over threshold and energy loss by photons in plastic scintillators used in the J-PET scanner," 2019.

[141] T. Fujiwara, H. Takahashi, K. Shimazoe, and B. Shi, "Multi-level time-over-threshold method for energy resolving multi-channel systems," *IEEE Transactions on Nuclear Science*, vol. 57, p. 2545–2548, Oct. 2010.

[142] J. Jakubek, "Precise energy calibration of pixel detector working in time-over-threshold mode," *Nuclear Instruments and Methods in Physics Research Section A: Accelerators, Spectrometers, Detectors and Associated Equipment*, vol. 633, p. S262–S266, May 2011.

[143] M. Benoit and L. A. Hamel, "Simulation of charge collection processes in semiconductor CdZnTe γ-ray detectors," *Nuclear Instruments and Methods in Physics Research, Section A: Accelerators, Spectrometers, Detectors and Associated Equipment*, vol. 606, no. 3, pp. 508–516, 2009.

[144] H. Spieler, *Semiconductor detector systems*, vol. 12. Oxford university press, 2005.

[145] K. Shimazoe, H. Takahashi, B. Shi, T. Orita, T. Furumiya, J. Ooi, and Y. Kumazawa, "Dynamic time over threshold method," *IEEE Transactions on Nuclear Science*, vol. 59, pp. 3213–3217, 2012.

[146] D. Turecek, J. Jakubek, M. Kroupa, and P. Soukup, "Energy calibration of pixel detector working in time-over-threshold mode using test pulses," *IEEE Nuclear Science Symposium Conference Record*, pp. 1722–1725, 2011.

[147] E. R. Kandel, J. H. Schwartz, T. M. Jessell, S. A. Siegelbaum, and A. J. Hudspeth, *Principles of Neural Science*. McGraw-Hill, 5th ed., 2012.

[148] P. E.-m. H. Edlow, "Multi-Sspectrum Photodiode Devices," 1980.

[149] Sigma Corporation, "Company overview," 2024. Available: https://www.sigma-global.com/.

[150] F. Maloberti, *Data Converters*. Springer, 2007.

[151] M. Pelgrom, *Analog-to-Digital Conversion*. Springer, 2010.

[152] O. T.-C. Chen, K.-H. Lin, and Z. M. Liu, "High-efficiency 3D CMOS image sensor," in *2013 18th OptoElectronics and Communications Conference held*

jointly with 2013 International Conference on Photonics in Switching (OEC-C/PS), pp. 1–2, 2013.

[153] J. Park, S. Diestel, S. Richman, F. Chen, J. Mooney, D. Escobar, D. Sato, C. Lee, and Y. Media, "Hot spot measurement on CMOS-based image sensor using liquid crystal thermograph," in *52nd Electronic Components and Technology Conference 2002. (Cat. No.02CH37345)*, pp. 1627–1630, 2002.

[154] D.-L. Lin, C.-C. Wang, and C.-L. Wei, "Quantified temperature effect in a CMOS image sensor," *IEEE Transactions on Electron Devices*, vol. 57, p. 422–428, Feb. 2010.

[155] M. A. Green, "Self-consistent optical parameters of intrinsic silicon at 300K including temperature coefficients," *Solar Energy Materials and Solar Cells*, vol. 92, no. 11, pp. 1305–1310, 2008.

[156] M. A. Green and M. J. Keevers, "Optical properties of intrinsic silicon at 300 K," *Progress in Photovoltaics: Research and Applications*, vol. 3, p. 189–192, Jan. 1995.

[157] A. Moini, *Vision Chips*. Springer US, 2000.

[158] J. A. Leñero-Bardallo, D. Bryn, and P. Häfliger, "Bio-inspired asynchronous pixel event tricolor vision sensor," *Biomedical Circuits and Systems, IEEE Transactions on*, vol. 8, pp. 345–357, June 2014.

[159] C.-C. Wang, *A study of CMOS technologies for image sensor applications*. PhD thesis, Massachusetts Institute of Technology, 2001.

[160] A. El Gamal and H. Eltoukhy, "CMOS image sensors," *IEEE Circuits and Devices Magazine*, vol. 21, no. 3, pp. 6–20, 2005.

[161] M. Furumiya, H. Ohkubo, Y. Muramatsu, S. Kurosawa, F. Okamoto, Y. Fujimoto, and Y. Nakashiba, "High-sensitivity and no-crosstalk pixel technology for embedded CMOS image sensor," *IEEE Transactions on Electron Devices*, vol. 48, no. 10, pp. 2221–2227, 2001.

[162] Y.-H. Kuo, C.-J. Wu, F.-T. Kuo, J.-Y. Yen, and Y.-Y. Chen, "Image based in situ electron-beam drift detection by silicon photodiodes in scanning-electron microscopy and an electron-beam lithography system," *Microelectronic Engineering*, vol. 103, pp. 137–143, 2013.

[163] A.-C. Milazzo, P. Leblanc, F. Duttweiler, L. Jin, J. C. Bouwer, S. Peltier, M. Ellisman, F. Bieser, H. S. Matis, H. Wieman, P. Denes, S. Kleinfelder, and N.-H. Xuong, "Active pixel sensor array as a detector for electron microscopy," *Ultramicroscopy*, vol. 104, p. 152–159, Sept. 2005.

[164] J. A. Leñero-Bardallo, D. H. Bryn, and P. Häfliger, "Bio-inspired asynchronous pixel event tri-color vision sensor," in *BioCAS*, 2011.

[165] J. J. Sáenz-Noval, J. A. Leñero-Bardallo, L. C. Gontard, and W. Tang, "Dynamic slope detection: A high-compression fidelity-preserving approach for ECG signal acquisition," in *2024 IEEE International Midwest Symposium on Circuits and Systems (MWSCAS)*, IEEE, 2024.

[166] O. Skorka and D. Joseph, "Design and fabrication of vertically-integrated CMOS image sensors," *Sensors*, vol. 11, p. 4512–4538, Apr. 2011.

[167] S. Xie and A. J. P. Theuwissen, "On-chip smart temperature sensors for dark current compensation in CMOS image sensors," *IEEE Sensors Journal*, vol. 19, p. 7849–7860, Sept. 2019.